# Cell Culture Monitoring with Novel Bright Field Miniature Microscopy Prototypes

# Überwachung von Zellkulturen mit neuartigen Hellfeldmikroskopieprototypen

Der Technischen Fakultät
der Friedrich-Alexander-Universität
Erlangen-Nürnberg

zur

Erlangung des Doktorgrades Dr.-Ing.

vorgelegt von

Simon Josef Schöll aus
Freystadt

Als Dissertation genehmigt
von der Technischen Fakultät
der Friedrich-Alexander-Universität Erlangen-Nürnberg

| | |
|---|---|
| Tag der mündlichen Prüfung: | 28.11.2016 |
| Vorsitzender des Promotionsorgans: | Prof. Dr.-Ing. Reinhard Lerch |
| Gutachter: | Prof. Dr.-Ing. Joachim Hornegger |
| | Prof. Dr.-Ing. Dietrich Paulus |

**Abstract**

Cell cultures are monitored to develop new drugs, to find efficient ways to produce vaccines and to perform toxicity tests. The cells are cultivated in an incubator and the monitoring steps such as the acquisition of images and the counting of cells are often done outside. As part of a research project, novel bright field miniature microscopy prototypes were developed. These prototypes were designed to work inside the incubator, and hence, they need to be very small.

In this thesis, image processing methods for these systems (at different development stages) are presented. These methods made the systems usable for cell monitoring in an incubator. This is a main contribution of the thesis. Our analyses of the system and its components helped to improve the development of the systems. A calibration procedure and algorithms for adjusting the illumination and the focus position of these systems are introduced. Moreover, the proposed preprocessing steps such as illumination correction and contrast enhancement improved the image quality.

An image processing library and a cell monitoring software using the library were developed. An algorithm for counting cells in images of the prototype system was included in the image processing library. Features for viability determination were investigated and also included in the library.

Another main contribution is related to all bright field microscopes. They have the following effect in common: Focusing of very thin (phase) objects differs from focusing of objects that are thicker and less transparent for light. This effect is investigated in detail, explained, and the calculation of different useful focus positions for phase objects is derived. The optical focus position can be used for applications such as phase retrieval. Slightly defocused cell images with a maximum in contrast at small details can be useful for applications such as cell segmentation or cell analysis. Strongly defocused cell images with a maximum in contrast for the cell borders can be used for applications such as cell detection.

**Zusammenfassung**

Zellkulturen werden überwacht, um neue Medikamente zu entwickeln, um effiziente Herstellungswege für Impfstoffe zu finden und um Toxizitätsprüfungen durchzuführen. Die Zellen werden in einem Brutschrank kultiviert und Überwachungsschritte wie die Erzeugung von Bildern und das Auszählen der Zellen werden meist außerhalb durchgeführt. Im Rahmen eines Forschungsprojektes wurden neuartige Hellfeldmikroskope entwickelt. Diese Systeme wurden so entwickelt, dass sie im Brutschrank funktionieren und sind daher sehr klein.

In dieser Arbeit werden Bildverarbeitungsmethoden für diese Systeme (in unterschiedlichen Entwicklungsstufen) vorgestellt. Diese Methoden machen das System benutzbar für die Zellüberwachung in einem Brutschrank. Dies ist ein Hauptbeitrag der Arbeit. Es werden Analysen des Mikroskopsytems und seiner Komponenten gezeigt, die die Entwicklung des Systems unterstützten. Ein Verfahren zur Kalibrierung und Algorithmen zur automatischen Anpassung der Beleuchtung und der Fokusposition werden eingeführt. Vorverarbeitungsschritte wie die Korrektur von Beleuchtungsinhomogenitäten und eine Kontrastverbesserung verbessern die Bildqualität.

Eine Bildverarbeitungsbibliothek und eine Zellüberwachungssoftware, die diese Bibliothek benutzt, wurden entwickelt. Ein Algorithmus zur Auszählung der Zellen wurde in die Bildverarbeitungsbibliothek portiert. Merkmale zur Beurteilung der Lebensfähigkeit von Zellen wurden untersucht und auch in die Bildverarbeitungsbibliothek übernommen.

Ein weiterer Hauptbeitrag bezieht sich generell auf Hellfeldmikroskope. Sie zeigen folgenden Effekt: Die Fokussierung von sehr dünnen Objekten (Phasenobjekten) unterscheidet sich von der Fokussierung von dickeren Objekten, die weniger lichtdurchlässig sind. Dieser Effekt wird genau untersucht, erklärt und die Berechnung mehrerer nützlicher Fokuspositionen für Phasenobjekte wird abgeleitet. Der optische Fokus kann für Verfahren zur Rekonstruktion der Phase verwendet werden. In leicht defokussierten Bildern besitzen kleine Details einen sehr hohen Kontrast. Diese Bilder können für die Segmentierung von Zellen oder die Analyse der Zellen verwendet werden. In stärker defokussierten Bildern besitzen die Zellgrenzen einen sehr hohen Kontrast. Diese Bilder können für die Zelldetektion verwendet werden.

## Acknowledgment

This thesis was written at the pattern recognition lab of the Friedrich-Alexander-Universität Erlangen-Nürnberg and at the company ASTRUM IT GmbH. I want to thank the following people of both institutions for their support.

At the pattern recognition lab first of all I would like to thank my supervisor Prof. Dr.-Ing. Joachim Hornegger for giving me the chance to work on this PhD thesis. I also want to thank my group heads Eva Kollorz, Dr.-Ing. Andreas Maier and Dr.-Ing. Stefan Steidl for supporting me and my work. I would like to thank my roommates Simone Gaffling, Willhelm Haas and Firas Mualla for having such a great time together. My special thanks go to Firas Mualla. We were a great team and I really enjoyed our fruitful discussions and our collaborative work!

At ASTRUM IT GmbH I want to thank Walter Greul, Ralph Steidl and Thomas Kammerer for giving me this chance and for supporting my work and the according research project.

Finally, I want to thank my parents, my brother and his family and all my friends for being patient with me during the time of this thesis.

Simon Schöll

# Contents

# Chapter 1

# Introduction

## 1.1 Cell Biology

Humans and trees are living while stones and sand are not. The main difference between organisms and materials is that organisms consist of cells. Therefore, cells are the basic building blocks of life [Albe 05]. These small units have the exceptional property to produce copies of themselves by growing and dividing. The simplest living organisms are single cells. Complex organisms such as humans consist of trillions of cells that form cellular collectives such as tissues or organs.

Cells are very different in their appearance. Cell diameter can vary from some micrometres to one millimetre [Albe 05]. The shape can be round or particularly long (e.g. typical nerve cells in the brain). Despite external differences, cells share common chemical properties regarding their basic functions.

All organisms are classified into two categories: eukaryote and prokaryote. The difference between them is that the cells of a prokaryote (e.g. a bacterium) do not have nuclei while the cells of an eukaryote (e.g. an animal or a plant) have [Albe 05]. In this thesis, the term *cell* is used for an eukaryotic animal cell unless explicitly stated otherwise. An animal cell with its main organelles is depicted in Figure 1.1. The most important cell parts for this thesis are described in the next sections.

### 1.1.1 Plasma Membrane

The plasma membrane is the physical border of the cell. On the one hand, it prevents the mixing of intra- and extracellular components in order to protect the cell. On the other hand, it enables the selective exchange of substances. A cell needs chemical energy from outside to survive and at the same time end products have to leave the cell [Klin 03].

### 1.1.2 Cytoplasm

The cytoplasm is the whole inner part of the cell besides the nucleus. It consists of the cytosol, the cytoskeleton, and the organelles. The organelles (e.g. mitochondria) are the internal components inside a cell that are limited by a membrane. The cytosol is the gel-like liquid inside the cell [Albe 05].

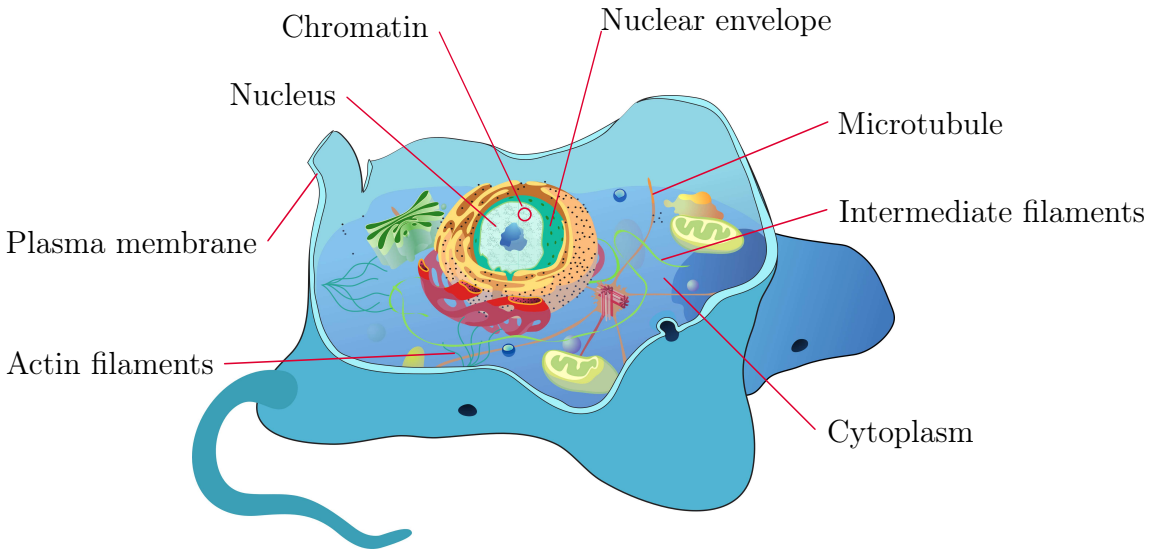


Figure 1.1: Typical animal cell [Stru]

### 1.1.3 Cytoskeleton

The cytoskeleton traverses the whole cell and has different functions depending on the cell type. As the word implies, it can stabilize the shape of the cell with its fine protein filaments and microtubules [Klin 03]. However, the functions of the cytoskeleton outreach the implication of the word „skeleton“. The microtubules are also responsible for the movement of the whole cell and control intracellular transport processes [Klin 03].

### 1.1.4 Nucleus

The nucleus is the most prominent organelle inside an eukaryotic cell. It is separated from the cytoplasm by two concentric membranes that are called nuclear envelope. In the chromatin, the nucleus contains the genetic information of the organism in form of deoxyribonucleic acids (DNA) [Klin 03].

## 1.2 Cell Culture

Cell culture is defined as the growth and proliferation of living cells under sterile conditions in a culture medium [Lang 13]. One challenge in cell culture technology is to prevent cultures from contamination. This risk is high because culture media are not only stimulating the growth of cells but also of microorganisms [Lang 13]. To avoid contamination, different working areas are separated by filtered clean air and antibiotics are added to the culture medium [Lang 13]. Nevertheless, the sterility of the cell culture should be controlled continuously. This is mostly done visually using a microscope.

The production of antibodies or drugs, and toxicity tests are exemplary use cases for cell cultures [Lang 13]. In toxicity tests, the toxic impact of particular substances

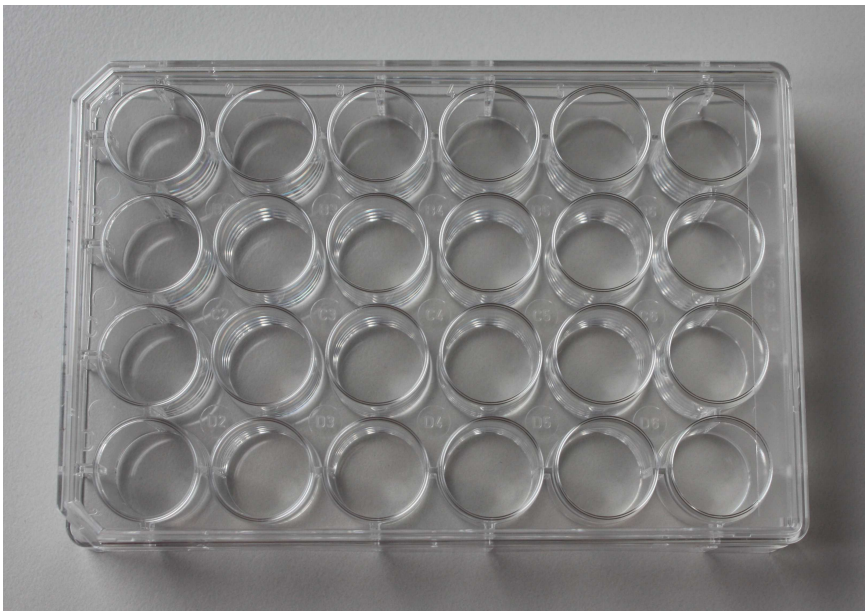

Figure 1.2: Microtiter plate with 24 wells

to cells or isolated tissues is monitored. By these tests on cell cultures, the amount of animal tests can be reduced that are necessary for the development of new active substances. Toxicity tests also enable research on the action mechanisms of toxic substances.

### 1.2.1 Incubator

In order to ensure a stable environment, cell cultures are kept in an incubator [Lang 13]. The incubator controls for example the carbon dioxide ($CO_2$) content, the temperature, and the humidity [Lang 13].

### 1.2.2 Culture Vessel

Cells can be grown on glass or plastic vessels. Differently shaped plastic containers are widespread and often used as culture vessels. They are mostly disposable and the vendors deliver them sterile and ready for use [Lang 13]. The determining factor for the choice of a culture vessel is the area required for the expected cell count. The most relevant culture vessel for this thesis is the microtiter plate. The number of wells in a microtiter plate ranges from 6 to 384. For this thesis, microtiter plates with 24 wells (see Figure 1.2) are used. They have a growth surface of 2.0 $cm^2$ per well and the recommended volume of the culture medium is $0.5 - 0.75$ ml [Gstr 13].

### 1.2.3 Cell Line

Cells normally stop dividing after a certain amount of cycles [Klin 03]. For lung fibroblasts (cells of the connective tissue) taken from 100-year-old persons, the ability to divide stops considerably earlier than for cells from children [Silb 05]. Only some cells are immortal. These cells are called continuous cell lines and they are used for

research and production. Established continuous cell lines with defined properties are deep-frozen and can be purchased from cell banks such as the *American Type Culture Collection*.
The relevant cell lines for this thesis are:

- CHO (ovary cells from the Chinese hamster)
- L929 (mouse fibroblasts)
- SF21 (ovary cells from larvae of *Spodoptera frugiperda*, a moth species)

### 1.2.4 Culture Medium

Cells need a special environment to be able to grow and divide outside the organism. A culture medium forms such an environment and preserves, for instance, the pH value at $7.2 - 7.4$ [Lang 13]. The recipe for a culture medium is chosen according to the requirements of the cultivated cell line. Cells are sensitive to different culture media compositions. The choice of the culture medium influences, for instance, the yield of cell products. A large number of different recipes can be found in the literature.

A medium for cell culture normally consists of a basal medium and nutrient supplements [Gstr 13]. Glutamine and pyruvate are examples for nutrient supplements. For many combinations of cell lines and basal media, a serum has to be added in order to enable or improve growth. A serum can originate from different animals and different development stages [Gstr 13]. The only relevant serum for this thesis is the fetal calf serum (FCS).
The relevant basal media [Gstr 13] for this thesis are:

- *Dulbecco's Modified Eagle Medium (DMEM)*: universal medium that is often used for animal cells [Dulb 59].
- *Hams Nutrient Mixtures*: developed by Richard Ham for CHO cells.
  - *Ham's F-10*: the composition of the medium is derived from exactly reproduced experiments with CHO cells [Ham 63].
  - *Ham's F-12*: further development of Ham's F-10 that makes serum-free cultivation of CHO cells possible [Ham 65].
- *Dulbecco's Modified Eagle Medium / Nutrient Mixture F-12 (DMEM/F-12)*: a 1:1 mixture of DMEM and Ham's F-12 that is often used as basal medium for serum-free cultivations.

### 1.2.5 Adherence and Suspension

A cell culture is called adherent if the cells adhere to the surface of the culture vessel. In contrast, suspension cells grow without adhering to a surface. Whether cells grow in suspension or adherent depends on various factors such as the cell line, the culture medium, and the culture vessel. Mammalian cells (e.g. CHO or L929) are mostly cultivated adherent [Gstr 13].

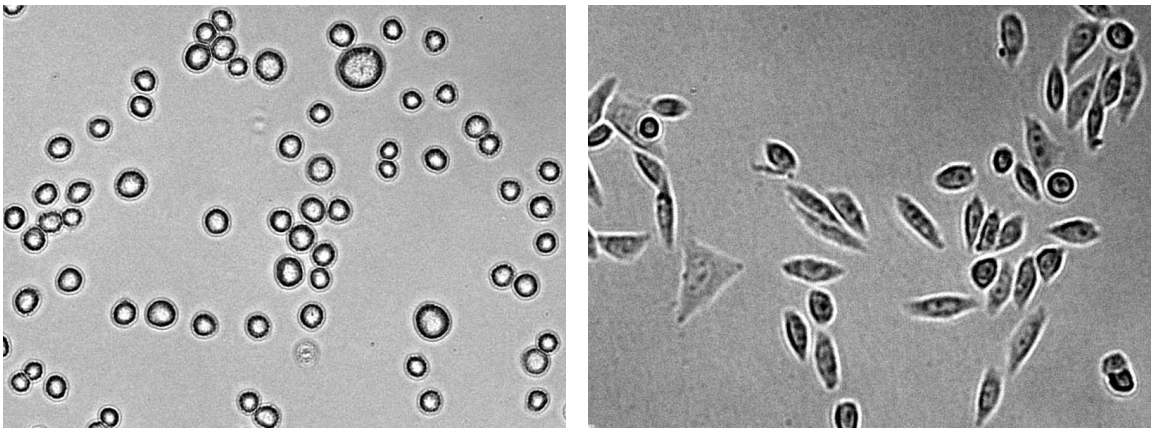

(a) Cells are in suspension after seeding out

(b) Cells become adherent after some cultivation time

Figure 1.3: Images of CHO cells at different stages of cultivation (images are contrast enhanced for clarity)

Adherent and suspension cells have different visual appearance. Figure 1.3 shows this difference for CHO cells. Figure 1.3a shows suspended cells with typical spherical shape. The cells lie on the bottom of a microtiter plate. In Figure 1.3b thin and stretched adherent cells are presented. They mostly show an elongated shape.

Cells of an adherent cell culture are sometimes in the suspension state. For example, after they are seeded in the culture medium. A cell also changes its state to suspension for dividing. After the division both resulting cells go back into the adherence state. For moving cells from one vessel to another, adherent cells need to be detached from the surface. For this purpose enzymes such as trypsin or accutase are added to the cell culture [Gstr 13].

## 1.3 Cell Culture Analysis

Many cell cultures are cultivated in parallel in the incubator. To be able to compare all these individual cell cultures, different parameters are observed and measured. Microscopes are used to check the morphological appearance. The microscope types that are relevant for this thesis are described in Section 1.3.1. Afterwards, methods to determine the cell count and the cell viability are described in Section 1.3.2.

### 1.3.1 Microscopes

Cells are normally very small and not visible to the naked eye. The invention of the light microscope in the $17^{\text{th}}$ century led to their discovery [Albe 05]. In the 1660s, Robert Hooke used different lenses to inspect objects and described his observations in the book *Micrographia* [Hook 65]. For the small objects which he saw when observing a piece of cork, he introduced the term „cell“. Although he described at that time the walls of dead plant cells the word cell remained to this day [Albe 05].

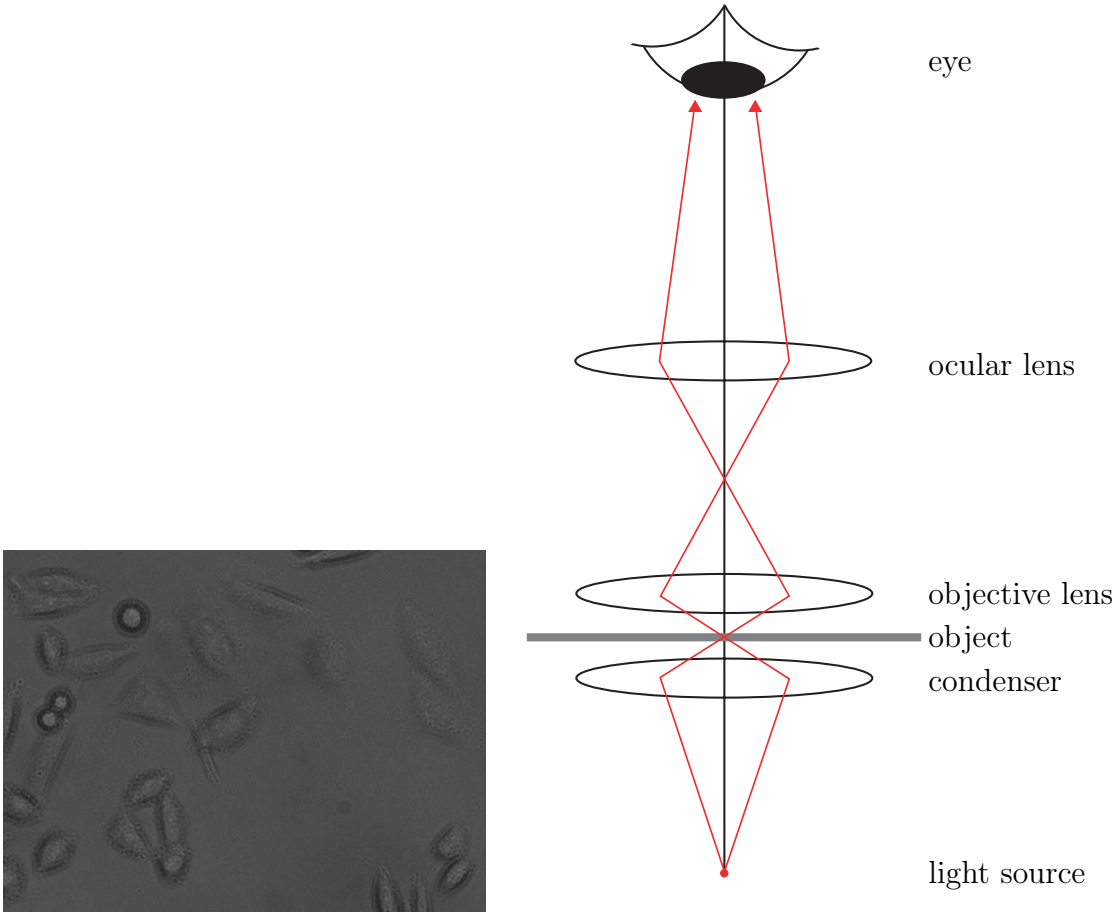


(a) Bright field micrograph at focus (b) Setup and beam path

Figure 1.4: Bright field microscopy

Optical microscopes are the most common and popular microscopes [Ghat 10] and part of the basic equipment of a cell biologist. They use visible light and different lenses to enlarge small samples and make their details visible. An optical microscope can resolve details up to a size of 0.2 µm [Albe 05]. This limit is given due to the wave nature of the visible light and not due to lens quality. The three types of optical microscopes that are relevant for this thesis are described in the following sections. First, bright field illumination is described. Second, the phase contrast microscope is introduced and finally the fluorescence microscope is specified.

### Bright Field Microscope

Bright field is an illumination technique in optical microscopy. Visible light is transmitted through an object and the amount of absorption by object parts is responsible for the visible differences in the resulting image. The path of light in a bright field microscope is illustrated in Figure 1.4b. Light from a light source (commonly halogen

light bulbs are used) reaches the condenser that focuses it on the observed object. The objective lens creates an inverted and magnified image of the object [Hech 09]. The ocular lens focuses the light for the human eye to see a magnified virtual image. To get digital magnified images, the ocular lens is replaced by a camera.

The magnification and the numerical aperture (NA) are the descriptive parameters of objective lenses. The numerical aperture is given by [Hech 09]:

$$\mathrm{NA} = n \sin \theta_{\max}, \tag{1.1}$$

where $n$ is the refractive index of the medium surrounding the objective lenses. The angle $\theta_{\max}$ is half of the maximal opening angle of the light beam that the objective lens can collect. The objective lenses for a microscope can be exchanged to achieve different magnifications. For this thesis, the Nikon Eclipse TE2000U microscope was frequently used. Exemplary parameters are listed in Table 1.1.

| **magnification** | **numerical aperture** |
|---|---|
| 10 times (10X) | 0.30 |
| 20 times (20X) | 0.45 |

Table 1.1: Parameters for two objective lenses

The contrast in a bright field image rises when the amplitude of the transmitted light wave is degraded by the imaged object. Objects are called *amplitude objects* if their contrast in the resulting image results from a diminished amplitude of the light wave [Hech 09]. Especially thin adherent cells hardly reduce the amplitude of the visible light. Therefore, they are almost invisible in the resulting images. A bright field image of adherent CHO cells is shown in Figure 1.4a. Such optically thin objects that do not change the amplitude of the light wave but instead shift their phase are called *phase objects*. This phase shift is invisible to the human eye in bright field microscopy [Hech 09].

One way to make cells and their components visible in bright field microscopy is to stain them [Albe 05]. Commonly used stains for bright field microscopy are trypan blue and neutral red. Neutral red is bound in living cells and stains them red. If the plasma membrane of a cell is damaged, trypan blue can penetrate into the cytoplasm and stain the cell bluish [Schm 11].

### Phase Contrast Microscope

In 1934, Frits Zernike developed the phase contrast microscope that makes the phase shift of light visible. For this invention he was awarded the Nobel Prize in Physics in 1953 [Pope 11]. The path of the light and the most important parts of a phase contrast microscope are shown in Figure 1.5b. In contrast to a bright field microscope, two additional hardware parts are used. The condenser annulus is an aperture between the light source and the condenser that forms a ring-shaped illumination. The phase plate is placed behind the objective lens. After the light has passed a phase object two kinds of waves are present: Firstly, the unscattered direct waves with high amplitude and without phase changes. Secondly, phase changed diffraction waves with low

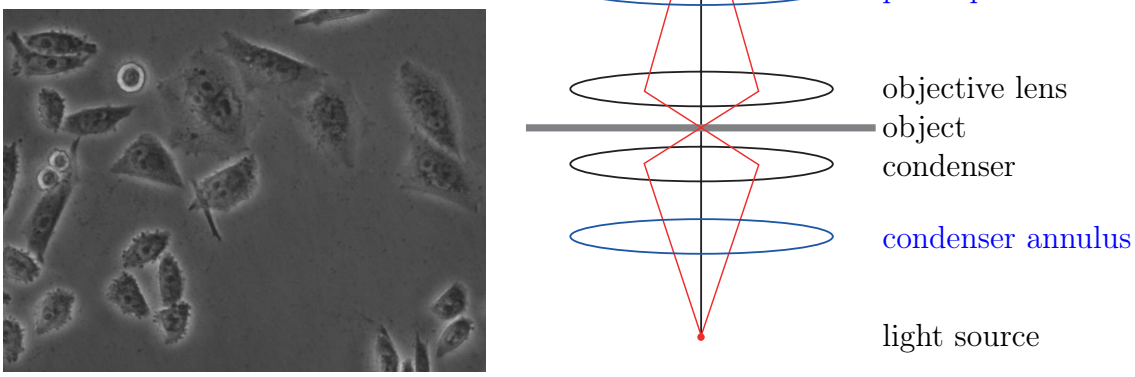


(a) Phase contrast micrograph at focus (b) Setup and beam path

Figure 1.5: Phase contrast microscopy

amplitude. The phase plate shifts the phase of the direct waves (formed by the condenser annulus) by $\frac{\pi}{2}$. As a result both waves superpose and interfere and the phase objects (e.g. cell details) become visible at the image plane. [Hech 09, Pope 11].

A phase contrast microscope is standard equipment for analysing cell cultures because it allows to observe thin living mammalian cells [Gstr 13]. An acquired image of adherent CHO cells is shown in Figure 1.5a. The improvement compared to the bright field image of the same cells in Figure 1.4a is remarkable.

### Fluorescence Microscope

Fluorescent dyes can be added to a cell culture. They normally bind to specific cell parts such as the nuclei. These fluorescent dyes are invisible in bright field microscopy. Compared to the bright field setup, two filters are added in fluorescence microscopy (see Figure 1.6b). The excitation filter blocks all wavelengths except the one that excites the dye. While fluorescing, the dye emits another specific wavelength. The emission filter blocks every wavelength except the emitted one [Albe 05]. The resulting images are therefore black with one colour visible (see Figure 1.6a).

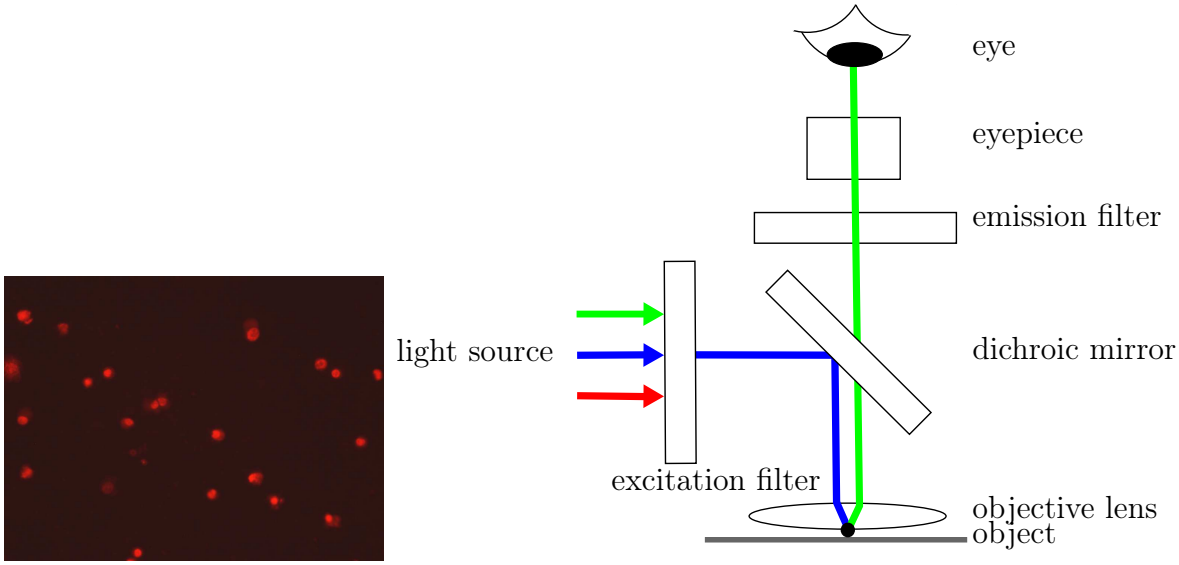


(a) Fluorescence micrograph (b) Setup and beam path

Figure 1.6: Fluorescence microscopy

Fluorescence microscopes are equipped with different emission filters that can be exchanged. For example, the used Nikon Eclipse TE2000U microscope was equipped with a red, a blue, and a green channel. The setup of this microscope can be modified so that it can be used to acquire micrographs with the three fluorescence channels, with a bright field setup or with a phase contrast setup.

Often all fluorescence channels are used in parallel to combine different information. It is for example possible to use the blue channel for the nucleus of all cells, the red channel for dead cells and the green channel to stain living cells. The red stain in Figure 1.6a is propidium iodide (PI) and dyes dead cells.

### 1.3.2 Cell Count and Cell Viability

Cells are sensible to the environment and the culture medium composition. Contamination can happen or the cells need a recovering phase before they start growing. Monitoring the growth of each cell culture in the incubator is important. In the daily routine, different parameters are obtained. One parameter that is monitored using a microscope is the morphology of the cells. Another parameter that is routinely observed is the cell count, i.e. the number of living cells per µl.

The most common method for determining the number of viable cells is the trypan blue method [Lang 13]. For using this method the cells have to be in the suspension state. Then trypan blue is added to the cells. The cells are homogeneously distributed with a pipette and a sample of 0.9 µl [Gstr 13] is loaded into a hemocytometer (see Figure 1.7). A hemocytometer is a glass or plastic chamber with a fixed grid of lines. It consists of nine large squares that are again subdivided into smaller squares. For the relevant cell cultures such as CHO cells the outer four squares are used for

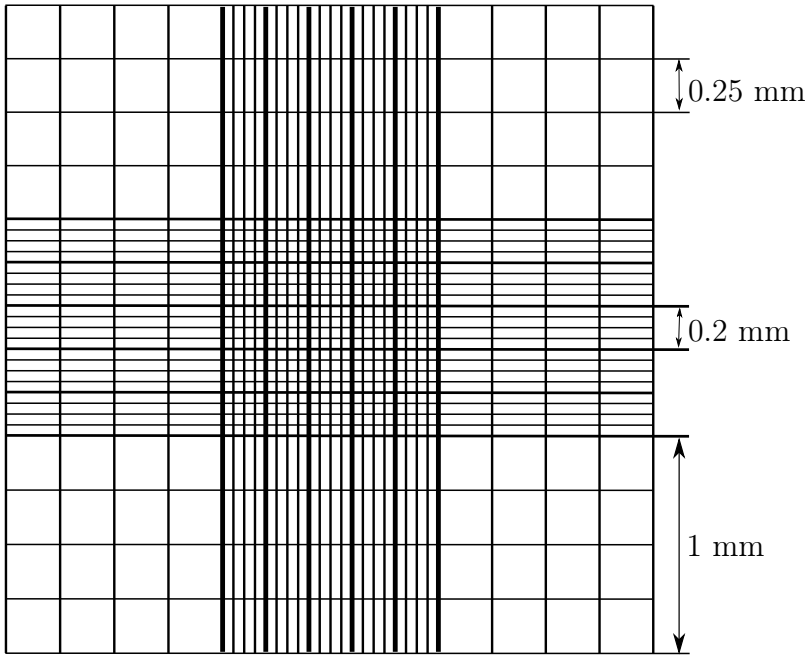


Figure 1.7: Hemocytometer for determining the cell count

determining the cell count. After the hemocytometer is filled, it is placed under the microscope and focused. The cells in each of the four relevant chambers are counted. The unstained cells are the number of living cells. After the four numbers are counted, their mean value is calculated and mapped to the total amount of liquid of the cell culture.

The cell count for a cell culture is mostly determined at different time points. The results are plotted into a graph with semi logarithmic scale. This graph is called growth curve (see Figure 1.8). The x-axis shows the time points with linear scale and the y-axis shows the cell count with logarithmic scale. The manual counting is very time-consuming and done approximately once a day for mammalian cells such as CHO.

The cell viability can also be determined with the hemocytometer. In addition to the number of living cells the number of dead cells is also counted. The viability is the percentage of living cells. In the trypan blue method, it is calculated by dividing the number of unstained (living) cells by the sum of unstained and stained cells.

## 1.4 Research Project COSIR

The term COSIR is an acronym and stands for „**C**ombination of Chemical-**O**ptical **S**ensors and **I**mage **R**ecognition“. It is the name of a research project that was funded by the Bavarian Research Foundation under the contract number AZ-917-10 in the years 2011–2013. Four partners worked on this project:

- PreSens Precision Sensing GmbH, Regensburg
- ASTRUM IT GmbH, Erlangen

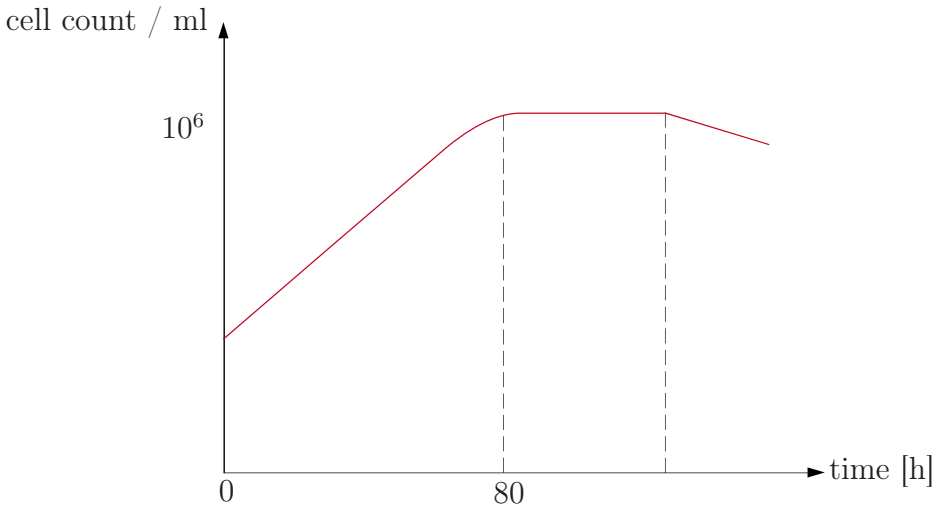


Figure 1.8: The number of cells over the time is displayed in a growth curve

- Pattern Recognition Lab, Friedrich-Alexander-Universität Erlangen-Nürnberg
- Institute of Bioprocess Engineering, Friedrich-Alexander-Universität Erlangen-Nürnberg

They used their diverse expertise and knowledge to develop a system for the non-invasive observation of cell cultures in microtiter plates with 24 wells.

Cell cultivation is usually done in an incubator but the analysis is performed while the cell culture is outside. This is a problem because microscopes for observing the cell morphology are large devices that do not fit into an incubator and also do not fulfil the other requirements for operating in an incubator. The dyes that are used for the analysis are influencing and often killing the cells. For instance, cell counting has to be done shortly after adding trypan blue to the culture because the dye is cytotoxic and therefore the number of dead cells increases after waiting a longer time [Lang 13]. The COSIR hardware system was developed to operate in an incubator. Twenty-four small microscopes are part of the system with a size smaller than the well size. The space for the hardware was therefore limited to a squared region with a side length of approximately 2 cm. For the final hardware prototypes, a sensor for measuring the pH and a sensor for measuring the partial pressure of dissolved oxygen (DO) was added for each well.

Within the project, a cell culture monitoring software was developed. This software is adapted to the needs of cell biologists, uses the developed hardware prototypes, and includes the image processing algorithms. The developed software systems and the image processing library are described in Chapter 6.

## 1.5 Structure of this Thesis

During the term of the research project COSIR image processing algorithms were developed to

- control the hardware systems of different development stages,

- support the hardware development,
- preprocess and
- analyse the acquired images

The investigated research questions and algorithms to solve them are described in the chapters 2 – 5.

## 1.6 Contribution to the Progress of Research

The main contributions of the thesis can be assigned to two categories: bright field microscopy, and novel miniature microscopy systems. In the following, the main items are briefly introduced. Detailed information can be found in the corresponding chapters of this thesis.

**Bright field microscopy**

1. Focusing of very thin (phase) objects such as CHO cells differs from focusing of objects that are thicker and less transparent for light. This effect is investigated in detail, explained, and different useful focus positions for phase objects are derived [Scho 14a]. The optical focus position can be used for applications such as phase retrieval. Slightly defocused cell images with a maximum in contrast at small details can be used for applications such as cell segmentation or cell analysis. Strongly defocused cell images with a maximum in contrast for the cell borders can be used for applications such as cell detection. To understand how to automatically focus at these different positions is a main contribution.

2. Knowledge was gained about phase objects, focusing [Scho 14a], and phase retrieval [Weig 13]. The low-pass monogenic local phase (LMLP) was used by our group to improve the accuracy of cell/background classification [Mual 14a]. The LMPL and transport of intensity equation (TIE) solution were used by Mualla et al. to improve joint learning of adherent and suspended cell detection [Mual 14b].

3. Some promising results were achieved for unstained cell viability detection [Heer 13]. For the given bright field data it was shown that dead cells can be differentiated from living cells.

**Novel miniature microscopy systems**

1. Algorithms were developed for or applied to novel miniature microscopy systems at different development stages. A calibration procedure was defined. Algorithms for automatic exposure and automatic focusing were developed. Algorithms for illumination correction and contrast enhancement were applied. As second main contribution the algorithms made these prototype systems usable for cell observations in an incubator [Scho 14b].

2. The algorithms were applied to the prototype systems in an early state of development. Therefore, they could be used to analyse the behaviour of the systems. The benefit of these analyses was that the development of the systems could address issues and fix them.

# Chapter 2

# Hardware Control

This chapter explains the algorithms used for controlling the different miniature bright field microscopy prototypes that were developed within the research project COSIR (see Section 1.4). First, in Section 2.1 the different prototype development stages and their characteristics are described. Second, the calibration procedure for a prototype system is explained in Section 2.2. Third, the algorithms for automatically selecting a suitable exposure time and their adaption to the prototypes are shown in Section 2.3. Fourth, in Section 2.4, focusing of phase objects such as adherent CHO cells is investigated in detail and conclusions for bright field microscopy are drawn. Finally, the algorithm for automatic focusing of COSIR systems is described in Section 2.5.

## 2.1 COSIR Hardware

Within the COSIR project, three major hardware setups were developed. They are listed in Table 2.1.

| **Name** | **Number of microscopes** | **pH-sensors** | **DO-sensors** |
|---|---|---|---|
| COSIR-1 | 1 | No | No |
| COSIR-2 | 2 | Yes | Yes |
| COSIR-24 | 24 | Yes | Yes |

Table 2.1: Different COSIR hardware setups

COSIR-1 was used to test the feasibility of the miniature concept and to select the hardware components. One specific setup of this early development stage is depicted in Figure 2.1. This setup was very unstable. Next, COSIR-2 was used to duplicate the camera system and to include pH- and DO-sensors. This prototype was a bit more stable even though in this system the hardware components were exchanged and moved several times.

The COSIR-24 systems included miniature microscopes for all 24 wells of a microtiter plate. Such a system is shown in Figure 2.2. The hardware components were fixed and could not be moved any more. One microscope of a prototype system

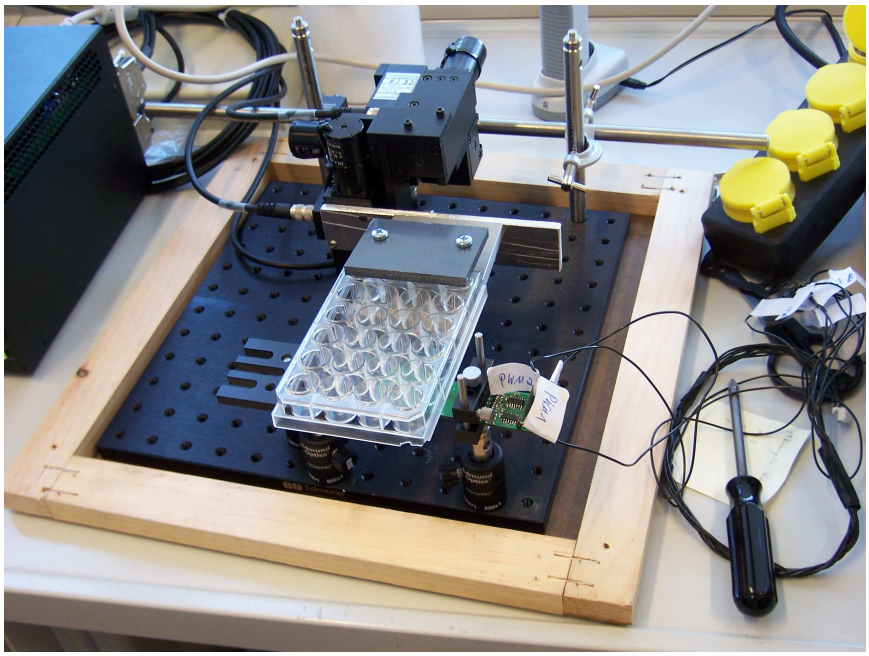

Figure 2.1: COSIR prototype system with one microscope

is also called channel. The prototype systems introduced above have one, two, or twenty-four channels.

## 2.2 Calibration

The calibration procedure described in this section was developed by the author of this thesis. It is applicable to all prototype systems and the basis for the algorithms described in the following sections.

As described in Section 1.4, the prototype systems are developed to operate inside an incubator for observing cell cultures. Hence, the systems normally work in a dark environment. Working with living cells in a laboratory is restricted. Therefore, the calibration and the development of some algorithms were mostly done outside the laboratory and without cells. In order to simulate the stable dark illumination environment of an incubator, the prototype systems were put inside a box (see Figure 2.3).

In the calibration procedure, the four parameters listed in Table 2.2 were determined for each channel of a prototype system.

| **Calibration parameter** | **Description** |
|---|---|
| $t_0$ | Initial exposure time |
| $E_{\text{const}}$ | Constant illuminance |
| $f_0$ | Initial focus position |
| $ROI_{\text{IlluminationCentre}}$ | Image region around the illumination centre |

Table 2.2: Calibration parameters for COSIR systems

Figure 2.2: COSIR prototype system with 24 microscopes

First, the two parameters related to the exposure are determined. The luminous exposure $H$ [lxs] is the amount of light energy on a given area during a given exposure time. It is defined [Ohno 97] as the product of the illuminance at the image plane $E$ [lx] and the exposure time $t$ [s]:

$$H = E \cdot t. \tag{2.1}$$

In the COSIR systems, both parameters can be tuned separately and belong to two different hardware parts. The exposure time $t$ is a parameter of the image sensor and the illuminance $E$ is a tunable parameter of the light-emitting diode (LED).

The initial exposure time $t_0$ was set to 700 ms in accordance with the project partners. For capturing an image of a cell culture (after the whole calibration procedure), the exposure time is adapted to the actual illumination environment and the imaged object. This automatic adjustment of the exposure time is described in Section 2.3.

The second calibration parameter that is related to the exposure is the illuminance ($E_{\text{const}}$). It is determined manually after setting $t_0$. This parameter stays constant for all further images acquired with this channel.

After $t_0$ and $E_{\text{const}}$ are applied to a channel, the third parameter $f_0$ is determined manually. Well plates filled with water and glass beads are used to do this calibration step without cells outside of a laboratory. The focus position is changed until the objects are visible as well as possible. The determined parameter $f_0$ is the starting point for finding a focus position automatically (see Section 2.5).

The hardware components of the COSIR microscope systems are combined in an extremely limited space. Because of this manufacturing constraint, the LED

Figure 2.3: Prototype systems are put inside a box to ensure a dark environment equal to an incubator

is positioned close to the object. This causes a circular illumination field at the centre of the image plane. When the image centre is not overexposed, the outer corners of the image area are underexposed and not usable. As a consequence, the hardware manufacturer defined a region of $1 \times 1$ mm$^2$ around the centre of the circular illumination as supported image area.

The position and size of the supported image region is the forth calibration parameter $ROI_{\text{IlluminationCentre}}$. Finding this region is done automatically and divided into two steps. First, the centre of illumination is detected. Second, the supported image region $ROI_{\text{IlluminationCentre}}$ is positioned according to it. A cell image with the circular illumination artefact is shown in Figure 2.4. The determined results for the centre of illumination and the $ROI_{\text{IlluminationCentre}}$ are drawn in this cell image with green colour.

For determining the centre of the circular illumination, the cells in the image are removed by a convolution with a Gaussian filter. The filter kernel is given by

$$G(x, y) = \frac{1}{\sqrt{2\pi}\sigma^2} e^{-\frac{x^2+y^2}{2\sigma^2}}, \tag{2.2}$$

where $x$ and $y$ are the horizontal and vertical distances to the origin of the kernel, and $\sigma$ is the standard deviation. The parameter $\sigma$ is experimentally set to 40 pixels according to the size of CHO cells on images acquired with COSIR prototype systems. The kernel size was set to $6\sigma + 1 = 241$. After applying this filter to a prototype cell image, the cells are removed. The resulting image is therefore an estimation of the illumination field. The centre of gravity of all pixels with maximum intensity in the estimated illumination field is calculated $(x_{\text{Centre}}, y_{\text{Centre}})$. This point is the illumination centre.

The image of a prototype system has a resolution of $2592px \times 1944px$. For the prototypes COSIR-1 and COSIR-2 a square region of $1 \times 1$ mm$^2$ corresponds to a side

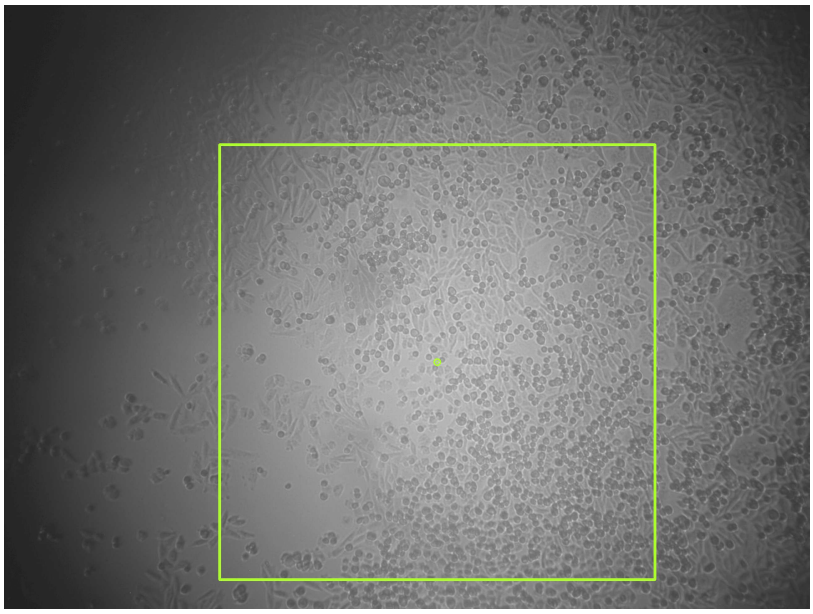

Figure 2.4: Detected centre of illumination and the corresponding region of interest are drawn on a CHO micrograph created with COSIR-2

length ($ROI_{\text{SideLength}}$) of 1400 pixels. For COSIR-24 the corresponding side length is 1500 pixels. The start coordinates of the ROI are determined using the centre of illumination ($x_{\text{Centre}}, y_{\text{Centre}}$):

$$\begin{aligned} x_{\text{ROIstart}} &= x_{\text{Centre}} - \frac{ROI_{\text{SideLength}}}{2} \\ y_{\text{ROIstart}} &= y_{\text{Centre}} - \frac{ROI_{\text{SideLength}}}{2} \end{aligned} \tag{2.3}$$

The determined ROI ($x_{\text{ROIstart}}$, $y_{\text{ROIstart}}$, $ROI_{\text{SideLength}}$, $ROI_{\text{SideLength}}$) is corrected in two cases:

1. If the coordinates are odd, they are shifted by 1 to fulfil the requirements of the image sensor.

2. If a part of the ROI is outside the image, it is shifted towards the image centre.

After the $ROI_{\text{IlluminationCentre}}$ is determined for a channel, it is applied for all further image acquisitions with this channel.

For the unstable systems COSIR-1 and COSIR-2, the three parameters $t_0$, $E_{\text{const}}$, and $f_0$ had to be calibrated for each experiment. $ROI_{\text{IlluminationCentre}}$ had to be determined before each image acquisition. For the stable COSIR-24 system, the calibration procedure was changed to reduce the runtime for acquiring 24 images. The calibration procedure is applied once for each channel and the resulting parameters are stored in a calibration file.

In order to determine the $ROI_{\text{IlluminationCentre}}$ of a COSIR-24 system, the following procedure was introduced. The wells of the microtiter plate are filled with water and an overexposed image is acquired. The circular overexposed region has to lie inside

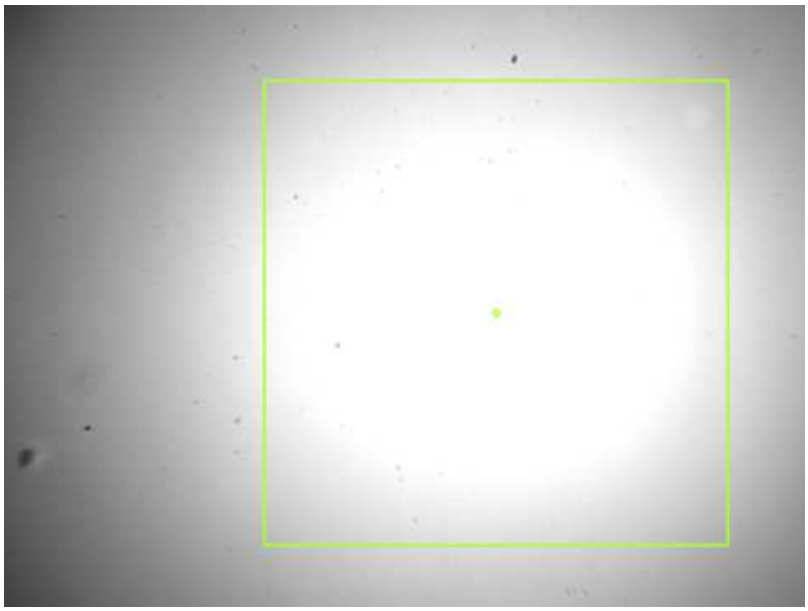

Figure 2.5: Overexposed image with detected centre of illumination and the corresponding region of interest

the image. The algorithm described above is applied to the image to determine $ROI_{\text{IlluminationCentre}}$. An example is shown in Figure 2.5.

## 2.3 Automatic Exposure

In overexposed or underexposed image parts, all pixels have the same value. Therefore, no contrast is available and the information is completely lost. The methods in this section automatically adapt the illumination time (see Section 2.2). The goal of this adaptation is a suitable luminous exposure to avoid over- or underexposed images. The methods developed for and adjusted to the prototype systems are described in Section 2.1.

The following reasons are responsible for the changes of the illumination conditions:

- The development constraints for the miniature microscope systems are the reason for a radial illumination field with dark edges and a bright centre (see Section 2.2 and Figure 2.5).
- The images of the prototype systems were sometimes over- or underexposed compared to the image taken before, even though the parameters used did not change.
- An experiment with cells takes normally days or even weeks. While it is running in an incubator, the illumination environment can change
  - because the incubator door is opened or closed.
  - because the well plate is removed and returned back (e.g. for exchanging the culture medium).

  - because the prototype system (including the well plate) is moved inside the incubator.

- When experiments are done outside the incubator (e.g. with glass beads), the illumination environment can also change

  - because of the time-dependent influence of the sunlight.
  - because of different light sources inside the room that are turned on or off.
  - because of the shadows from persons or objects.

Normally, the illumination conditions are stable during an experiment. Nevertheless, some of the events listed above can occur even between two consecutive images. Therefore, two different methods for automatic adaption were developed. First, a fast method to check each image and correct wrong exposure was developed. This method is described in Section 2.3.1. Second, the exposure time is adapted at the beginning of an experiment. The details of this algorithm are shown in Section 2.3.2.

### 2.3.1 Adaption for each Image

Each image is checked if it is over- or underexposed. The classification is done based on the following criteria:

$$\begin{aligned} \text{OVEREXPOSED} &\textbf{ if } p_{255} > \alpha_{\text{overexposed}} \\ \text{UNDEREXPOSED} &\textbf{ if } p_0 > \alpha_{\text{underexposed}} \\ \text{NORMALEXPOSED} &\textbf{ if } p_{255} > \alpha_{\text{overexposed}} \textbf{ and } p_0 > \alpha_{\text{underexposed}}, \end{aligned}$$

where $p_{\text{i}}$ is the probability of a pixel with intensity $i$:

$$p_i = \frac{h(i)}{NM}, \tag{2.4}$$

where $h(i)$ is the number of pixels with intensity $i$. The parameters $\alpha_{\text{overexposed}}$ and $\alpha_{\text{underexposed}}$ were experimentally set to 0.01.

If an image is OVEREXPOSED, the exposure time is decreased until the resulting image is not overexposed any more. One correction step is given as

$$t_i = t_{i-1} - t_{\text{step}}, \tag{2.5}$$

where $t_{\text{step}}$ is the step size of the exposure time. For all automatic adaptions of the exposure of COSIR systems, $t_{\text{step}}$ is set to 50 ms.

In the same way, the exposure time is increased until the resulting image is not underexposed any more if an image is UNDEREXPOSED. One step is

$$t_i = t_{i-1} + t_{\text{step}}. \tag{2.6}$$

### 2.3.2 Adaption at the Beginning of an Experiment

At the beginning of a measurement (a series of images over time) a suitable exposure time is determined automatically. The calibration described in Section 2.2 yields square images. For the algorithm in this section, only the inner part of the square image is used to consider the circular illumination and to avoid an overexposed image centre. The corresponding ROI is given by ($x_{\text{illumination}}$, $y_{\text{illumination}}$, SideLength, SideLength), where

$$\begin{aligned} x_{\text{illumination}} &= \frac{ROI_{\text{SideLength}}}{4} \\ y_{\text{illumination}} &= \frac{ROI_{\text{SideLength}}}{4}. \end{aligned} \tag{2.7}$$

Algorithm 1 shows the procedure used for adjusting the exposure time. According to the hardware specification the input parameters $t_{\min}$ and $t_{\max}$ were set to 0 ms and 1600 ms. The parameter $\sigma_{\text{thresh}}$ was experimentally set to 0.01.

## 2.4 Phase Object Focus

The most important target cell line for the research project COSIR was the CHO cell line. CHO cells mostly adhere to the bottom of the well. Therefore, the cells are very thin and nearly transparent. It turned out that algorithms for automatic focusing behave unexpected for such cells. Therefore, many experiments and evaluations were done to investigate this unexpected behaviour. These experiments were done with a standard bright field microscope to be independent from the prototype hardware. In the following sections, the experiments and results are described. First, in Section 2.4.1, the related work and the scientific contribution are presented. In Section 2.4.2, the focus measures are explained and the phase effect in Section 2.4.3. The bright-field cell image materials that were acquired and used for the study are described in Section 2.4.4. A presentation of the evaluation scheme and a report of our experimental observations follows in Section 2.4.5. Finally, we discuss and interpret these results in Section 2.4.6.
Considerable parts of this section were published in [Scho 14a].

### 2.4.1 Related Work and Contribution

The accuracy and reliability of the focus measure is essential for the quality of the resulting images. Focused images are desirable because they contain more information compared to defocused images [Yeo 93].

An imaging system is considered at-focus if the light rays originating from a single point in the object plane converge to a single point in the image plane [Hech 09]. The focused image is commonly obtained by selecting the image plane for which a focus measure achieves its global maximum. The one-dimensional function of a focus measure for different $z$-positions is called a focus curve. There are several studies comparing different focus measures [Sun 04, Yu 10, Osib 10, Fire 91]. The choice of an appropriate measure depends on the type of microscope and the object

**Algorithm 1** Automatic Exposure Adaption at the Beginning of an Experiment

**procedure** AUTOADAPTINTEGRATIONTIME($t_{\text{start}}, t_{\text{step}}, t_{\text{min}}, t_{\text{max}}, \sigma_{\text{thresh}}$)
  $t_{\text{final}} \leftarrow t_{\text{start}}$
  $I_{\text{current}} \leftarrow$ GETIMAGE($t_{\text{start}}$)
  $\sigma_{\text{max}} \leftarrow$ GETSTANDARDDEVIATION($I_{\text{current}}$)
  $AfterMax \leftarrow 0$
  $isUnderexposed \leftarrow$ false
  $t_{\text{loop}} \leftarrow t_{\text{start}} - t_{\text{step}}$
  **while** $t_{\text{loop}} > t_{\text{min}}$ **and** $iAfterMax < 2$ **and** $isUnderexposed =$ false **do**
    $I_{\text{loop}} \leftarrow$ GETIMAGE($t_{\text{loop}}$)
    $\sigma_{\text{loop}} \leftarrow$ GETSTANDARDDEVIATION($I_{\text{loop}}$)
    **if** $I_{\text{loop}}$ is UNDEREXPOSED **then**
      $isUnderexposed \leftarrow$ true
    **else if** $|\sigma_{\text{max}} - \sigma_{\text{loop}}| > \sigma_{\text{thresh}} \cdot \sigma_{\text{max}}$ **then**
      **if** $\sigma_{\text{loop}} > \sigma_{\text{max}}$ **then**
        $\sigma_{\text{max}} \leftarrow \sigma_{\text{loop}}$
        $t_{\text{final}} \leftarrow t_{\text{loop}}$
      **else**
        $iAfterMax++$
      **end if**
    **end if**
    $t_{\text{loop}} \leftarrow t_{\text{loop}} - t_{\text{step}}$
  **end while**
  $iAfterMax \leftarrow 0$
  $isOverexposed \leftarrow$ false
  $t_{\text{loop}} \leftarrow t_{\text{start}} + t_{\text{step}}$
  **while** $t_{\text{loop}} < t_{\text{max}}$ **and** $iAfterMax < 2$ **and** $isOverexposed =$ false **do**
    $I_{\text{loop}} \leftarrow$ GETIMAGE($t_{\text{loop}}$)
    $\sigma_{\text{loop}} \leftarrow$ GETSTANDARDDEVIATION($I_{\text{loop}}$)
    **if** $I_{\text{loop}}$ is OVEREXPOSED **then**
      $isOverexposed \leftarrow$ true
    **else if** $|\sigma_{\text{max}} - \sigma_{\text{loop}}| > \sigma_{\text{thresh}} \cdot \sigma_{\text{max}}$ **then**
      **if** $\sigma_{\text{loop}} > \sigma_{\text{max}}$ **then**
        $\sigma_{\text{max}} \leftarrow \sigma_{\text{loop}}$
        $t_{\text{final}} \leftarrow t_{\text{loop}}$
      **else**
        iAfterMax++
      **end if**
    **end if**
    $t_{\text{loop}} \leftarrow t_{\text{loop}} + t_{\text{step}}$
  **end while**
  **return** $t_{\text{final}}$
**end procedure**

imaged [Redo 12]. Comparisons of focus measures for bright field (BF) microscopy have been conducted for objects that are amplitude objects such as tissue slices [Gao 10, Yazd 08, Redo 12], micropipette tips [Yu 10], pap smear [Liu 07], blood smear [Makk 09, Yu 10] or sputum smear [Osib 10, Kimu 10].

Bright field microscopy is the simplest light microscopy technique [Ghat 10] and thus it is cheap and widely used. An inherent problem in bright field images is the lack of sufficient contrast. In fact, for some very thin and almost transparent objects such as adherent cells, the imaged objects are barely visible at-focus [Ager 03, Ali 11a]. However, by defocusing the microscope, it is possible to increase the contrast and thus make these objects visible [Ager 03]. This contrast is proportional to the Laplacian of the light phase [Ager 03]. Therefore, we refer to this phenomenon of obtaining more contrast through defocusing by the term phase effect.

In this thesis, we show that the typical use of focus measures is likely to fail in the presence of the phase effect. The following observations were made:

- If the images show homogeneous cells, i.e., if most cells tend to lie in the same focal plane, the optical focus is at a local minimum of gradient-based focus measures.

- Inhomogeneous cells lead to characteristic focus curves for gradient-based focus measures due to the constructive overlapping of differently shaped focus curves from different image regions.

- For both homogeneous and inhomogeneous cells, statistic-based focus measures tend to have a local minimum instead of a global maximum at the focus position.

- For homogeneous cells, experts prefer focus settings that diverge considerably from the optical focus.

### 2.4.2 Focus Measures

As [Groe 85] stated, the image obtained by a microscope can be modelled as a convolution between an ideal image and a low-pass point spread function. The blurring introduced by the latter is proportional to the defocus distance and leads to decreased high spatial frequency content inside the resulting image. Therefore, focus measures use the high frequency content inside an image in order to automatically pick the image at optical focus. They tend to have a global maximum at the focus position.

Extensive comparisons of focus measures can be found in [Sun 04, Sant 97]. Below, the investigated focus measures are listed. They are split into gradient- and statistic-based measures. The two groups and the reason for the assignment of their members will become clear in the Section 2.4.5.

#### Gradient-based focus measures

In all equations $I$ is the considered image, $x$ and $y$ are the spatial pixel coordinates.

1. The Tenenbaum gradient (TEN) focus measure [Yeo 93, Sun 04] is given by the following equation:

$$F_{TEN} = \sum_{x,y} \left( [I(x,y) * S_x]^2 + [I(x,y) * S_y]^2 \right) \approx \sum_{x,y} \|\nabla I(x,y)\|_2^2 \tag{2.8}$$

where $*$ denotes the 2D convolution operator, $\|\cdot\|_2$ is the Euclidean distance, while $S_x$ and $S_y$ are the Sobel filter kernels:

$$S_x = \begin{pmatrix} -1 & 0 & 1 \\ -2 & 0 & 2 \\ -1 & 0 & 1 \end{pmatrix} \qquad S_y = \begin{pmatrix} 1 & 2 & 1 \\ 0 & 0 & 0 \\ -1 & -2 & -1 \end{pmatrix} \tag{2.9}$$

2. The squared gradient (SQGRAD) focus measure [Sant 97] is given by:

$$F_{SQGRAD} = \sum_{x,y} \Big( I(x,y) - I(x+1,y) \Big)^2 \tag{2.10}$$

3. The Brenner focus measure [Bren 76, Sun 04] is given by:

$$F_{BRENNER} = \sum_{x,y} \Big( I(x-1,y) - I(x+1,y) \Big)^2 \tag{2.11}$$

4. The autocorrelation (AUTOCOR) focus measure [Voll 88, Sun 04] is given by:

$$F_{AUTOCOR} = \sum_{x,y} I(x,y)\, I(x+1,y) - \sum_{x,y} I(x,y)\, I(x+2,y) \tag{2.12}$$

5. The wavelet focus measure [Yang 03] is given by:

$$F_{WAVELET} = \sum_{x,y} \left( |W_{HL}(x,y)| + |W_{LH}(x,y)| + |W_{HH}(x,y)| \right) \tag{2.13}$$

where $W_{HL}$, $W_{LH}$ and $W_{HH}$ are the level-1 subbands of the wavelet transform. The wavelet base is Daubechies 6 [Daub 92].

6. The Fourier focus measure [Lian 12] is given by:

$$F_{FOURIER} = \sum_{u,v} \Big( \sqrt{u^2 + v^2} \cdot \left| \mathcal{F}(u,v) \right| \Big) \tag{2.14}$$

where $u$ and $v$ are coordinates in frequency domain and $\mathcal{F}$ is the Fourier transform of the image where the zero-frequency component is shifted to the centre of the Fourier spectrum.

**Statistic-based focus measures**

7. The normalized variance (NVAR) focus measure [Sun 04] is given as follows:

$$F_{NVAR} = \frac{1}{NM\mu} \sum_{x,y} \Big( I\left(x,y\right) - \mu \Big)^2 \tag{2.15}$$

where $\mu$ is the mean intensity value in the image and $N$ and $M$ are the image width and height in pixels, respectively.

8. The entropy focus measure [Fire 91] is given by:

$$F_{ENTROPY} = -\sum_{i} p_i \log_2 \left(p_i\right) \tag{2.16}$$

**Patch-wise decomposition**

Images can consist of objects with different focus positions. To investigate the focus behaviour of such images it is helpful to split a focus measure of the whole image into focus measures of image parts.

The following formula can be derived for gradient-based focus measures such as TEN:

$$F_{\text{Gradient}} = \sum_{x=1}^{N} \sum_{y=1}^{M} \|\nabla I(x,y)\|_2^2 = \sum_{k=1}^{P} \sum_{x=x_{1,k}}^{x_{2,k}} \sum_{y=y_{1,k}}^{y_{2,k}} \|\nabla I(x,y)\|_2^2 \tag{2.17}$$

The image is divided into $P$ disjoint patches covering the whole image. The coordinates $x_{1,k}$,$x_{2,k}$ are the start and the end $x$ coordinates of the $k$-th patch. In the same way, $y_{1,k}$,$y_{2,k}$ are defined for the $y$ coordinate. According to Equation 2.17, the gradient-based focus measure of an image can be seen as the sum of $P$ measures, each of which is computed for one of the $P$ patches.

### 2.4.3 Phase Object Focusing

**Phase effect**

Phase objects at-focus are shown in Figure 2.6b. They are almost invisible [Ager 03, Ali 11a, Beca 11]. Their contrast can be improved by defocusing the imaging system. According to [Ager 03], the contrast obtained by defocusing is given by:

$$C(x,y) = \frac{I(x,y) - I_0(x,y)}{I_0(x,y)} = \frac{\Delta z}{\kappa} \nabla^2 \phi(x,y) \tag{2.18}$$

where $C(x,y)$ is the contrast at the pixel position with spatial coordinates $x$ and $y$, $\Delta z$ is the distance between the plane of the at-focus image $I_0$ and the plane of the defocused image $I$, $\nabla^2\phi(x,y)$ is the Laplacian of the physical phase of light at point $x,y$ and $\kappa$ is the wavenumber. The image is considered positively defocused when the objective approaches the object and negative otherwise [Ager 03]. In Figure 2.6, bright field images of CHO cells at different $z$-positions are shown: negatively defocused (Figure 2.6a), at-focus (Figure 2.6b), and positively defocused (Figure 2.6c). Both, Figure 2.6a and Figure 2.6c show a considerable contrast increase compared to Figure 2.6b.

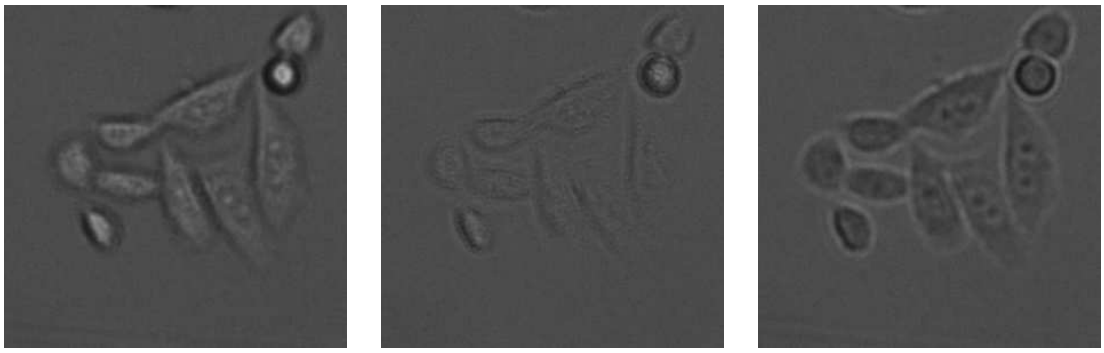

(a) At −30 µm (b) At-focus (c) At +30 µm

Figure 2.6: Bright field images of adherent CHO cells acquired at different distances according to the physical focus position

| **Object class** | **Object** | **No. of stacks** | **No. of images /stack** | $\Delta z$ (µm) |
|---|---|---|---|---|
| Amplitude | Tissue | 2 | 40 | 1 |
| Phase (homogeneous) | CHO-K1 | 11 | $23 \pm 2$ | 5 |
| Phase (inhomogeneous) | CHO-K1 | 12 | $25 \pm 2$ | 5 |

Table 2.3: Overview of the image data used for this work

#### Phase effect characteristic

In [Scho 14a], we introduced the term phase effect characteristic (PEC) to describe the case when there are two local maxima, A and B, and a local minimum C between them in a focus curve. Examples are shown in Figure 2.10 and explained in Section 2.4.5.

### 2.4.4 Materials

For the evaluation, we differentiate between three different types of stacks that are characterized in Table 2.3.

#### Amplitude objects

We used two stacks taken from an online database [Redo 12] as amplitude objects. These stacks show histopathological tissue samples of a biopsy and an autopsy. They have a resolution of $1392px \times 1040px$ and a $z$-distance of 1 µm. The focused image of the autopsy stack is shown in Figure 2.7.

#### Homogeneous phase objects

For phase objects, CHO-K1 epithelial-like cells were used. DMEM/F-12 (Invitrogen 21331-046) was used as the growth medium. It was combined with 10% fetal calf serum (PAA A15-102) and 4 mM Glutamine (Sigma-Aldrich G7513-100ML). The cells were precultured in T-25 polystyrene culture flasks (Sarstedt 83.1810) and maintained

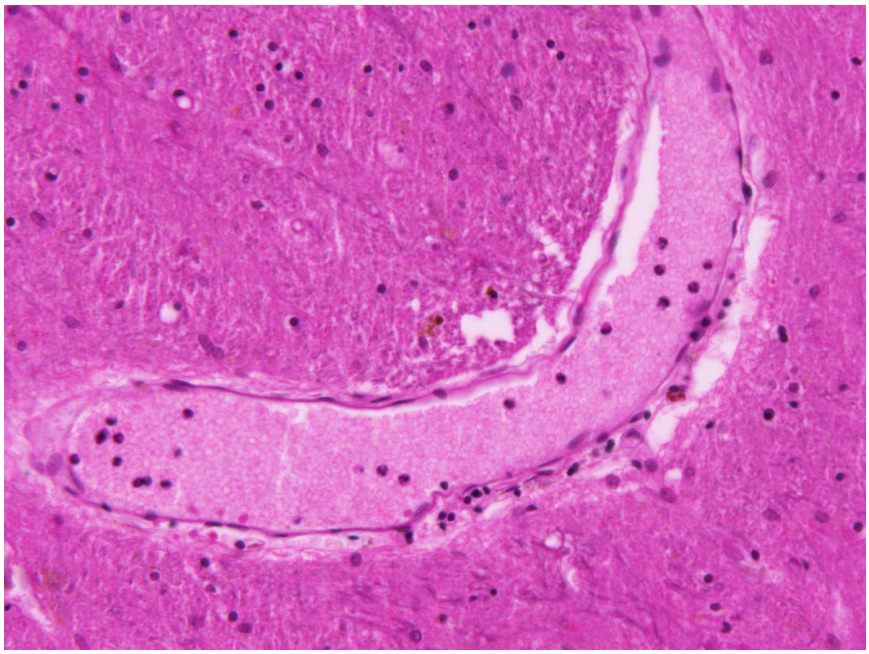

Figure 2.7: Image at-focus of an amplitude object

in the exponential growth phase. The atmosphere in the incubator was set to 37 °C and 7% $CO_2$.

As stated in the introduction, we use the term homogeneous stack to describe the situation when most cells in the imaged region tend to lie in the same focal plane. This case is likely to happen when the cells are separated and therefore are almost the same in thickness.

In order to obtain images that show separable cells, the following procedure was applied: The cell detachment solution AccutaseTM (Sigma-Aldrich A6964-100ML) was used to remove the cells from the T-Flask and to separate them. They were then seeded out in 24-well plates using a working volume of 600 µl of the described medium composition. In a second step, a crosswise movement of the well plate was used to distribute the cells in the wells.

After this process, it is possible to obtain separated cells. Two types of homogeneous stacks were acquired: suspension cell stacks after half an hour of cultivation and adherent cell stacks after 18 hours of cultivation.

### Inhomogeneous phase objects

After long cultivation times, cells agglomerate and thus form layers of different thickness. This leads to inhomogeneous stacks because different regions in the image will tend to have different focal planes. Such stacks were acquired after 42 hours of cultivation. Figure 2.8 illustrates the difference between homogeneous and inhomogeneous images.

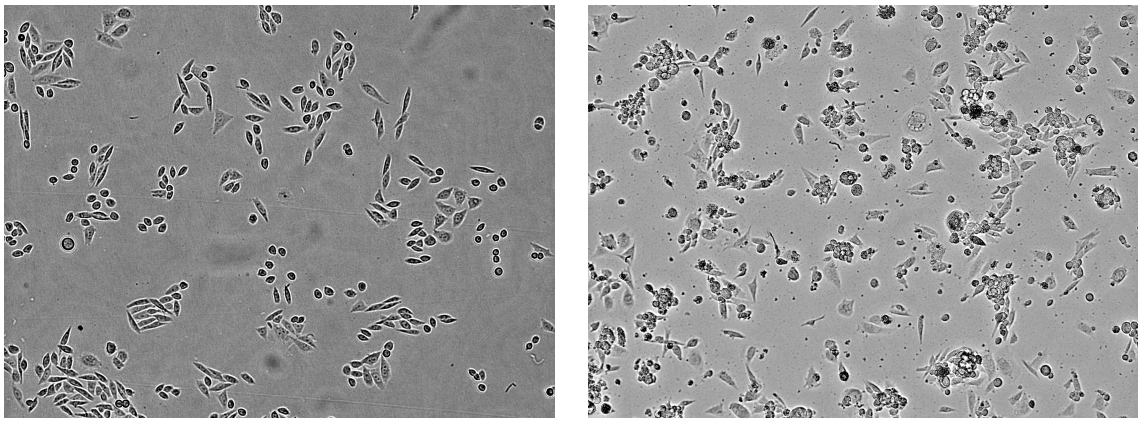

(a) Homogeneous image (b) Inhomogeneous image

Figure 2.8: The two different investigated classes of adherent CHO images

#### Image acquisition

All previously mentioned CHO-K1 stacks were acquired using an inverted Nikon Eclipse TE2000U microscope and a Nikon USB camera. A halogen light bulb for standard bright field microscopy was used to illuminate the cells appropriately. Two microscope objectives were used. The first had a magnification of 20 times, a numerical aperture of 0.45 and a working distance of 7.4 mm. The second objective had a 10 times magnification, a numerical aperture of 0.30 and a working distance of 15.2 mm. The image resolution was $2560px \times 1920px$ with 0.49 µm/pixel for the objective with 10 times magnification and 0.24 µm/pixel for the objective with 20 times magnification.

### 2.4.5 Evaluation

For each of the stacks described in Section 2.4.4, the focus curves were computed. For valid comparisons, a min-max normalization was applied to each focus measure $F$ to change its range linearly from $[F_{\min},F_{\max}]$ to [0, 1]. Afterwards, the extrema were localized.

#### Amplitude Objects

Figure 2.9 shows typical focus curves for an amplitude object. As expected, most focus curves of the tested data have one distinct maximum. For one stack, there is a second maximum in the WAVELET focus curve.

#### Homogeneous Cell Objects

Figure 2.10 shows the mean focus curves over all homogeneous stacks for all gradient-based focus measures. In Figure 2.11, the mean curves for the statistic-based methods are shown. Before computing the mean, all curves were aligned according to the NVAR minimum.

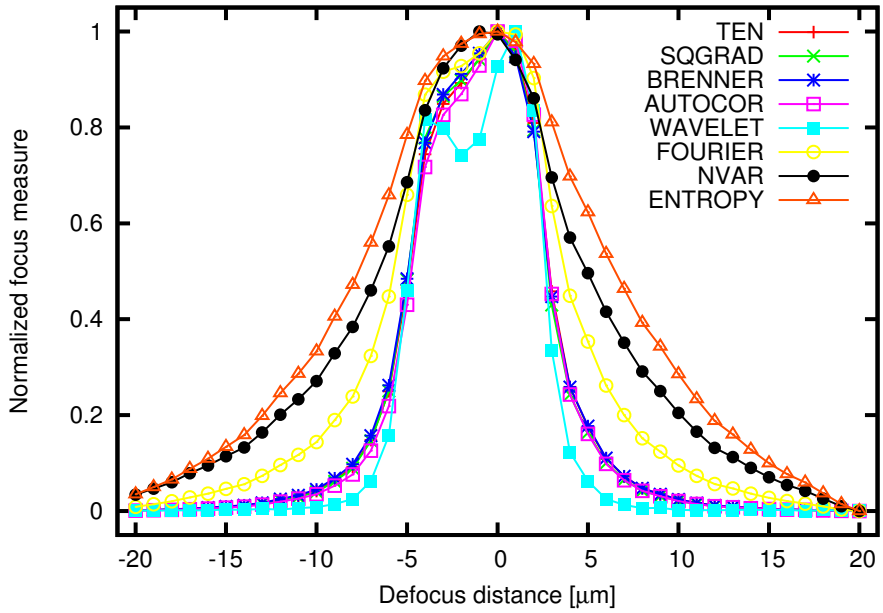


Figure 2.9: Focus curves for a stack of an amplitude object

In order to reduce the effect of noise, all PEC cases for which

$$F(A) - F(C) < 0.2 \tag{2.19}$$

or

$$F(B) - F(C) < 0.2 \tag{2.20}$$

were discarded. The $z$-positions A, B and C are described in the previous Section 2.4.3.

In Figure 2.10, the curves (except WAVELET) show exactly one PEC, whereas the mean curves in Figure 2.11 show exactly one prominent minimum. The six gradient-based focus measures were applied to the eleven homogeneous stacks. The observation of one PEC applies to 57 out of the 66 resulting focus curves. The WAVELET focus measure had one PEC only for five of the eleven stacks. The TEN, BRENNER and AUTOCOR focus measures showed one PEC for all stacks of our data. FOURIER showed two outliers, whereas SQGRAD showed one.

**Comparison with expert focus positions** For each of the homogeneous stacks, four bioprocess engineering experts of Friedrich-Alexander-Universität Erlangen-Nürnberg were asked to select the image at-focus. The results are shown in Figure 2.12. No expert chose the position determined by the global minimum of NVAR. The experts preferred a defocused image with increased contrast. As shown in Table 2.4, three quarters of the chosen focus positions were positively defocused.

Computing the mean expert focus position for each stack is not straightforward as illustrated in Figure 2.6. If, for instance, one expert chose −30 µm (Figure 2.6a) as the image at-focus and another expert chose +30 µm (Figure 2.6c), then the average distance will be 0 µm (Figure 2.6b) which is inherently different from what both experts chose. Consequently, as can be seen in Table 2.4, the focus distances in

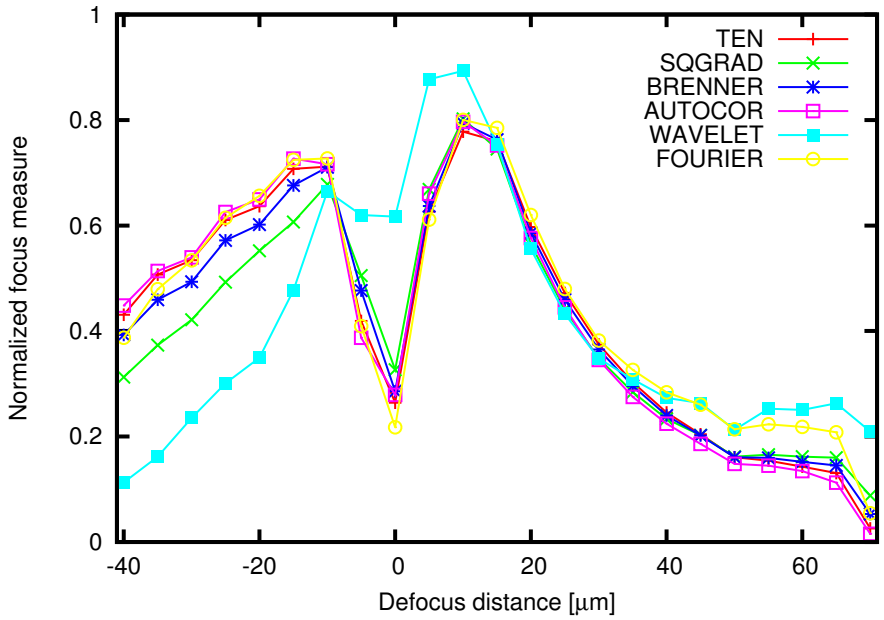


Figure 2.10: Mean gradient-based focus curves computed from all homogeneous stacks

| | **Ratio (%)** | **Distance to** $NVAR_{min}$ **(µm)** |
|---|---|---|
| **Positive defocused** | 75 | $21.97 \pm 12.99$ |
| **At-focus** | 0 | |
| **Negative defocused** | 25 | $10.91 \pm 4.37$ |

Table 2.4: Average focus positions of experts for all homogeneous stacks

Figure 2.12 were averaged at each side of the NVAR minimum. The average absolute distance of the expert focus position to the NVAR minimum was $19.20 \pm 12.39$ µm.

**NVAR minimum related to gradient-based focus measures** In this section, we compare the behaviour of gradient-based and NVAR curves of homogeneous stacks. For this purpose, we use the following measures:

$D(NVAR_{min}, FGRAD_{max})$: Distance in micrometres between the position at which the NVAR curve has its minimum and the position at which the gradient-based focus measure (FGRAD) has its global maximum.

$D(NVAR_{min}, FGRAD_{PEC,min})$: Distance in micrometres between the position at which the NVAR curve has its minimum and the position at which the gradient-based curve has its PEC minimum. Only the 57 curves with exactly one PEC were used to compute this measure.

Table 2.5 shows the results. We can see that the NVAR minimum was very close to the PEC minimum of the gradient-based curves. Please note that part of the error is a quantization error because there is a distance of 5 µm between two successive images in each stack. We can also see that, excluding the WAVELET focus measure, the maximum of the gradient-based curves had an average distance of about 10 µm

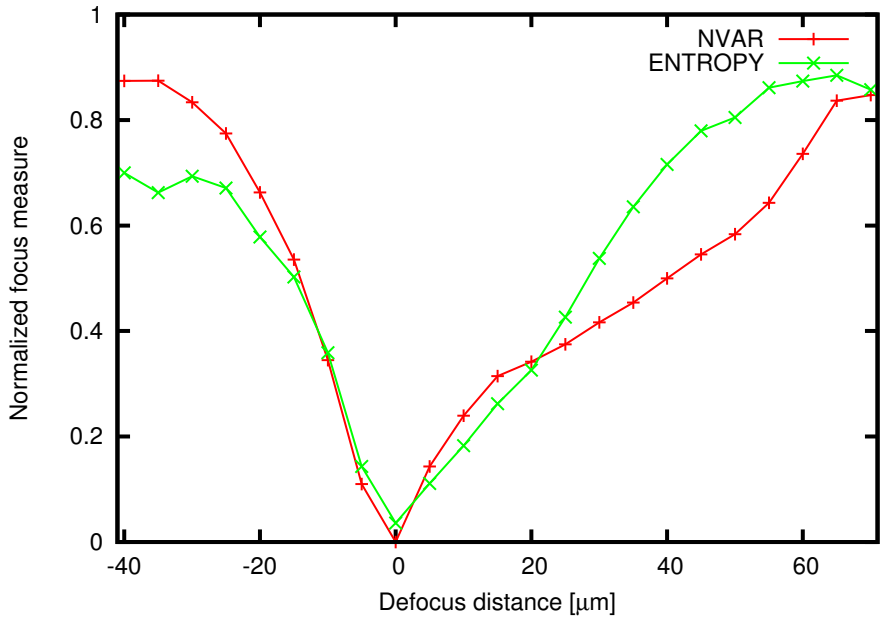


Figure 2.11: Mean statistic-based focus curves computed from all homogeneous stacks

| **Focus measure** | $D(NVAR_{min}, FGRAD_{max})$ (µm) | $D(NVAR_{min}, FGRAD_{PEC,min})$ (µm) |
|---|---|---|
| TEN | $10.9 \pm 6.3$ | $1.8 \pm 2.5$ |
| SQGRAD | $10.5 \pm 5.0$ | $3.5 \pm 6.3$ |
| BRENNER | $10.5 \pm 4.7$ | $1.4 \pm 2.3$ |
| AUTOCOR | $10.9 \pm 6.3$ | $1.8 \pm 2.5$ |
| WAVELET | $21.0 \pm 27.5$ | $5.0 \pm 8.7$ |
| FOURIER | $12.8 \pm 6.7$ | $1.7 \pm 2.5$ |

Table 2.5: Relation of gradient-based focus measures to NVAR for all homogeneous stacks

from the minimum of the corresponding NVAR curve. In general, the results for WAVELET differ significantly from the values of the other focus measures.

### Inhomogeneous Cell Objects

Figure 2.13 and Figure 2.14 show focus curves for two representative examples of the twelve inhomogeneous stacks. For both of them, the gradient-based curves have no PEC. In fact, all inhomogeneous stacks showed no PEC. While the gradient-based curves in Figure 2.13 look similar to the curves for an amplitude object, the gradient-based curves in Figure 2.14 show a partial similarity with the non-typical curves in Figure 2.10.

We investigate this point by performing a patch-wise analysis on the stacks. For our experiments, a patch size of $130px \times 130px$ was used. The resulting number of patches per stack was 300.

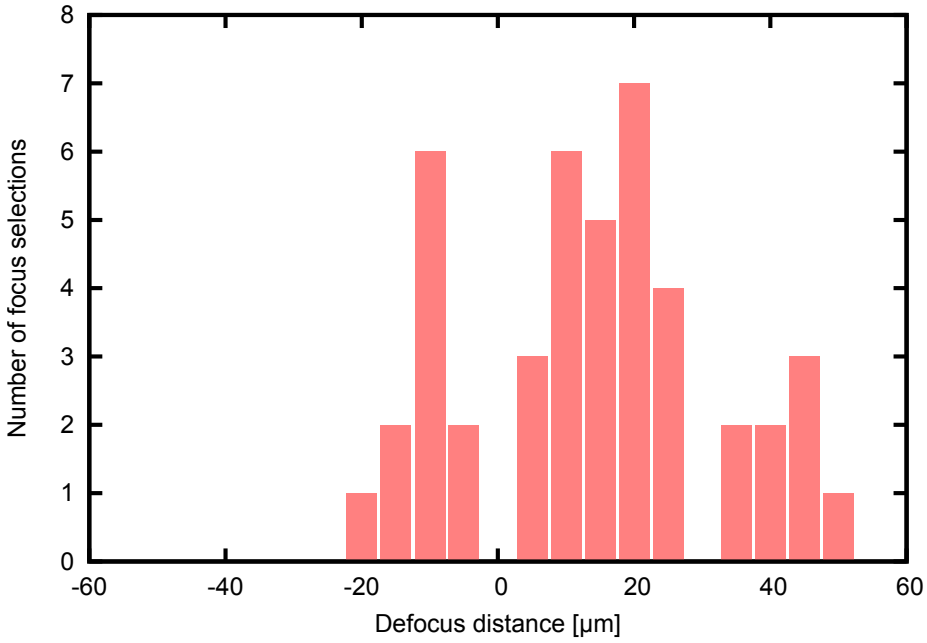


Figure 2.12: Distribution of the distances to the NVAR minimum reported by four bioprocess engineering experts for the eleven homogeneous stacks

For each patch, the focus curves and their number of PECs were computed. The results were grouped into three categories: no PEC (0PEC), one PEC (1PEC), and more than one PEC (>1PEC).

| **Focus measure** | **0 PEC (%)** | **1 PEC (%)** | **>1 PEC (%)** |
|---|---|---|---|
| TEN | $67.8 \pm 20.0$ | $29.9 \pm 19.3$ | $2.4 \pm 3.5$ |
| SQGRAD | $75.4 \pm 18.7$ | $20.8 \pm 17.0$ | $3.8 \pm 5.8$ |
| BRENNER | $71.8 \pm 20.3$ | $25.2 \pm 19.1$ | $3.0 \pm 4.8$ |
| AUTOCOR | $52.0 \pm 14.2$ | $27.8 \pm 7.4$ | $20.2 \pm 8.0$ |
| WAVELET | $75.1 \pm 14.1$ | $12.9 \pm 10.2$ | $12.1 \pm 9.9$ |
| FOURIER | $67.8 \pm 18.0$ | $27.3 \pm 15.8$ | $4.9 \pm 4.7$ |

Table 2.6: Phase effect characteristic distribution in gradient-based focus curves of image patches for all inhomogeneous stacks

Table 2.6 shows these values averaged over the patches of all inhomogeneous stacks. Combined for all focus measures, $68.3 \pm 18.9\%$ of the patches had no PEC and $24.0 \pm 16.0\%$ had one PEC. We noticed that the patches that showed no PEC tend to be dominated by agglomerations while the patches which showed one PEC tend to contain homogeneous cell regions. Figure 2.15 illustrates this observation.

The $z$-position of the maxima from patches without PEC ($FGRAD_{0PEC,max}$) and the local minima from patches with one PEC ($FGRAD_{1PEC,min}$) differ. The distances are shown in Table 2.7. The maxima lie in the positive focus direction compared to the local minima.

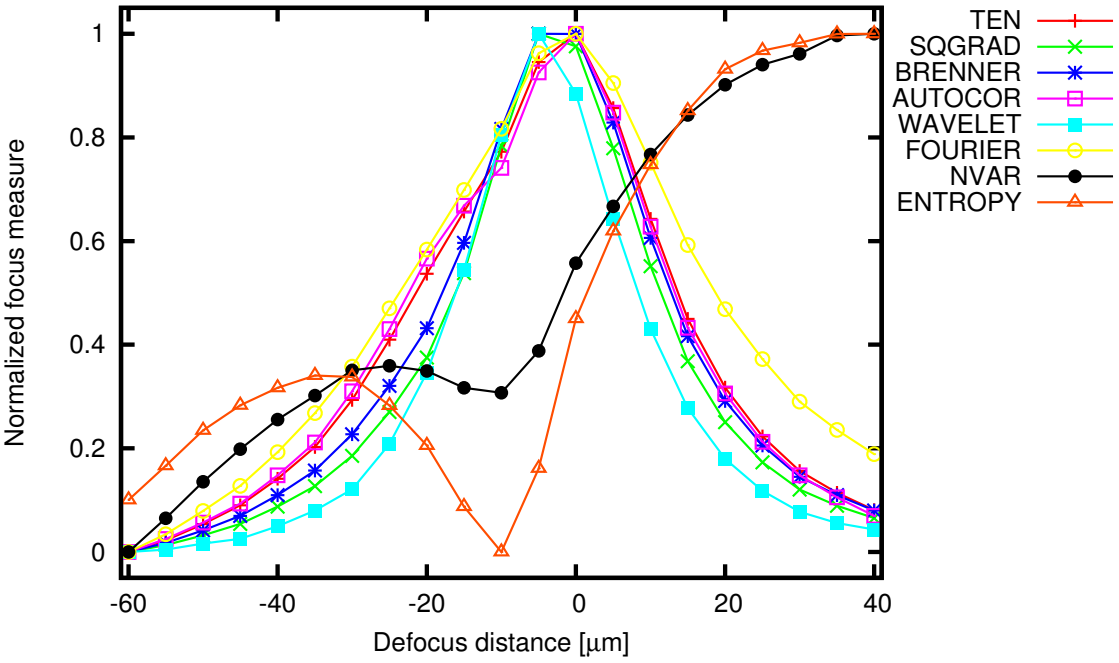


Figure 2.13: Exemplary focus curve (1) from an inhomogeneous stacks

| **Focus measure** | $D(FGRAD_{0PEC,max}, FGRAD_{1PEC,min})$ (µm) |
|---|---|
| TEN | $9.00 \pm 2.11$ |
| SQGRAD | $6.50 \pm 2.42$ |
| BRENNER | $7.00 \pm 2.58$ |
| AUTOCOR | $11.36 \pm 5.05$ |
| WAVELET | $6.67 \pm 2.58$ |
| FOURIER | $9.50 \pm 1.58$ |

Table 2.7: Distance between the focus positions of patches without PEC and patches with exactly one PEC for inhomogeneous stacks

Table 2.8 shows the result of the same process, i.e. patch-wise computation of focus curves, applied to the homogeneous stacks. Combined for all focus measures, $50.8 \pm 27.9\%$ of the patches had one PEC and $38.6 \pm 25.2\%$ had more than one PEC.

### 2.4.6 Conclusions and Discussion

The results for the homogeneous stacks of CHO-K1 cells show non-typical gradient- and statistic-based focus curves. By „non-typical“, we mean that they have different characteristics compared with the „typical“ focus curves which have one distinctive maximum at the optical focus position. This is due to the fact that defocusing in the presence of the phase effect increases not only blurring but also contrast.

Our results showed that most gradient-based focus curves for the homogeneous stacks have two maxima and one minimum between them. We called this the „phase effect characteristic“, which can be interpreted from the fact that the contrast is min-

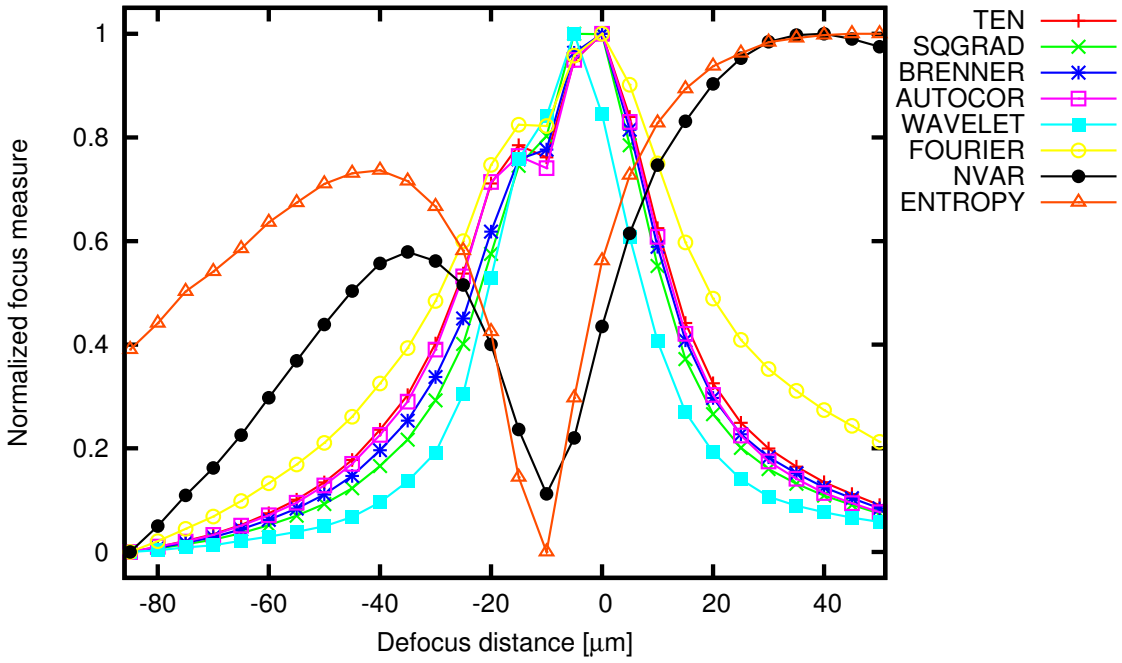


Figure 2.14: Exemplary focus curve (2) from an inhomogeneous stacks

| **Focus measure** | **0 PEC (%)** | **1 PEC (%)** | **>1 PEC (%)** |
|---|---|---|---|
| TEN | 5.5 ± 4.8 | 64.8 ± 23.9 | 29.7 ± 22.2 |
| SQGRAD | 9.4 ± 7.5 | 56.8 ± 24.2 | 33.8 ± 22.9 |
| BRENNER | 7.2 ± 5.1 | 59.6 ± 24.7 | 33.2 ± 22.3 |
| AUTOCOR | 9.9 ± 5.9 | 43.1 ± 31.7 | 47.0 ± 27.5 |
| WAVELET | 27.4 ± 34.1 | 22.2 ± 50.4 | 50.4 ± 27.1 |
| FOURIER | 4.5 ± 8.5 | 58.3 ± 28.7 | 37.2 ± 27.2 |

Table 2.8: Phase effect characteristic distribution in gradient-based focus curves of image patches for all homogeneous stacks

imized at-focus according to Equation 2.18. Defocusing increases the contrast and, thus, the gradient magnitude and the image variance, too. Blurring is also increased. Therefore, after a certain amount of defocusing, the blurring effect compensates the contrast gained by the phase effect. Consequently, the gradient magnitude and – to a lesser extent – the image variances decrease again.

Each statistic-based curve in our results for the homogeneous stacks has one distinctive global minimum. The optical focus of phase objects such as homogeneous CHO-K1 cells should conform to this global minimum. This can be justified by Equation 2.18.

The reason for the different behaviour of gradient- and statistic-based focus measures for homogeneous cells can be seen in Figure 2.16. When the microscope is defocused, small details inside cells and at cell borders become visible (Figure 2.16b, Figure 2.16d). These details are responsible for the maxima of the gradient-based focus measures. Further defocusing increases the contrast, while blurring removes

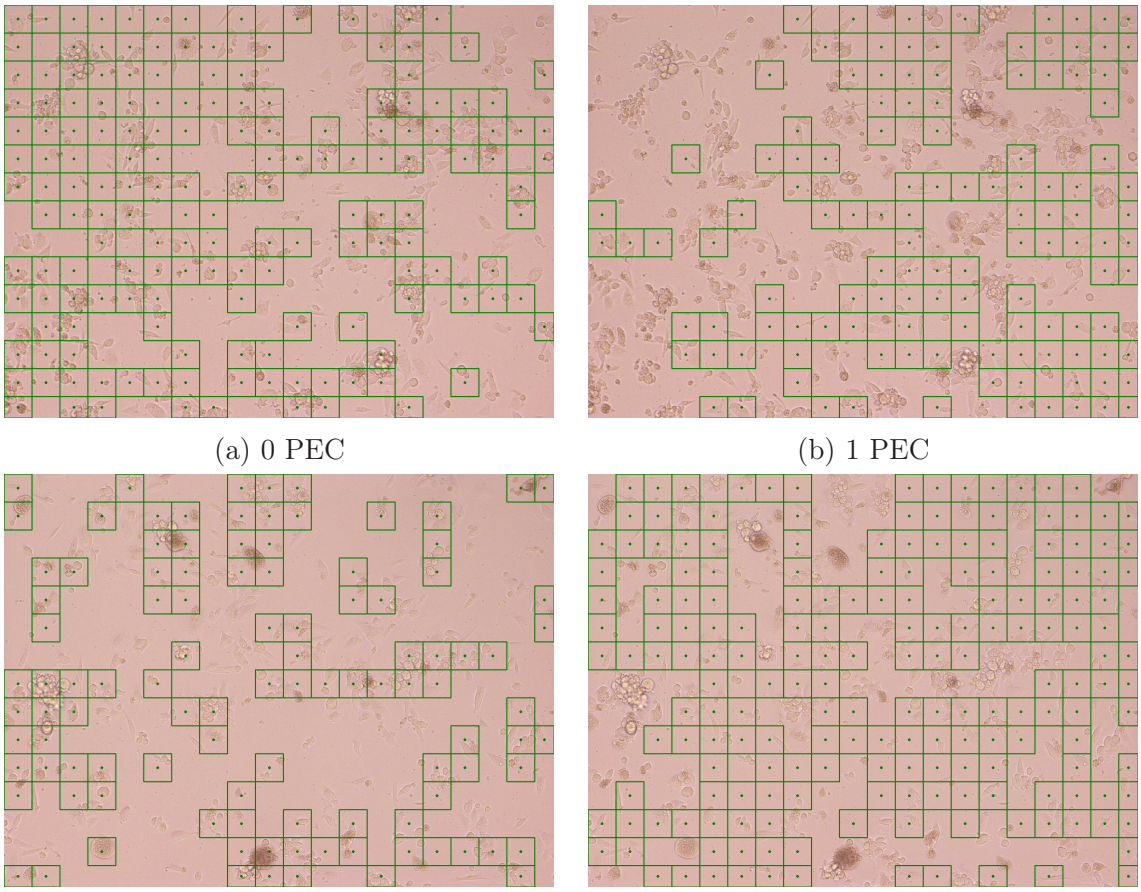

(a) 0 PEC (b) 1 PEC

(c) 0 PEC (d) 1 PEC

Figure 2.15: Image regions that do not have a phase effect characteristic in their TEN focus curves are drawn on the images on the left-hand side. Image regions with exactly one phase effect characteristic are shown in the same images on the right-hand side

all cell details. Blobs with high contrast (Figure 2.16a, Figure 2.16e) are responsible for higher statistic-based measures. Wider stacks will also have a PEC for statistic-based measures, because the gained contrast is then removed by the smoothing. The main differences between statistic- and gradient-based measures are the positions of the maxima. The focus curves of statistic-based focus measures for our data have a global minimum at the optical focus position because the acquired $z$-distance is small enough. Due to the limitation of our data, statistic-based PECs could not be investigated. This is part of future research.

The results in Table 2.5 show that the gradient-based local PEC minimum is very close to the global minimum of the NVAR curve at a distance which is less than the step size in the $z$-direction (5 µm). This distance indicates that the $z$-position of the local minimum of a PEC in a gradient-based curve is the optical focus position. Therefore, the PEC minimum of focus measures should be used to find the optical focus position for phase objects instead of a global maximum.

As shown in Table 2.5, the maximum of a gradient-based curve has an average distance of about 10 µm from the minimum of the corresponding NVAR curve. This

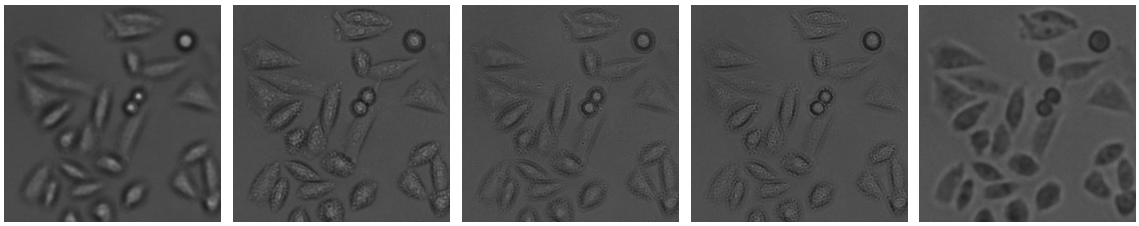

(a) negative (b) negative (c) at-focus (d) positive (e) positive

Figure 2.16: Homogeneous CHO cells at different focus positions

distance shows the error in localizing the optical focus that is introduced when interpreting the gradient-based curve in the typical way that is appropriate for amplitude objects.

In applications such as automatic bright-field cell image analysis [Mual 14a] or in phase retrieval [Alle 01], it is important to find the optical focus position. However, in the presence of the phase effect we show that the typical use of focus measures will fail. For these applications, the PEC minimum of focus measures should be used.

Other approaches use images with manually selected defocus distances in one or both directions of the optical focus. We suggest using the two PEC maxima of focus curves in order to automatically select appropriate $z$-positions. Whether gradient- or statistic-based measures should be used depends on the application. For cell detection [Beca 11, Ali 11a, Mual 13] the maxima of a statistic-based measure seem promising. In images of an automated microscope the cell details are most important for analysis. Therefore, the maxima of gradient-based measures seem promising. This focus position could also be used for the initialization of the segmentation in [Ali 11a].

Criteria for ranking focus measures are used in many focus papers (e.g. [Sant 97, Sun 04, Fire 91]). They are not applicable for focus curves of phase objects and should be adjusted for this case. For example, the number of false maxima should be changed to the number of false extrema (excluding the PEC extrema). This topic is out of the scope of this work and can be investigated in future research.

The focus estimated by four bioprocess engineering experts diverges considerably from the optical focus. The average absolute distance from the minimum of NVAR is $19.20 \pm 12.39$ µm and no expert chose an image at the minimum NVAR position. Expert users seem to interpret focus as the image plane were cells are optimally visible. As mentioned above, many cells are invisible at the optical focus and they become visible only with the increased contrast resulting from defocusing. The $z$-position of the optical focus and the $z$-position of an image that expert users prefer to see are different for phase objects.

Our results further showed that the gradient-based focus curves of all inhomogeneous stacks have typical focus curves with one distinctive maximum. Nevertheless, in some cases, a minor similarity with the non-typical curves was observed. In order to understand these curves, we investigated the images in more detail. According to Equation 2.17, a focus curve of the whole image can be seen as the sum of the focus curves of the image patches.

In the homogeneous stacks, the majority of the patch curves show exactly one PEC due to the homogeneity. They tend to overlap constructively and produce focus curves

with one PEC. We noticed that the patches with more than one PEC are mostly background patches and can be regarded as noise. In fact, in our homogeneous image stacks, background patches are much more frequent compared to the inhomogeneous image stacks because of two reasons: First, the cells are sparsely distributed in the homogeneous stacks (see 2.4.4). Second, in the inhomogeneous stacks, cellular debris is in all image parts due to the longer cultivation time.

In the inhomogeneous stacks, the majority of the patch curves are typical and therefore do not have a PEC whereas about one-fourth has exactly one PEC. As shown in Table 2.7, the $z$-position for $FGRAD_{0PEC,max}$ is shifted in the positive $z$-direction regarding $FGRAD_{1PEC,min}$. $FGRAD_{0PEC,max}$ and $FGRAD_{1PEC,max}$ coincide approximately. Consequently, depending on the overlapping pattern, combining the curves of all patches tends to produce focus curves which look similar to the focus curves for amplitude objects. The maximum of these curves is therefore related to a $z$-position where the contrast of the homogeneous cells is enhanced due to positive defocusing and the agglomerations are approximately focused.

The minimum remains in the statistic-based focus curves for inhomogeneous stacks because the distance between the PEC maxima is much higher compared to gradient-based curves. Therefore, the minimum is not eliminated by overlapping curves from different patches.

For gradient-based measures, 0PEC patches contain cells with different object characteristics than 1PEC patches as Figure 2.15 shows for inhomogeneous cells. Indeed, 1PEC patches tend to show mostly phase objects such as single cells, and 0PEC patches tend to show mostly amplitude objects such as cell agglomerations. This knowledge can be used to differentiate between phase objects and amplitude objects by analysing focus curves of image patches. It would, therefore, be possible to detect automatically different $z$-positions for their different optical foci. A combination of our results with approaches that use only detected image regions for focusing such as [Hamm 10] seems promising.

## 2.5 Automatic Focus

We investigated phase objects, focus measures and focus positions for bright field microscopes in the previous section. Unfortunately, most results were not applicable to the COSIR systems due to partially unpredictable behaviour of the focusing parts of the systems. The primary goal of the algorithm presented in this section is to work in a stable manner. We used the TEN focus measure because it turned out to be stable compared to the other focus measures. This decision was made based on the qualitative analysis of resulting focus curves. A PEC maximum was used as focus position instead of the PEC minimum because the resulting image is appropriate for analysis by an expert. The PEC maximum is also better suited for cell detection (see Section 5.1) than the image at the PEC minimum.

Algorithm 2 shows the procedure for automatically adapting the focus position. The calibrated focus position $f_0$ (see Section 2.2) is used as input $f_{\text{start}}$ when the procedure is executed the first time. For further adaptions, the focus position determined in the previous adaption is used. In the initialization phase of Algorithm 2, the focus of the hardware is changed to $f_{\text{start}}$ and an image $I_{\text{start}}$ is acquired. The initial max-

**Algorithm 2** Automatic Focus Adaption

```
1: procedure AutoAdaptFocus(f_start, F_thresh)
2:     I_start ← ChangeFocusAndTakeImage(f_start)
3:     F_max ← GetTenenGrad(I_start)
4:     f_max ← f_start
5:     F_max, f_max, MAX_Found ← ScanNeighbors(f_max, F_max, F_thresh)
6:     if !MAX_Found then
7:         focusCurve ← CoarseScanForward
8:         F_max, f_max ← GetFocusForMaximum(focusCurve)
9:         CoarseScanBackward(f_max)
10:        F_max, f_max, MAX_Found ← ScanNeighbors(f_max, F_max, F_thresh)
11:    end if
12:    return f_max
13: end procedure
```

imum focus value $F_{\max}$ is calculated from $I_{\text{start}}$ and $f_{\max}$ is set to the corresponding focus position $f_{\text{start}}$.
In the adjustment phase, two variations are used:

- Fine scan of the neighbourhood using the step size $f_{\text{step,fine}}$.
- Coarse scan of the whole focus range using the step size $f_{\text{step,coarse}}$.

The step sizes can be configured. For the COSIR systems we used approximately 1 µm for $f_{\text{step,fine}}$ and approximately 20 µm for $f_{\text{step,coarse}}$. The adaption procedure is called each time when an image is acquired. A fine scan in the neighbourhood of the initial focus position $f_{\text{start}}$ is done first. If a maximum is found, the algorithm ends and the focus position of this maximum is applied to the hardware. If no maximum is found, a course scan is done to find a better approximation of the focus position than $f_{\text{start}}$. The approximation is stored as $f_{\max}$. After the course scan is done, the maximum of the acquired focus curve ($F_{\max}$) is determined. The focus position of the system is then changed to this position and a fine scan is done in the neighbourhood.

Algorithm 3 shows the fine scan in detail. First, $f_{\text{step,fine}}$ and $f_{\text{range,fine}}$ are read from the configuration file. The maximal range scanned in each direction is $f_{\text{range,fine}}$. For the COSIR systems, 60 µm was used as $f_{\text{range,fine}}$. Second, the left side is scanned for a maximum. If no maximum is found, the right side is scanned too. Focus value and focus position of the maximum ($F_{\max}, f_{\max}$) and a Boolean value indicating if a maximum was found are returned.

Starting with Line 10 in Algorithm 3, the fine scan in one direction is shown in detail. The function contains a loop that starts at the focus position $f_{\text{in}}$. Three reasons can stop the loop:

1. The shift distance reaches $f_{\text{range}}$.
2. There is almost no difference in the focus value of ten images ($|F_{\max} - F_{\text{loop}}| < F_{\text{thresh}} \cdot F_{\max}$). Either the system is completely out of focus or the lens does not react. $F_{\text{thresh}}$ was experimentally set to 0.02.

**Algorithm 3** Focus Fine Scan

```
1: function ScanNeighbors(f_in, F_in, F_thresh)
2:     f_step ← ReadFineFocusStepFromConfig()
3:     f_range ← ReadFineFocusRangeFromConfig()
4:     F_max, f_max, MAX_Found ← ScanFineLeft(f_in, F_in, f_step, f_range, F_thresh)
5:     if !MAX_Found then
6:         F_max, f_max, MAX_Found ← ScanFineRight(f_in, F_in, f_step, f_range, F_thresh)
7:     end if
8:     return F_max, f_max, MAX_Found
9: end function
10: function ScanFineLeft(f_in, F_in, f_step, f_range, F_thresh)
11:     F_max ← F_in
12:     f_max ← f_in
13:     MAX_Found ← false
14:     NoDiff ← 0
15:     AfterMax ← 0
16:     f_loop ← f_in − f_step
17:     while f_loop > f_in − f_range and AfterMax < 2 and NoDiff < 10 do
18:         I_loop ← ChangeFocusAndTakeImage(f_loop)
19:         F_loop ← GetTenenGrad(I_loop)
20:         if |F_max − F_loop| < F_thresh · F_max then
21:             NoDiff + +
22:         else if F_loop > F_max then
23:             F_max ← F_loop
24:             f_max ← f_loop
25:             MAX_Found ← true
26:         else
27:             AfterMax + +
28:         end if
29:         f_loop ← f_loop − f_step
30:     end while
31:     return F_max, f_max, MAX_Found
32: end function
33: function ScanFineRight(f_in, F_in, f_step, f_range, F_thresh)
34:     ...
35:     f_loop ← f_in + f_step
36:     while f_loop < f_in + f_range and AfterMax < 2 and NoDiff < 10 do
37:         ...
38:         f_loop ← f_loop + f_step
39:     end while
40:     ...
41: end function
```

3. A maximum of the focus values was found and additionally two consecutive images have different and smaller focus values.

The scan function in the other direction works exactly in the same way. The only difference is that the focus shift is added to the focus position $f_{\text{in}}$ instead of being subtracted.

**Algorithm 4** Focus Coarse Scan

```
1: function CoarseScanForward
2:     f_step ← ReadCoarseFocusStepFromConfig()
3:     f_start ← ReadCoarseSweepStartFocusFromConfig()
4:     f_end ← ReadCoarseSweepEndFocusFromConfig()
5:     focusCurve ← new FocusCurve()

6:     for f_loop ← f_start; f_loop <= f_end; f_loop = f_loop + f_step do
7:         I_loop ← ChangeFocusAndTakeImage(f_loop)
8:         F_loop ← GetTenenGrad(I_loop)
9:         focusCurve.Add(f_loop, F_loop)
10:    end for
11:    return focusCurve
12: end function

13: function CoarseScanBackward(f_max)
14:    f_step ← ReadCoarseFocusStepFromConfig()
15:    for f_loop ← f_current − f_step; f_loop >= f_max; f_loop = f_loop − f_step do
16:        ChangeFocusTo(f_loop)
17:    end for
18: end function
```

The coarse scan procedures are shown in Algorithm 3. The forward scan procedure scans the whole focus range from $f_{\text{start}}$ to $f_{\text{end}}$ with a configurable step size. When the algorithm was applied to the COSIR systems, a range of approximately 300 µm was scanned with a step size of approximately 20 µm. A focus curve containing each scanned focus position and the focus value is generated and returned. After determining the maximum of the focus curve, the focus position of the COSIR system is not directly changed to this position. The system changes the focus position step-wise back to this position. This is done because the lens showed an effect called hysteresis. The lens behaves differently if the focus position is changed step-wise compared to the case when it is changed at once. The step-wise approach tended to be more accurate for getting to the position with maximum focus value.

# Chapter 3

# Hardware Development and Analysis

In the research project COSIR the development of the hardware and the development of image processing algorithms were done in parallel. This turned out to be an advantage for the hardware development, because image processing algorithms (especially focusing algorithms) could be used to investigate an actual hardware setup and the evaluations were used to identify hardware or firmware issues that needed to be solved. This chapter contains the experiments and investigations that helped to understand and improve the COSIR systems. In Section 3.1 experiments regarding the light path of COSIR systems are described. Different investigations concerning the lens are summarized in Section 3.2. In Section 3.3 an effect is investigated that was related to the light source. Finally, in Section 3.4 the influence of objects in microtiter plates to focusing is analysed.

Because the exact hardware parts of the COSIR prototype systems are confidential, some sections contain just basic hardware information that are necessary to understand the experiments and the conclusions. A more accurate hardware description could not be given.

## 3.1 Light Path

The hardware setup and the light path of the COSIR systems is different from a standard bright field microscope (as described in Section 1.3.1). It is shown in Figure 3.1. One main difference is the position of the light source. The light source and the imaging sensor are at the same side of the object for the COSIR systems. A beam splitter is used to turn the light from the light source to the object and the beam splitter also let the light pass on the way back from the object to the imaging sensor. At the beginning of the research project it was not clear where the light that reaches the imaging sensor comes from: Is it reflected at the object or at the material above the well? To find that out a series of experiments regarding the material above the well were done.

The material is very important for the amount of light that is reflected at that position. When light travels from one material to the other, a part of the light is reflected and another part is refracted and passing through the material. The amount of light that passes through the medium depends on the refractive indexes of both materials.

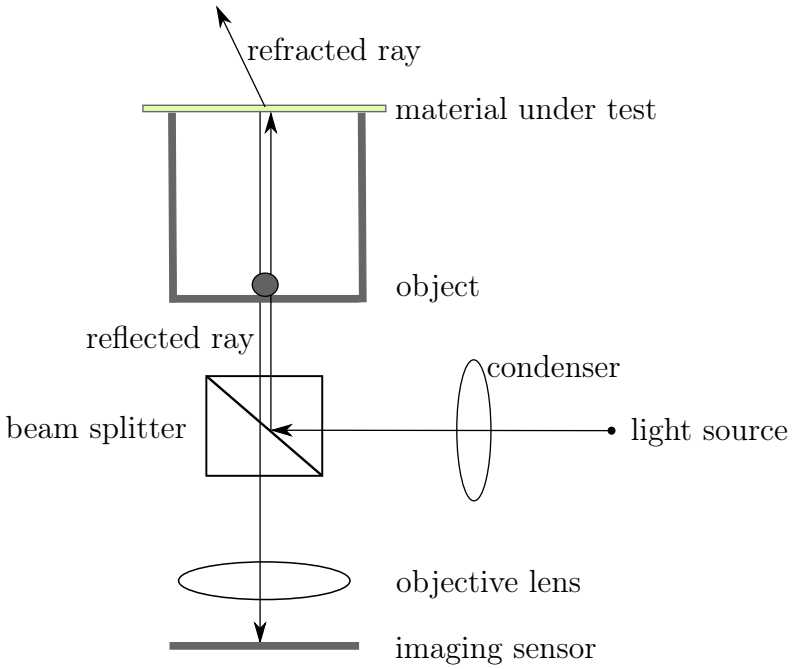


Figure 3.1: Setup for testing the light path of COSIR systems

### 3.1.1 Experiments

For all experiments in this section CHO was used as cell line. To determine the influence of the light reflected from the material under test (MUT) (see Figure 3.1) two experiments were done.
Two materials were used as MUT in the different COSIR systems:

- a mirror
- a semitransparent material

In the experiments the standard MUT was replaced to estimate the influence of the reflected light in the resulting image. It was replaced by:

- no material (air) or
- black material (absorption of the light).

In the first experiment the mirror was used as MUT. Then the illuminance and the exposure time were manually tuned to get a suitable image. The mirror was then removed and an image was taken without changing the illumination parameters. The results of this experiment are shown in Figure 3.2.

In the second experiment the semitransparent material was used as MUT. Then the illuminance and the exposure time were manually tuned to get a suitable image. The mirror was removed then and an image was taken without changing the illumination parameters. A second image was acquired. Then a black material was put above the well and a third image was acquired. The results of this experiment are shown in Figure 3.3.

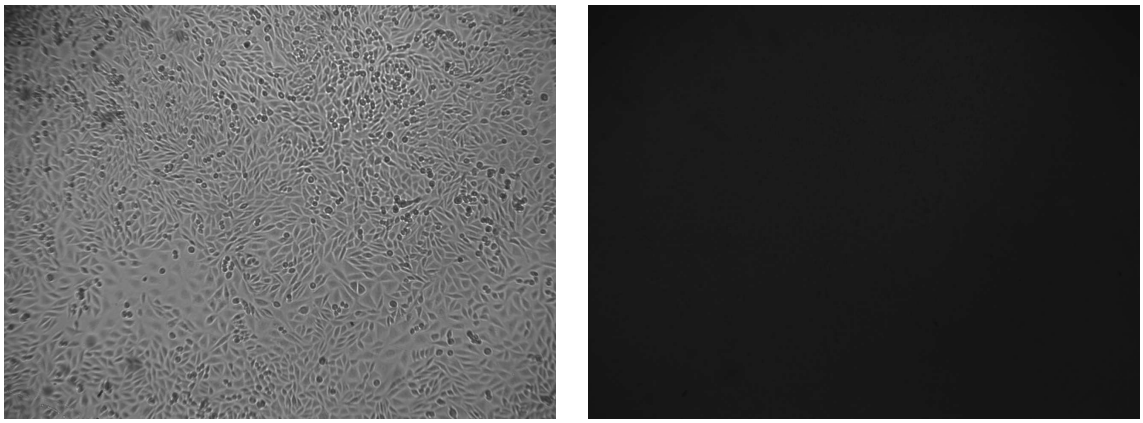

(a) MUT = mirror (b) MUT = air (no material)

Figure 3.2: Illumination is adapted to a mirror and an image is acquired (3.2a). The same illumination settings are used after removing the mirror (3.2b)

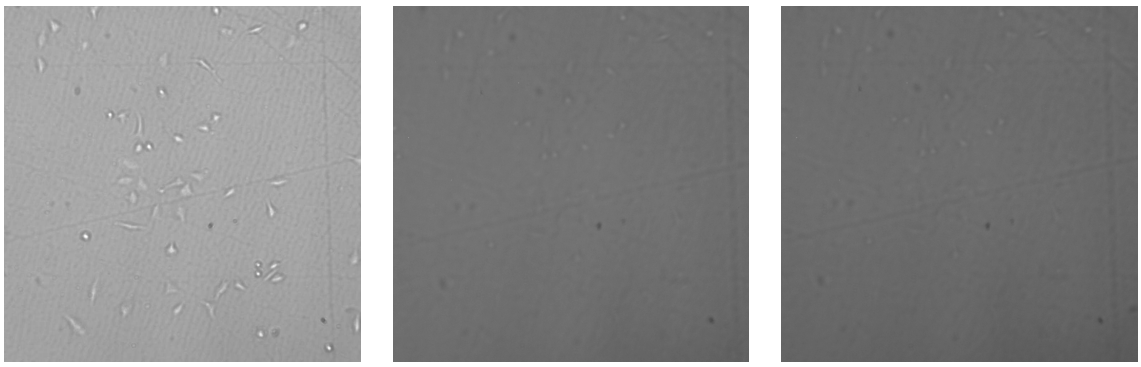

(a) MUT = semitransparent material (b) MUT = air (no material) (c) MUT = black material

Figure 3.3: Illumination is adapted to a semitransparent material and an image is acquired (3.3a). The same illumination settings are used after removing the mirror (3.3b) and with a black cover material (3.3c)

### 3.1.2 Conclusion

In both experiments the majority of the information in the image is only visible in the first image (see Figure 3.2a and 3.3a). If the material is removed (Figure 3.2b and 3.3b) or replaced by a black material (Figure 3.3c), the cell information is not or nearly not visible. The conclusion of the experiments was that the COSIR setup is similar to the setup of a bright field microscope, because the majority of the light containing cell information that reaches the imaging sensor is transmitted through the object. The material above the well can be regarded as light source to simplify the COSIR setup.

The main benefit of these experiments and conclusion was, that we could develop algorithms for the COSIR systems using standard bright field images or apply algorithms already used for them.

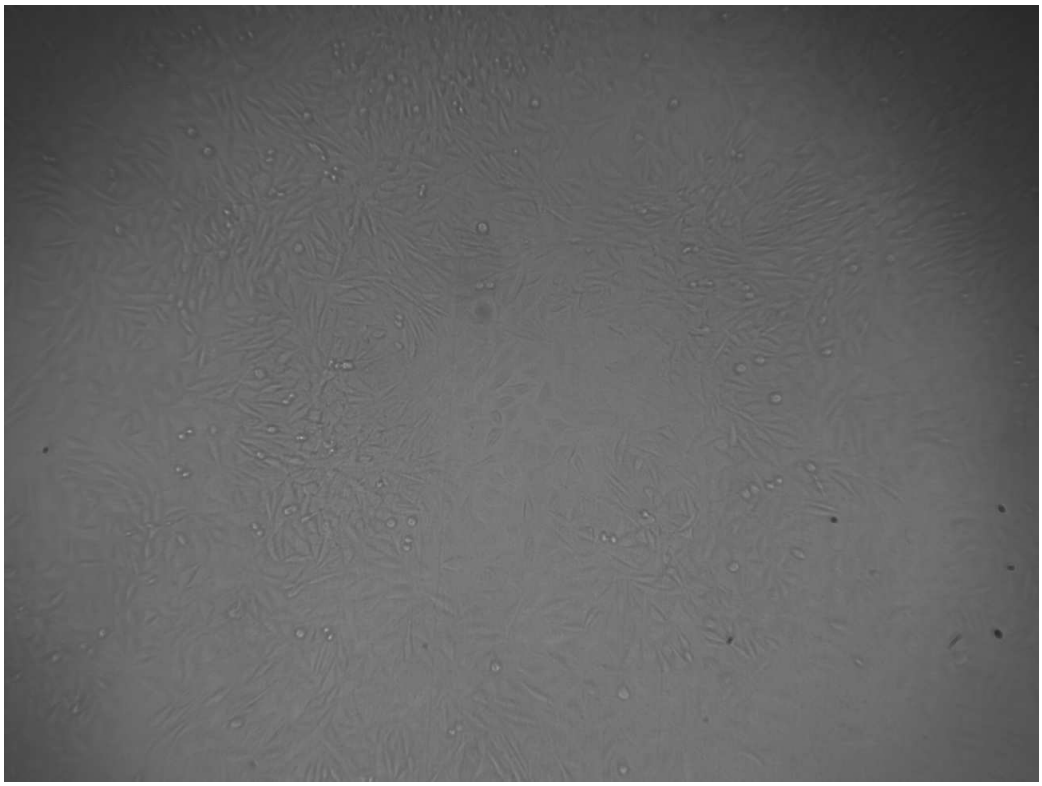

Figure 3.4: Image of CHO cells with differently focused parts

## 3.2 Lens

The lens is responsible for focusing the COSIR system. A different focus position can be set by either changing the position of the lens or by changing the properties of the lens. In the COSIR systems both ways were used, but the exact details of the lenses that were used for the experiments are confidential. The following sections describe how focus algorithms were used to analyse and solve different issues regarding the lens.

### 3.2.1 Focus Lateral Irregularity

If a cell imaging system is focused, one focus position is determined where the whole image is (or should be) at focus. As described in Section 2.4 phase objects such as CHO cells have a different appearance depending on the focus position. They are almost invisible at the optical focus position, they get black when they are positively defocused and white if they are negatively defocused. From one stage of the prototype systems we got images from CHO cells as depicted in Figure 3.4. This image contains all three kinds of appearance. The effect was investigated using focus curves.

#### Experiments

A focus stack with 18 images was acquired with the COSIR prototype system. Each image has a resolution of $2592px \times 1944px$. The distance between two images was

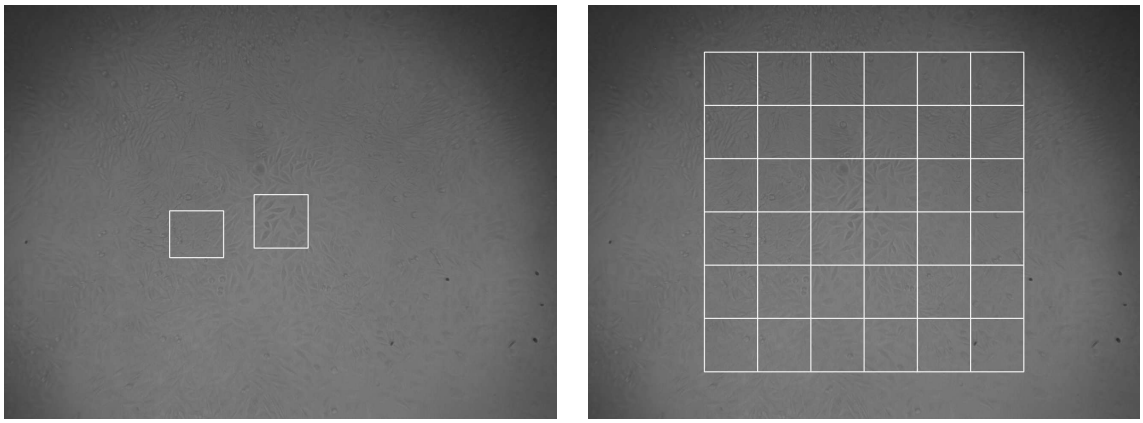

(a) Two areas (b) Thirty-six areas

Figure 3.5: Two manually selected areas (Figure 3.2a) and a grid of six by six square areas (Figure 3.2b) are evaluated to quantify the focus shift of image parts

approximately 5 µm. To investigate the effect inside the image two experiments were done.

First, two areas were selected manually where the focus position seemed to be most different. These regions are drawn on the image in Figure 3.5a. Second, a grid of $6 \times 6$ image areas was selected automatically around the image centre. Each image area has a resolution of $250px \times 250px$.

As focus measure, TEN was used. In each area the focus position was determined as the PEC minimum according to Section 2.4.

For the two manually selected areas the focus of the left area was detected at image number 8 and the focus position of the right area at image number 10. Therefore, the $z$-distance of the focus position of these two areas is approximately 10 µm.

Focus positions of the 36 image regions are shown in Table 3.1. This experiment shows that there is an apparent deviation of the optical focus position between the upper-left part and the middle of the acquired images. This deviation is approximately 10 µm on the $z$-axis.

| | | | | | |
|---|---|---|---|---|---|
| 7 | 8 | 8 | 8 | 8 | 8 |
| 7 | 8 | 8 | 8 | 8 | 8 |
| 8 | 8 | 9 | 9 | 8 | 8 |
| 8 | 8 | 8 | 8 | 8 | 8 |
| 8 | 8 | 8 | 8 | 8 | 8 |
| 8 | 8 | 8 | 8 | 8 | 8 |

Table 3.1: Image numbers of the focus position for all 36 image areas

### Conclusion

The evaluations using focus curves showed that it is not possible to get one image at focus with this specific version of the hardware. Even in the inner square region of the image that is approximately $1 \times 1$ mm$^2$, the $z$-distance of the focus position

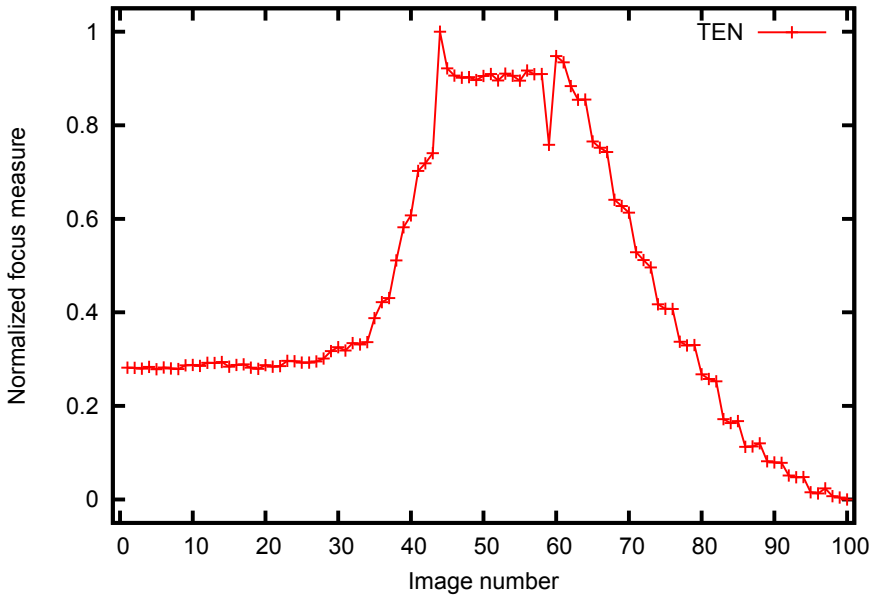


Figure 3.6: Focus curve of an image stack taken with a prototype system that shows a significant plateau

differs by approximately 10 µm. After these results were presented, the hardware was corrected to remove the effect.

### 3.2.2 Quantization Step Size

At the very early development stages of the COSIR systems no algorithm for automatic focus was used. Focus measures were implemented but not used for focusing. Z-stacks in a given range were acquired to test the applicability of the focus measures. This section describes one effect that appeared and the conclusion drawn.

#### Experiment

A focus stack with 100 images was acquired with the COSIR prototype system. The $z$-distance between two images was limited by the firmware of the prototype system. Therefore, the smallest $z$-distance between two images was approximately $1 - 2$ µm. This $z$-distance was used to acquire the image stack. In each image the $1 \times 1$ mm$^2$ area (see Section 2.2) was detected and cropped. Each resulting image has a resolution of $1400px \times 1400px$. The TEN focus measure was applied to all images and the resulting focus curve is shown in Figure 3.6. In the focus curve a plateau is clearly visible where a PEC is expected. Indeed, the focus value of image 45 and the focus value of image 58 are almost the same. From image 58 to image 59 and from image 59 to image 60 the focus value changes significantly. These images are shown in Figure 3.7.

#### Conclusion

After discussing the focus curves with the hardware experts they found out that the quantization step size used in the firmware to change the focus position had to

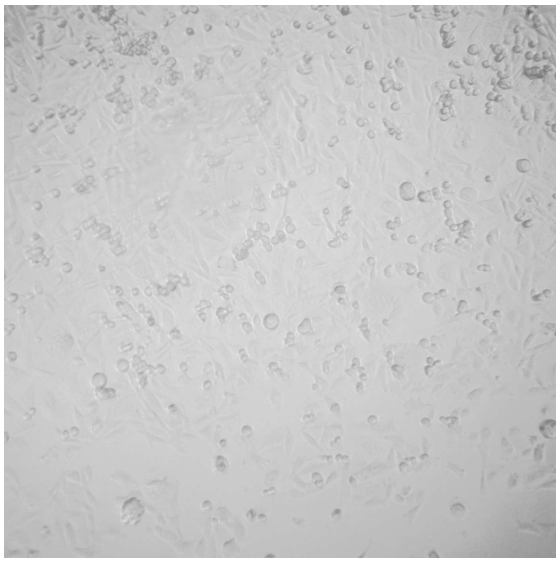

(a) Image 45

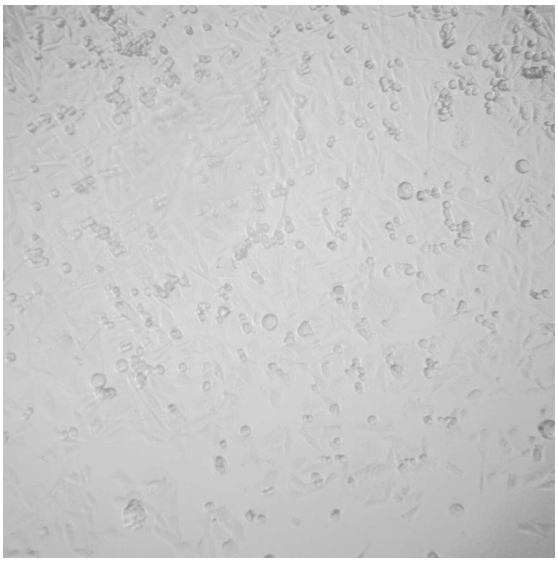

(b) Image 58

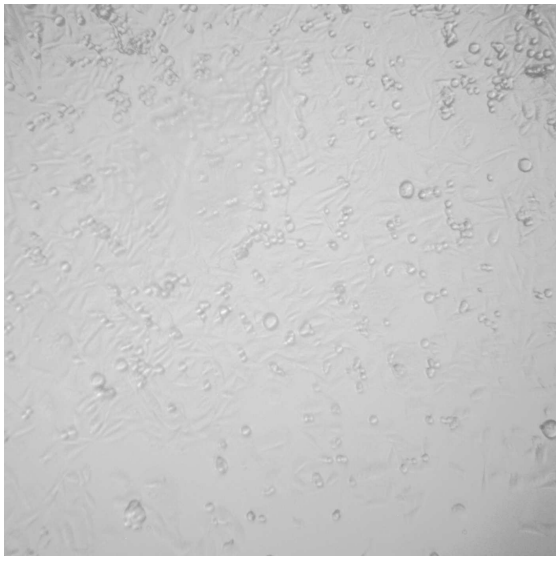

(c) Image 59

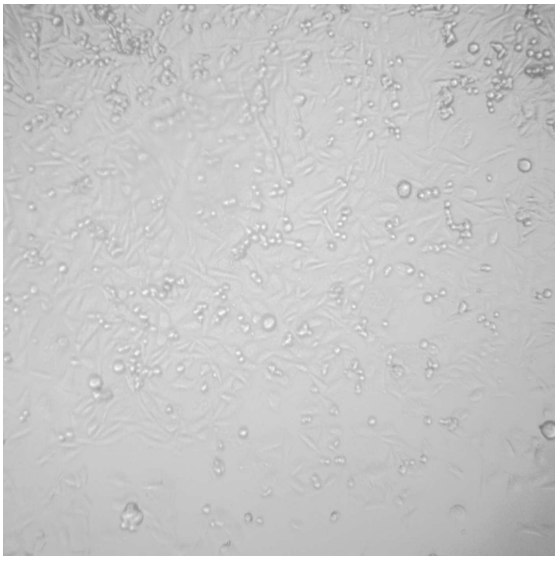

(d) Image 60

Figure 3.7: Images at the beginning and the end of the plateau in the focus curve

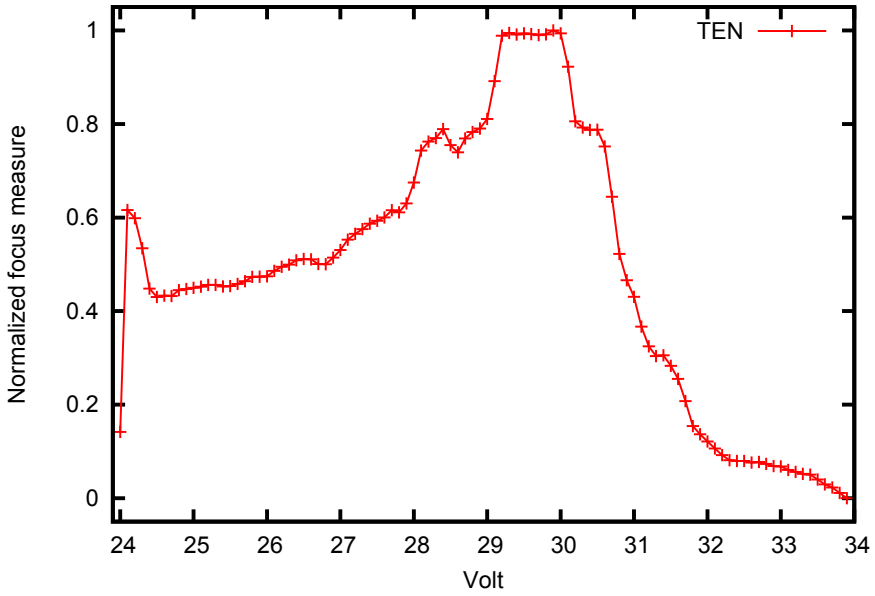


Figure 3.8: Focus curve where the focus value between image 1 and image 2 is very different

be corrected. As a consequence the firmware was updated and this problem was removed.

### 3.2.3 Timing

Another example how the interpretation of focus curves can help to detect and solve a problem of the imaging system is presented in this subsection.

#### Experiment

A focus stack with 100 images was acquired with the COSIR prototype system. In each image the $1 \times 1\ \text{mm}^2$ area (see Section 2.2) was detected and cropped. Each resulting image has a resolution of $1400px \times 1400px$. The $z$-distance between two images was approximately 1 µm. The TEN focus measure was applied to all images and the resulting focus curve is shown in Figure 3.8.

The difference of the focus value of image 1 and image 2 is approximately 0.5. The images look very different.

#### Conclusion

In order to acquire a $z$-stack, two commands of the firmware are executed in a loop:

- change the $z$-position
- acquire an image

After discussing the focus curves with all project partners we found out that we need to wait between these two commands. Before this experiment started, the focus of the imaging system was at the other end of the focus range. The first image was taken,

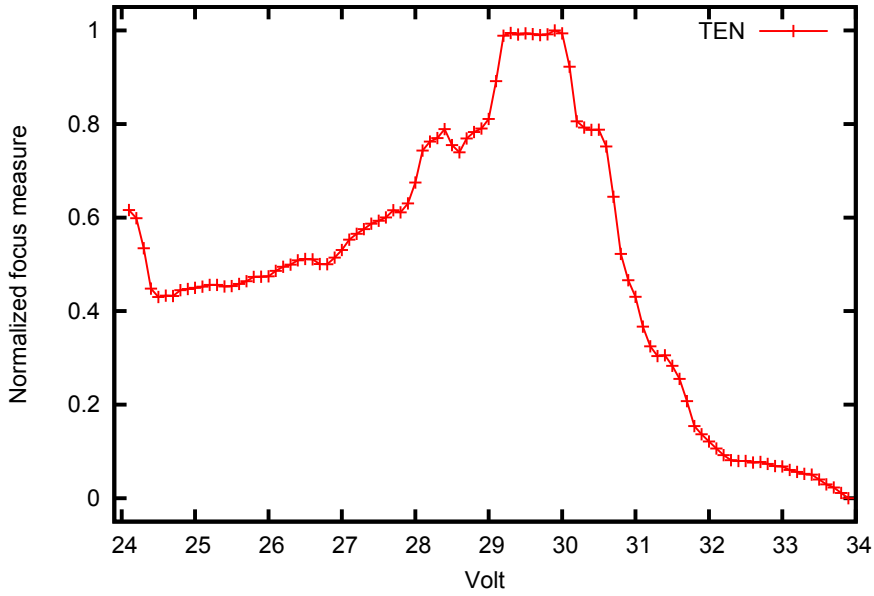


Figure 3.9: First experiment regarding the response of the lens. The image at-focus is at 24.5. The right maximum at 30.

before the adjustment of the focus position was completely finished. The image was acquired at a focus position between the focus position used before and the focus position that was intended. After knowing the reason for this effect the acquisition protocol was adapted:

- change the $z$-position
- wait until the intended focus position is reached
- acquire an image

### 3.2.4 Response

Different lenses and ways of focusing were used during the development of the COSIR system. In one of the used lens types, changing the focus position is achieved by changing the voltage level. The response of this lens type regarding voltage changes is investigated in this section.

#### Experiment

A $z$-stack of adherent CHO cells was acquired with two different hardware setups. Both hardware setups included the same lens type that is described above. A voltage of 24 V was used to acquire the first image. A step size of 0.1 V was used to acquire the next image. For the first experiment 100 images were acquired and for the second experiment 110. In each image the $1 \times 1\ \mathrm{mm}^2$ area (see Section 2.2) was detected and cropped. Each resulting image has a resolution of $1400px \times 1400px$. The TEN focus measure was applied to all images and the resulting focus curves are shown in Figure 3.9 and Figure 3.10.

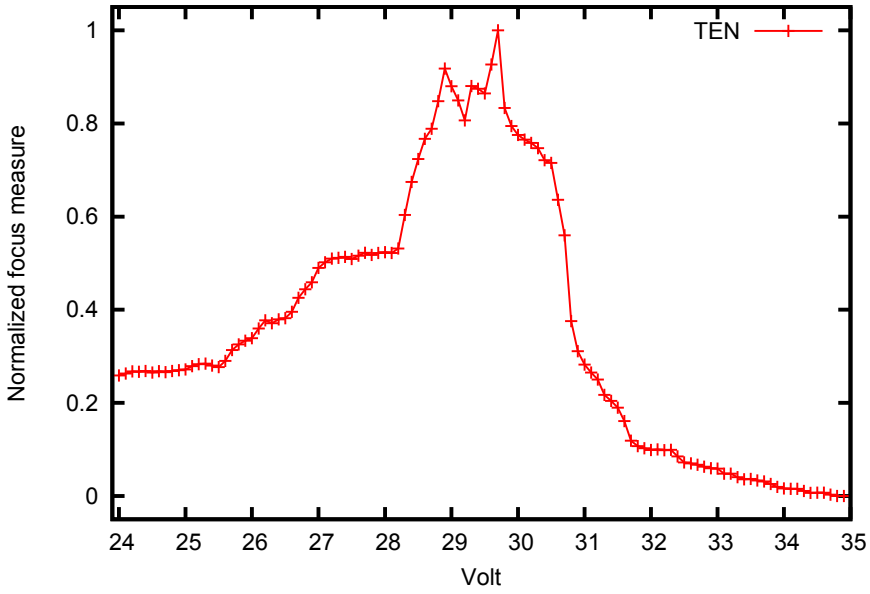


Figure 3.10: Second experiment regarding the response of the lens. The image at-focus is at 29.2. The right maximum at 29.7.

The first experiment (Figure 3.9) equals the experiment from Section 3.2.3 (Figure 3.8). Only the first point is removed because the timing problem described in the section above was responsible for a wrongly focused image and therefore this focus value is not usable.

We know from Section 2.4 that the focus curves of adherent cells should have a PEC in the TEN focus curve. The cells in images from the two maxima of the PEC also have a different appearance. Positively defocused cells are dominated by black and negatively defocused cells are mostly white. The cells nearly disappear when the system is at-focus. Based on this knowledge, the acquired images and the calculated focus curves were evaluated to determine the focus position manually.

The at-focus image in the first experiment was acquired with 24.5 V applied to the lens. Almost all images of this stack are negatively defocused. The at-focus image in the second experiment was acquired with 29.2 V applied to the lens.

### Conclusion

The behaviour of the investigated lenses was discussed with our hardware partner. It turned out that for a voltage smaller than 26 V, voltage changes only slightly change the focus position. The higher the voltage, the higher is the focus position change resulting from the same step. Two different lenses also showed high differences in their behaviour regarding the voltage range $24 - 30$ V.

The experiments and investigations presented in this section showed that for this lens type, the position regarding the object is very important. As a consequence, the position of the lens was adapted in further hardware setups containing this lens type. The lens was moved towards the object and focusing as described in Section 2.5 became possible.

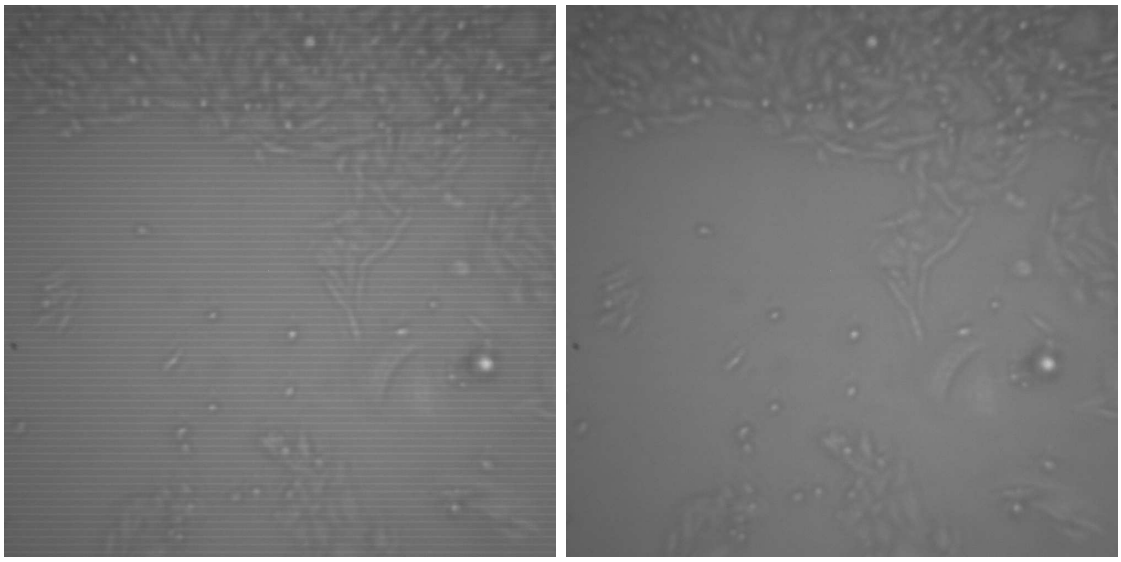

(a) Horizontal lines (b) Removed horizontal lines

Figure 3.11: Horizontal lines visible in a COSIR image

## 3.3 Light Source

Horizontal lines appeared in images of one specific COSIR system (see Figure 3.11a). If only few cells were in the image area, the horizontal lines were the dominant edges in the image and therefore automatic focusing did not work correctly.

### 3.3.1 Method

Since this artefact is periodic, it can be tackled in the Fourier domain. The repetitive pattern in Figure 3.11a manifests itself in the Fourier domain as maxima of $|\mathcal{F}(u, v)|$ at $nv_0$, where $\mathcal{F}(u, v)$ is the Fourier transform of $I(x, y)$, $n = \pm 1, \pm 2, \pm 3, \ldots$, and $v_0$ is the fundamental frequency of the repetitive pattern. Therefore, in order to remove this artefact, we set $\mathcal{F}$ at frequencies which satisfy $u = 0$ and $|v| \geq v_0$ to zero. The result is shown in Figure 3.11b.

### 3.3.2 Discussion

Periodic patterns in images such as the horizontal lines can be easily removed in the Fourier domain. However, the reason for such image artefacts should be removed. The brightness generated by the light sources in our systems is a result of light pulses. It depends on the pulse width and frequency. The horizontal lines appeared because the frequency was very small. After increasing the frequency, the horizontal lines disappeared and the algorithm (see Section 3.3.1) could be removed from the image processing pipeline.

(a) Hairs (b) Scratches

Figure 3.12: Objects visible in COSIR images

## 3.4 Microtiter Plate

### 3.4.1 Experiment

The algorithm for automatic focusing (see Section 2.5) was used to acquire images with COSIR systems. The resulting images were sometimes not at-focus and showed objects like hairs (see Figure 3.12a) or scratches (see Figure 3.12b).

### 3.4.2 Conclusion

Microtiter plates are sterile and therefore used only once (see Section 1.2.2) for experiments with real cells. The goal of most experiments we did was to develop and analyse algorithms and hardware and not to draw biological conclusions. Therefore, we used well plates many times. Scratches and hairs are the results of this process. When focusing did not work any more because of these objects we had to exchange the well plates used for testing with new and clean ones.

# Chapter 4

# Preprocessing

One goal of the system COSIR is to allow the user of the system to look at the cell cultures inside the incubator without influencing them. With these images the user can analyse what happens or happened to the cells. In Section 4.1 the whole COSIR pipeline that generates the images presented to the user of the system is presented.

Another benefit of the system COSIR would be if it could produce phase information. Therefore, in Section 4.2, approaches for phase retrieval with bright field images are presented.

## 4.1 COSIR Preprocessing Pipeline

The image processing pipeline of the system COSIR is shown in Figure 4.1. After the calibration is done for a device, the imaged ROI and the start parameters for automatic exposure and automatic focus algorithms are determined (see Section 2.2). When an experiment is started, the illumination is adjusted to the environment (see Section 2.3.2). Images are then iteratively acquired. For each image the illumination conditions of the system are checked and the exposure is adjusted if necessary (see Section 2.3.1). Then the focus is detected automatically (see Section 2.5). The resulting image is transformed in two steps to enhance the visual appearance. First, the circular illumination artefacts are corrected as described in Section 4.1.1. Second, the contrast is enhanced (see Section 4.1.2).

Further preprocessing steps (for example noise removal) were investigated but not taken into account for the COSIR system because they can result in information loss or enhanced artefacts. The main existing problems with the acquired images were illumination artefacts and lack of contrast.

### 4.1.1 Illumination Correction

In the calibration procedure the circular illumination is used to position the imaged ROI. The middle of the ROI is the centre of illumination (see Section 2.2). To correct the remaining illumination artefacts in the imaged area, the illumination field $I_{\text{IlluminationField}}(x, y)$ is computed by convolving the image with the Gaussian kernel(see equation 2.2):

$$I_{\text{IlluminationField}}(x, y) = I(x, y) * G(x, y). \tag{4.1}$$

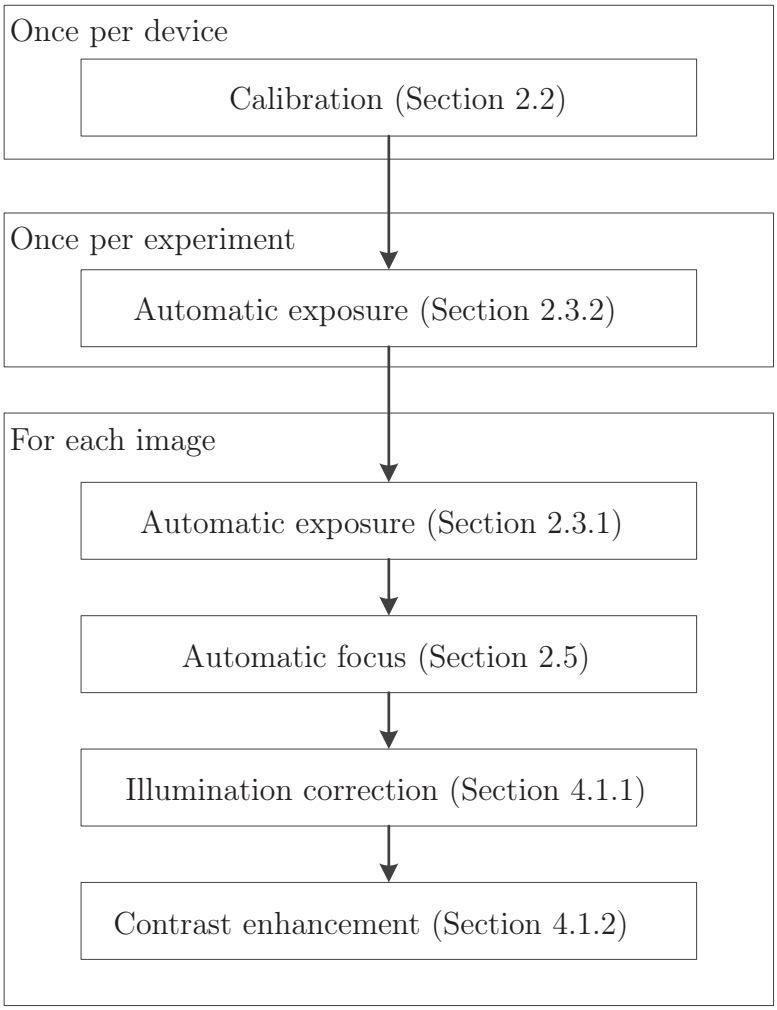


Figure 4.1: Image processing pipeline used to generated COSIR images for the user of the system

The corrected image is generated by subtracting the calculated illumination field from the input image:

$$J(x, y) = I(x, y) - I_{\text{IlluminationField}}(x, y). \tag{4.2}$$

After the subtraction, the range of the resulting image ($J(x, y)$) is changed to the range of the input image ($I(x, y)$).

### 4.1.2 Contrast Enhancement

The resulting images of the COSIR prototypes showed low contrast because just a small range of the possible Gray values was used. To enhance the contrast the intensities of the image are therefore scaled to the whole range of Gray values [0, 255]. To reduce the influence of outliers and noise, the lowest 1% of intensity values are mapped to 0 and the highest 1% are mapped to 255. This simple approach was

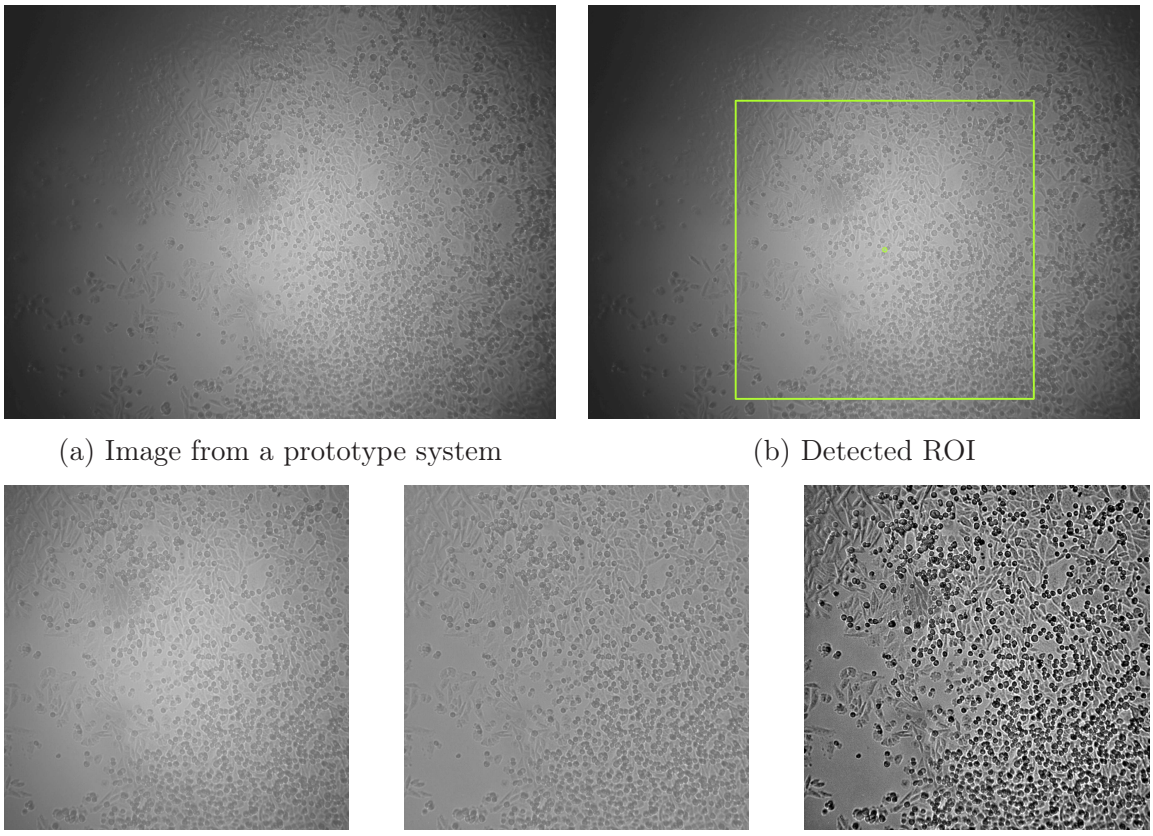

(a) Image from a prototype system (b) Detected ROI

(c) Cropped ROI (d) Corrected illumination (e) Enhanced contrast

Figure 4.2: Results of the COSIR pipeline

chosen because it improves the visual appearance without changing the information content.

### 4.1.3 Results

In Figure 4.2 the results of the last pipeline steps are shown. The micrograph (Figure 4.2a) shows an image of the whole area acquired with a COSIR prototype system. In Figure 4.2b the ROI that was automatically detected in the calibration procedure is drawn on the image. This ROI is cropped (Figure 4.2c) and the illumination field is corrected (Figure 4.2d). For the final image (Figure 4.2e) as last preprocessing step the contrast is enhanced. The final image 4.2e shows a considerable improvement in visual image quality compared to the cropped ROI (Figure 4.2c) due to the two preprocessing steps.

The presented COSIR preprocessing pipeline was used for all development stages of the prototype systems. Therefore, it was completely integrated in the COSIR cell monitoring software which is described later in Section 6.3. The flexible pipeline allowed to use all systems in a similar way and to evaluate their results. This pipeline enables the novel bright field microscopy prototypes to be used to observe cells.

The pipeline was used at a laboratory of our bioprocess engineering partners to observe cell cultures. A large number of images and videos were acquired there and

checked by bioprocess engineers. The above-mentioned algorithms are thus stable and can be safely used in a product.

## 4.2 Phase Retrieval

Although we are able to acquire constantly good images with the novel miniature microscopy systems, the resulting images are still bright field images. The main disadvantage when imaging cells and especially phase objects such as CHO cells with a bright field microscope is the lack of contrast (see Figure 1.4a). The cells and the details in the cells such as the nucleus are almost invisible. One way to enhance the contrast without additional hardware components is to use dyes for staining the cells. For example, as mentioned in Section 1.3.2 the dye trypan blue can be added to the cell culture and it stains the living cells blue. However, cell staining has many disadvantages. High effort is necessary to perform the staining and even worse is that staining influences the cell culture and many stains can even cause the death of cells. Therefore, staining is just applicable in very limited cases.

In practice, a phase contrast microscope (see Section 1.3.1) is normally used instead of a bright field microscope to generate images of the ultra-thin cells. It makes the phase shift of the light waves visible and thereby allows images with significantly higher contrast. As additional hardware components could not be added to the COSIR system, it was not possible to change the type of the microscope. Nevertheless, phase contrast microscopy shows that the phase shift of the light waves contains a lot of information (and thereby contrast).

There are several methods that can be used for retrieving the phase from images of different planes. We investigated three of them. First, an iterative approach is described in Section 4.2.1. Second, a numerical solution to the transport of intensity equation (TIE) is shown in Section 4.2.2. Third, an approximation of the TIE called low-pass monogenic local phase is described in Section 4.2.3. Results of applying these methods are presented afterwards in Section 4.2.4.

### 4.2.1 Iterative Approach

All numerical methods for retrieving the phase shift without specialized hardware use images from different imaging planes in bright field microscopy. As described in Section 2.4 for finding the optical focus using a bright field microscope system, images from different planes are acquired. Therefore, the images that are acquired for focusing can also be used for phase retrieval.

Non-iterative methods use the images from more than one plane to solve an equation. In contrast, iterative methods use the image at one plane, combine it with an approximated (or in case of the first iteration: a random) phase distribution and propagate it to another plane using a propagation function. The resulting phase distribution is used for the next propagation and the amplitude is replaced by the measured one.

The number of planes and the propagation function vary from algorithm to algorithm. The best known algorithm is the Gerchberg-Saxton algorithm [Gerc 72]. Two different image planes are used and the propagation method is the Fourier transform.

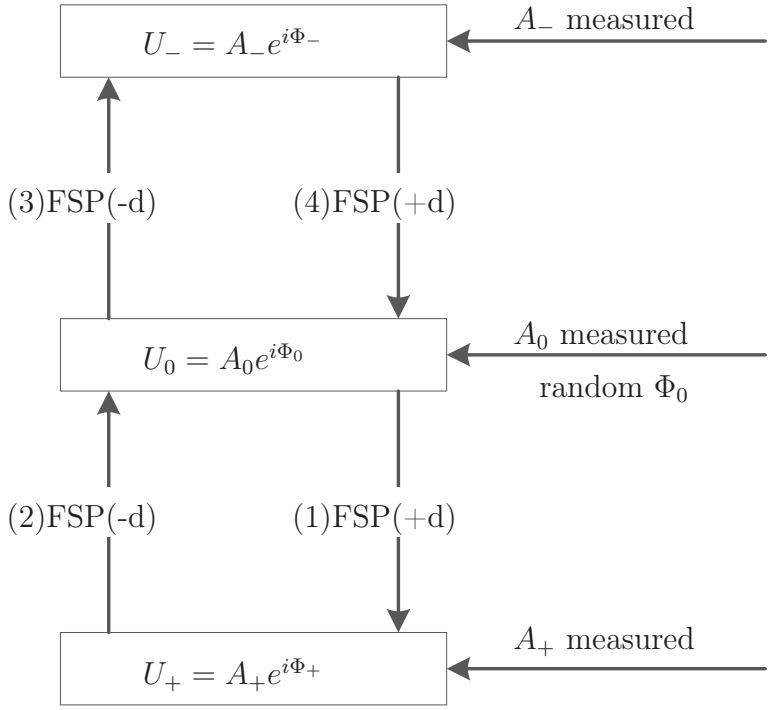


Figure 4.3: First iteration of the iterative phase retrieval algorithm

A short time after the Gerchberg-Saxton algorithm was published, Misell [Mise 73] used the free space propagation (FSP) instead of the Fourier transform as propagation method. Later, the algorithm was also extended to more than two planes. For example, Grossman et al. [Gros 10] used an algorithm with three planes to improve the image quality in the presence of a perturbation medium.

Figure 4.3 shows the first iteration of the algorithm that we [Weig 13] used for iterative phase retrieval. Three images with equal distance $d$ are used. The image at focus $I_0$, a positively defocused image $I_+$ and a negatively defocused image $I_-$. The scalar field at a certain plane can be written as

$$U(x,y) = \sqrt{I(x,y)} e^{i\Phi(x,y)}, \tag{4.3}$$

where $I(x,y)$ is the amplitude or intensity distribution and $\Phi(x,y)$ is the spatial phase distribution [Pope 11]. The first iteration starts at the plane of optical focus. A random phase distribution is used. The scalar field is then propagated to the positively defocused plane (1). The calculated phase image remains and the amplitude image is replaced. The scalar field is then propagated back to the plane of the optical focus (2). It is afterwards also propagated to the negatively defocused plane (3) and back (4).

For further iterations, the scheme in Figure 4.3 stays the same. Just the random phase distribution $\Phi_0$ is not necessary any more, because the previously approximated one is used.

### 4.2.2 Transport of Intensity Equation

The TIE equation [Teag 83] is derived from the Helmholtz equation and can be written as:

$$\frac{2\pi}{\lambda}\frac{\partial}{\partial z}I = -\nabla \cdot I \nabla \phi_{\mathrm{TIE}}, \tag{4.4}$$

where $\lambda$ is the wavelength, $\phi_{\mathrm{TIE}}$ is the physical phase, $\partial z$ is the distance to the optical focus and $I$ is the image at focus.
Paganin and Nugent [Paga 98] found the following algebraic solution to the TIE:

$$\phi_{\mathrm{TIE}} = -\frac{2\pi}{\lambda}\nabla^{-2}\left\{\nabla \cdot \left[\frac{1}{I}\nabla\nabla^{-2}\frac{\partial I}{\partial z}\right]\right\}, \tag{4.5}$$

where $\nabla^{-2}$ is the inverse Laplacian and the intensity $I$ is assumed to be strictly positive.

To compute the inverse Laplacian we used the FFT-based approach from Volkov et al. [Volk 02]

$$\nabla^{-2}s = \mathcal{F}^{-1}\left[\frac{\mathcal{F}[s]}{|\mathbf{q}|^2}\right], \tag{4.6}$$

where $\mathbf{q}$ is the frequency vector. However to use this formula one has to assume that $\mathbf{q} \neq \mathbf{0}$.

### 4.2.3 Low-Pass Monogenic Local Phase

The monogenic signal is the 2D version of the analytic signal. Felsberg and Sommer [Fels 01] introduced it in 2001.
The monogenic signal has the following three output images:

- local energy
$$\tilde{A} = \sqrt{{I_b}^2 + (I_b * h_1)^2 + (I_b * h_2)^2} \tag{4.7}$$
- local phase
$$\tilde{\phi}_{\mathrm{LMLP}} = \arctan\frac{\sqrt{(I_b * h_1)^2 + (I_b * h_2)^2}}{I_b} \tag{4.8}$$
- local orientation
$$\tilde{\theta} = \arctan\frac{I_b * h_2}{I_b * h_1} \tag{4.9}$$

The input image is filtered

$$I_b = I * b, \tag{4.10}$$

where $b$ is the band-pass filter.
The filters $h_1$ and $h_2$ are given as follows:

$$h_l(\mathbf{x}) = \frac{\Gamma((n+1)/2)}{\pi^{(n+1)/2}}\frac{x_l}{\|\mathbf{x}\|^{n+1}}, \quad l = 1, \ldots, n \tag{4.11}$$

where $\Gamma$ is the Gamma function, n is the number of dimensions and $\mathbf{x} = (x_1, \ldots, x_n)$.

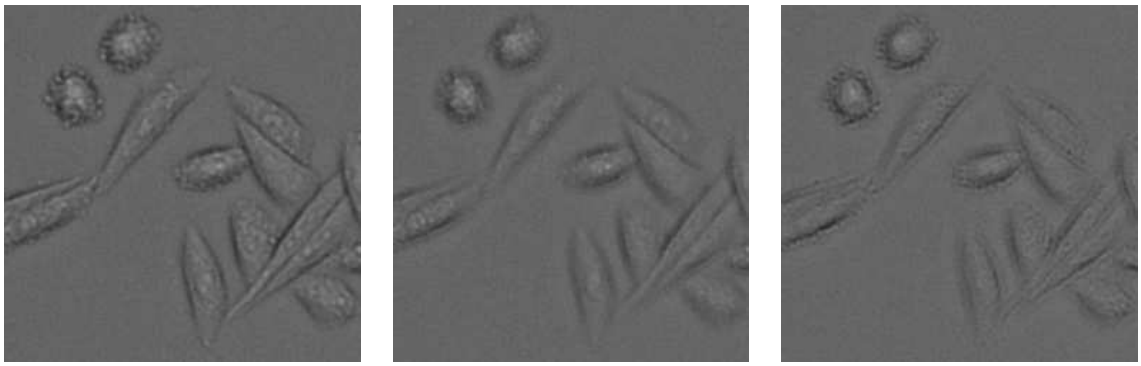

(a) At −5 µm (b) At-focus (c) At +5 µm

Figure 4.4: Images of three slightly different focus positions that were used as input to reconstruct the phase shift of light

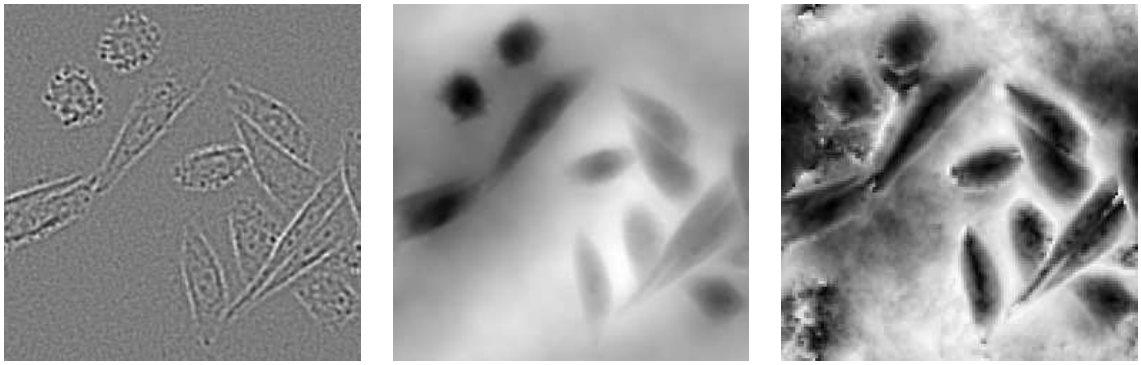

(a) Result of iterative approach (two iterations) (b) Result of TIE solution (c) Result of LMLP

Figure 4.5: Resulting phase images after applying three different phase retrieval methods

Ali et al. [Ali 11b] used the monogenic signal to approximate the result of the TIE (see previous section). For this approximation, a low-pass filter was used instead of a band-pass filter. As second change, the difference image of the two equally defocused images (positively and negatively) are used as input instead of the image itself.
As low-pass filter they used

$$l(r) = \left[\frac{1}{r^{\alpha+\beta}} - \frac{1}{r^{\alpha-\beta}}\right], \tag{4.12}$$

where $r = \sqrt{x^2 + y^2}$ and $\alpha$ and $\beta$ are filter parameters that are set to 0.25 according to [Ali 11b].

### 4.2.4 Results

Images acquired at the different focus positions are necessary for applying all three phase retrieval approaches. Three input images at focus, positively, and negatively defocused (5 µm) are shown in Figure 4.4. All three images are needed for the

iterative approach and for the TIE solution. For calculating the LMLP image the two defocused images are sufficient.

The results of the three approaches are shown in Figure 4.5. Unfortunately, the phase retrieval results could not be used for COSIR systems. The first reason was that our bioprocess engineering partners did not see any benefit in the resulting images. Another reason was that exact and reproducible focus changes were not possible with COSIR systems until the end of the research project. Furthermore the exact mapping between focus changes (applying different voltage levels to the hardware) and distances was not available and hysteresis (see Section 2.5) prevented exact focusing. The runtime of the iterative approach was too slow for using it for each image (2.3 seconds for one iteration according to Weigand [Weig 13]). TIE and LMLP images showed low frequency noise.

However, doing research with the phase retrieval algorithms described in Section 4.2.2 and Section 4.2.3 inspired my colleague Firas Mualla to use these methods and the resulting images for his research. He was able to improve cell/background classification and joint learning for the detection of adherent and suspended cells. Next to other cell image analysis algorithms, these results will be presented in the next chapter.

# Chapter 5

# Cell Image Analysis

The basis for non-invasive cell monitoring with novel bright field miniature microscopy prototypes was laid in the previous chapters. After controlling the hardware (Chapter 2), supporting the hardware development (Chapter 3) and preprocessing the resulting images (Chapter 4) users of the system are able to observe what happens inside the wells (using images) without opening the incubator. In the next step, we did research on cell image analysis algorithms that can be used for generating growth curves (see Figure 1.8) automatically. First, we developed algorithms for cell counting (see Section 5.1) to determine the number of cells in an image. Second, we investigated features for cell viability determination (see Section 5.2) to differentiate between living and dead cells.

In contrast to the previous chapters, the algorithms and results presented in this chapter are mainly not the work of the author of this thesis. They are mainly the contribution of Firas Mualla and therefore only roughly presented. Detailed information can be found in the cited publications and in the PhD thesis of Firas Mualla. Nevertheless, the author and Firas Mualla worked closely together in the same research project COSIR and the author did the following contributions for the algorithms presented in this chapter:

- Introducing Firas Mualla to the project COSIR and all details about cells and cell cultivation.
- Development of the image analysis questions relevant for COSIR with all project partners.
- Many fruitful discussions about a lot of details regarding the algorithms in this chapter.
- Research on phase retrieval (see Section 4.2) was input for the algorithms in Section 5.1.3 and Section 5.1.2.
- Implementation of the algorithms in Section 5.1.1 and Section 5.2 into the C++/CLI image processing library.

## 5.1 Cell Counting

Algorithms for cell counting have an image as input parameter and (at least) the number of cells as output. The number of cells over the time can be used to generate growth curves automatically. There are different algorithm categories to get the number of cells. The categories are listed in Table 5.1.

| Category | Output |
|---|---|
| Cell counting | Only the number of cells |
| Cell detection | Cell centre coordinates |
| Cell segmentation | Cell border delineation |

Table 5.1: Different algorithm categories for getting the number of cells in an image

We decided to concentrate on cell detection methods. These methods have important advantages over cell counting methods. The resulting points inside the cells can later be used for cell tracking and they can be visualized to allow the user of the COSIR system a visual inspection of the result. Cell segmentation is a very hard task especially for bright field images. The cell borders are not visible in images at-focus.

A robust cell detection algorithm is presented in Section 5.1.1. An improvement of the algorithm for joint learning for the detection of a combination of adherent and suspended cells can be found in Section 5.1.2. In Section 5.1.3, the advantage of using LMPL images (see Section 4.2.3) instead of the original images for the cell/background classification is shown.

### 5.1.1 Robust Cell Detection

The cell detection algorithm should fulfil some criteria:

- The algorithm should be adaptable to different cell lines. Therefore, it was designed based on machine learning.
- The algorithm should be able to deal with different hardware setups and especially COSIR setups. Therefore, it was made invariant to the size and orientation of the cells and invariant to the illumination condition.
- The algorithm should be usable for new images or cell lines without manual parameter tuning. Therefore, it was designed to be automatic and to adapt its parameters automatically during the training procedure.

The roughly presented cell detection algorithm in this section was published in [Mual 13].

#### Method

An overview of the algorithm pipeline is shown in Figure 5.1. The following main steps were done:

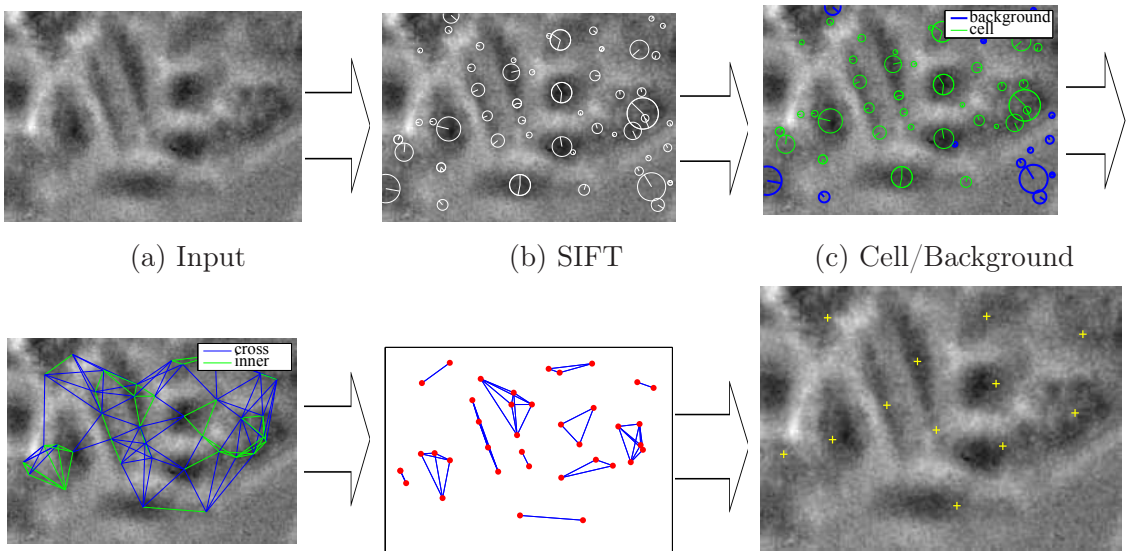


(a) Input (b) SIFT (c) Cell/Background

(d) Inner/Cross profile (e) Hierarchical Clustering (f) Result

Figure 5.1: Cell detection pipeline [Mual 13]

1. Points of interest were found in the input image using the Scale-Invariant Feature Transform (SIFT).

2. A random forest keypoint classifier is used to classify each keypoint as either cell or background keypoint.

3. The background keypoints are removed and only the cell keypoints remain.

4. A random forest profile classifier is used to classify the profiles (connections between cell keypoints) as either inner or cross profiles.

5. Hierarchical clustering is then used to build the clusters of keypoints that belong to single cells.

6. If more than one keypoint is found in a cluster, the keypoint coordinates are averaged to one point.

### Results

The algorithm was evaluated quantitatively for standard bright field images and qualitatively for COSIR images. The results are shown in the next two paragraphs. For standard bright field images, the algorithm was also compared to two other approaches from Ali et al. [Ali 11a] and Becattini et al. [Beca 11]. Table 5.2 shows a comparison with these two approaches regarding the input parameters. First, the number of input images of our approach is one and for the other approaches two or three. Second, our approach needs no manual parameter-tuning whereas the algorithm of Ali et al. [Ali 11a] needs one tuned parameter and the approach of Becattini et al. [Beca 11] more than nine.

| Algorithm | Required number of images | Manually tuned parameters |
|---|---|---|
| Becattini et al. [Beca 11] | 3 | >9 |
| Ali et al. [Ali 11a] | 2 | 1 |
| Mualla et al. [Mual 13] | 1 | 0 |

Table 5.2: A comparison of the input requirements for [Ali 11a], [Beca 11], and [Mual 13]

| Cell line | Description | Images | Cells |
|---|---|---|---|
| CHO | adherent cells | 6 | 1431 |
| L929 | adherent cells | 5 | 1078 |
| Sf21 | cells in suspension | 5 | 1001 |

Table 5.3: The cell lines used for the evaluation

**Standard Bright Field Images** The bright field images used for the evaluation are listed in Table 5.3. Three different cell lines were evaluated. CHO and L929 as mammalian cell lines that tend to adhere and Sf21 as insect cell line that stays in suspension. At least five images and more than 1000 labelled cells are used from each cell line . Results with these images of living cells are relevant for the COSIR systems. Further results with images of simulated cells can be found in [Mual 13].

| Cell line | Precision [%] | Recall [%] |
|---|---|---|
| CHO | 77.7 ± 8.0 | 92.9 ± 3.0 |
| L929 | 82.8 ± 4.4 | 92.6 ± 2.9 |
| Sf21 | 97.3 ± 0.9 | 96.4 ± 3.2 |

Table 5.4: Cell detection accuracy on the different cell lines

The most important evaluation measures (precision and recall) for the cell lines are shown in Table 5.4. Further evaluation measures can be found in [Mual 13]. As expected, the cells in suspension (Sf21) are considerably easier to detect than the adherent cells because of the higher contrast (see Section 1.2.5). For both adherent cell lines the results of the algorithm are similar.

Table 5.5 shows a comparison of the results for CHO cells with Ali et al. [Ali 11a] and Becattini et al. [Beca 11]. Our algorithm outperforms the other approaches.

To test the invariance to the cell size and to the illumination conditions, two changes are done to the original images. An illumination field was applied to all testing and training images and the testing images were resampled using different scales. The detection results are shown in Table 5.6. The results of our approach with the changed images are similar to the previous results, whereas the results of the other approaches are highly influenced. The recall values of 36.5 and 23.4 show that.

| Algorithm | Precision [%] | Recall [%] |
|---|---|---|
| Becattini et al. [Beca 11] | $80.9 \pm 3.2$ | $61.3 \pm 9.3$ |
| Ali et al. [Ali 11a] | $56.1 \pm 11.1$ | $91.8 \pm 3.5$ |
| Mualla et al. [Mual 13] | $88.1 \pm 2.3$ | $87.6 \pm 4.2$ |

Table 5.5: Comparison of the cell detection results for CHO cells with other approaches

| Algorithm | Precision [%] | Recall [%] |
|---|---|---|
| Becattini et al. [Beca 11] | $43.0 \pm 16.2$ | $23.4 \pm 10.6$ |
| Ali et al. [Ali 11a] | $81.0 \pm 12.7$ | $36.5 \pm 18.9$ |
| Mualla et al. [Mual 13] | $80.8 \pm 3.7$ | $91.4 \pm 2.5$ |

Table 5.6: Comparison of the cell detection results with other approaches when illumination and scale are changed

**COSIR Images** As already mentioned above, we did no quantitative evaluation on COSIR images. The reasons are that many images have to be labelled for a quantitative evaluation. Labelling is a very tedious task. One image takes hours and a set of images even days or weeks. As we were working with different prototype systems (e.g. 24 bright field microscope prototypes for one COSIR-24 system) and development stages, we had to deal with different image artefacts over time. Therefore, we decided to do a qualitative analysis. We labelled the image of one well (e.g. A2) and used it for the training of the algorithm. A training image and the corresponding cell mask are shown in Figure 5.2

After the algorithm was trained, the images of the other wells were processed. The results are shown in Figure 5.3, Figure 5.4 and Figure 5.5. Overall, the result of a visual qualitative evaluation is that the algorithm works well for COSIR images. The results of two wells are special. In well B1 there are some wrong hitpoints because of an unexpected object (perhaps a hair) in the image (see Figure 5.3f). Such objects in the image degrade detection results. In well C4 (see Figure 5.4f) the left side is darker than the right side and their is a vertical border in the middle of the image. The detection results are not influenced by this border. This is another example for the invariance regarding the illumination field in an image.

### 5.1.2 Joint Learning for Detection of Adherent and Suspended Cells

Although the algorithm presented in the previous section performed very well, there is one point that is worth looking at more closely. All presented results are generated with separate learning. That means, that for the detection results of CHO cells the algorithm was trained only with images of CHO cells. Similarly, for the Sf21 results, the algorithm was trained only with images of Sf21 cells. It would be beneficial to have an algorithm that can be trained with adherent and suspended cells (which is called joint learning) which has almost the same results as for separate learning. As

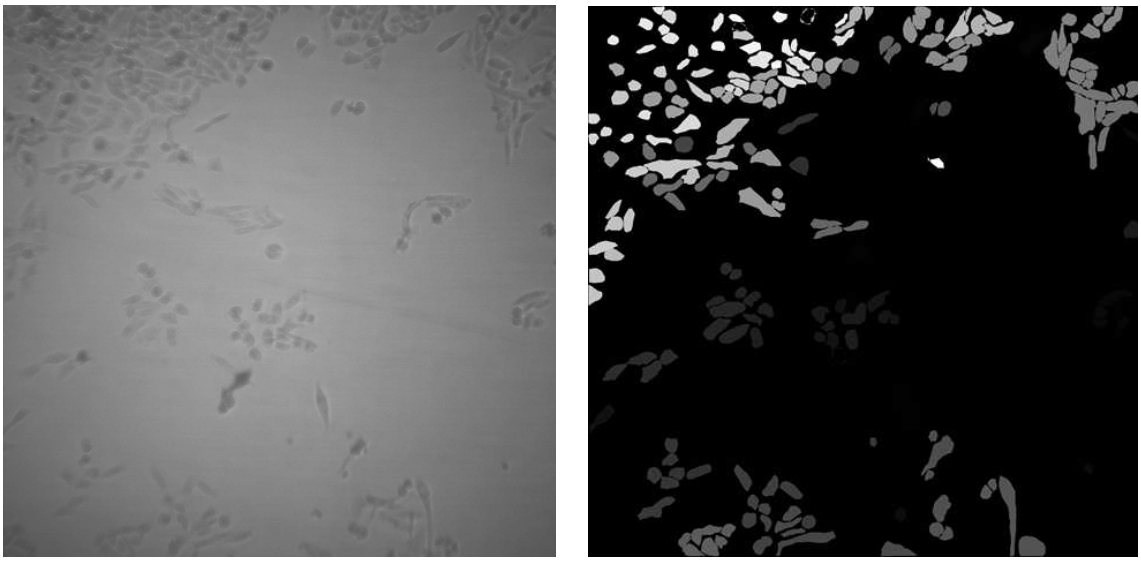

(a) Training image (b) Training mask

Figure 5.2: Training data for COSIR

reported in [Mual 14b], for the cell detection algorithm described in Section 5.1.1, the F-measure for detecting suspended cells is reduced by 10.4% when joint learning was used compared to separate learning. This section describes how the algorithm is adapted to perform better for joint learning and the results of these adaptions.

The roughly presented algorithm and the results in this section were published in [Mual 14b].

### Method

In principle, the cell detection algorithm described in Section 5.1.1 is used, but two adjustments were done. Three images are used: an image at-focus and two equally defocused images. An LMLP image (see Section 4.2.3) and a TIE image (see Section 4.2.2) are calculated from the input images. These images are used for the feature extraction of the keypoint and the profile features. The other algorithm steps are performed on the positively defocused image similar to the original algorithm.

### Results

| **Algorithm** | **Joint learning** | | **Separate learning** | |
|---|---|---|---|---|
| | **Adherent** | **Suspended** | **Adherent** | **Suspended** |
| Mualla et al. [Mual 13] | 84.2 | 86.6 | 85.3 | 97.0 |
| Mualla et al. [Mual 14b] | 83.6 | 96.3 | 85.5 | 97.8 |

Table 5.7: F-measure values [%] for the two cell detection approaches [Mual 14b] and [Mual 13].

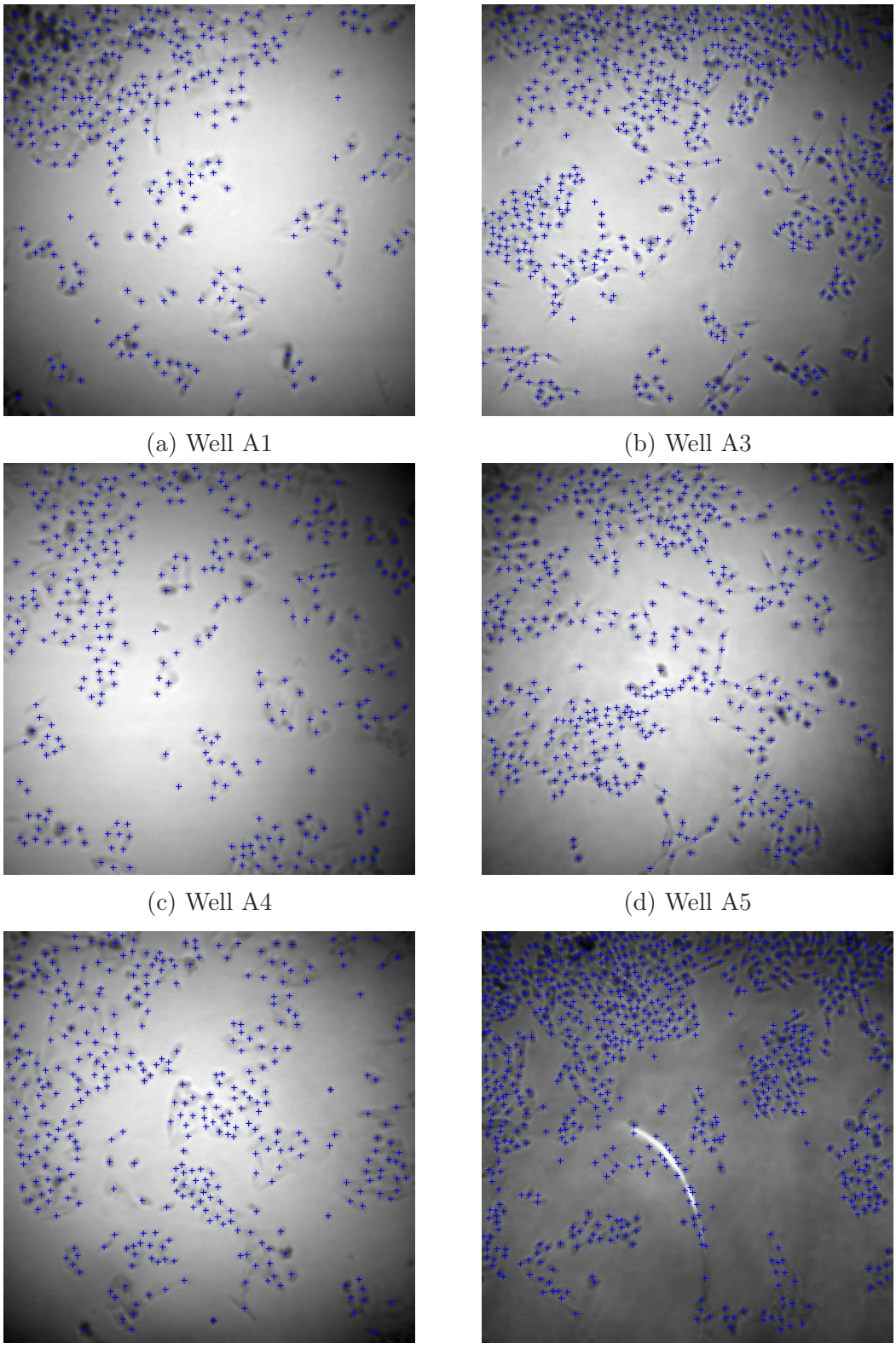

(a) Well A1 (b) Well A3

(c) Well A4 (d) Well A5

(e) Well A6 (f) Well B1

Figure 5.3: Results of the cell detection for COSIR-24 images - part 1

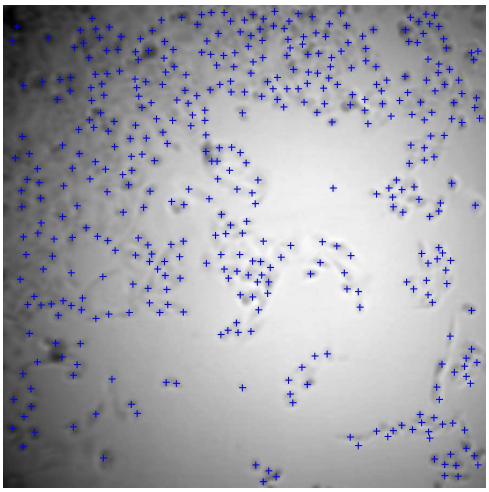

(a) Well B2

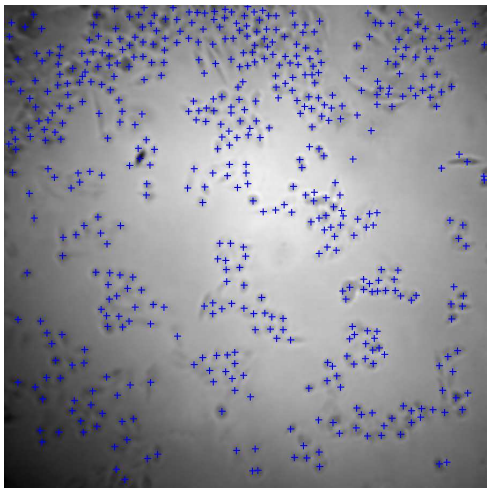

(b) Well B4

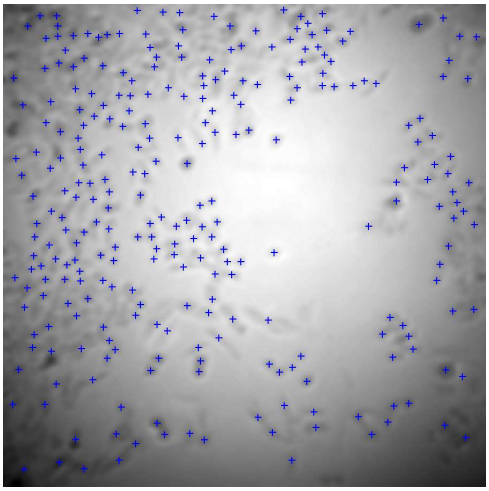

(c) Well C1

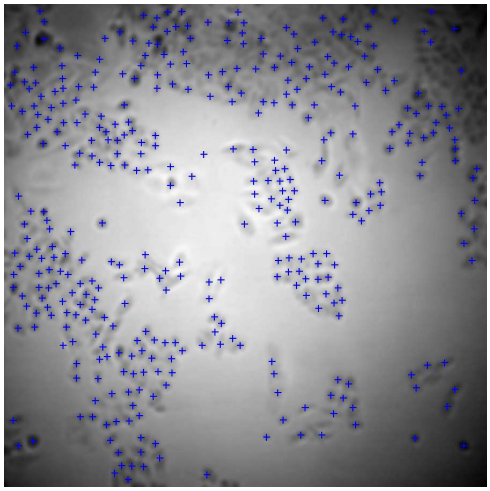

(d) Well C2

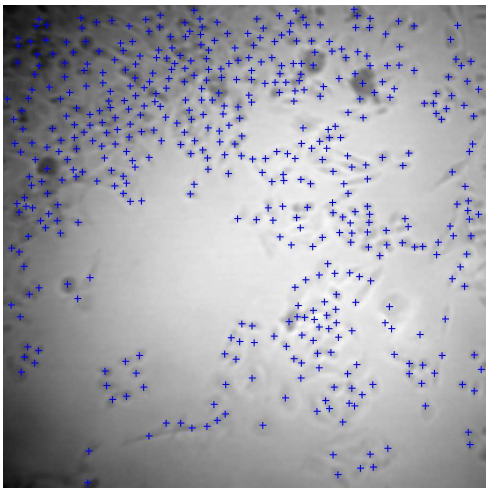

(e) Well C3

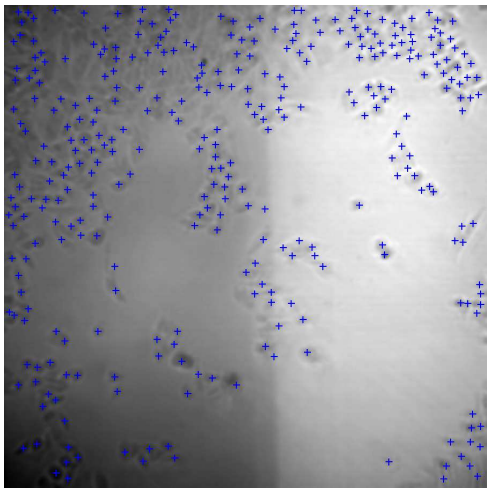

(f) Well C4

Figure 5.4: Results of the cell detection for COSIR-24 images - part 2

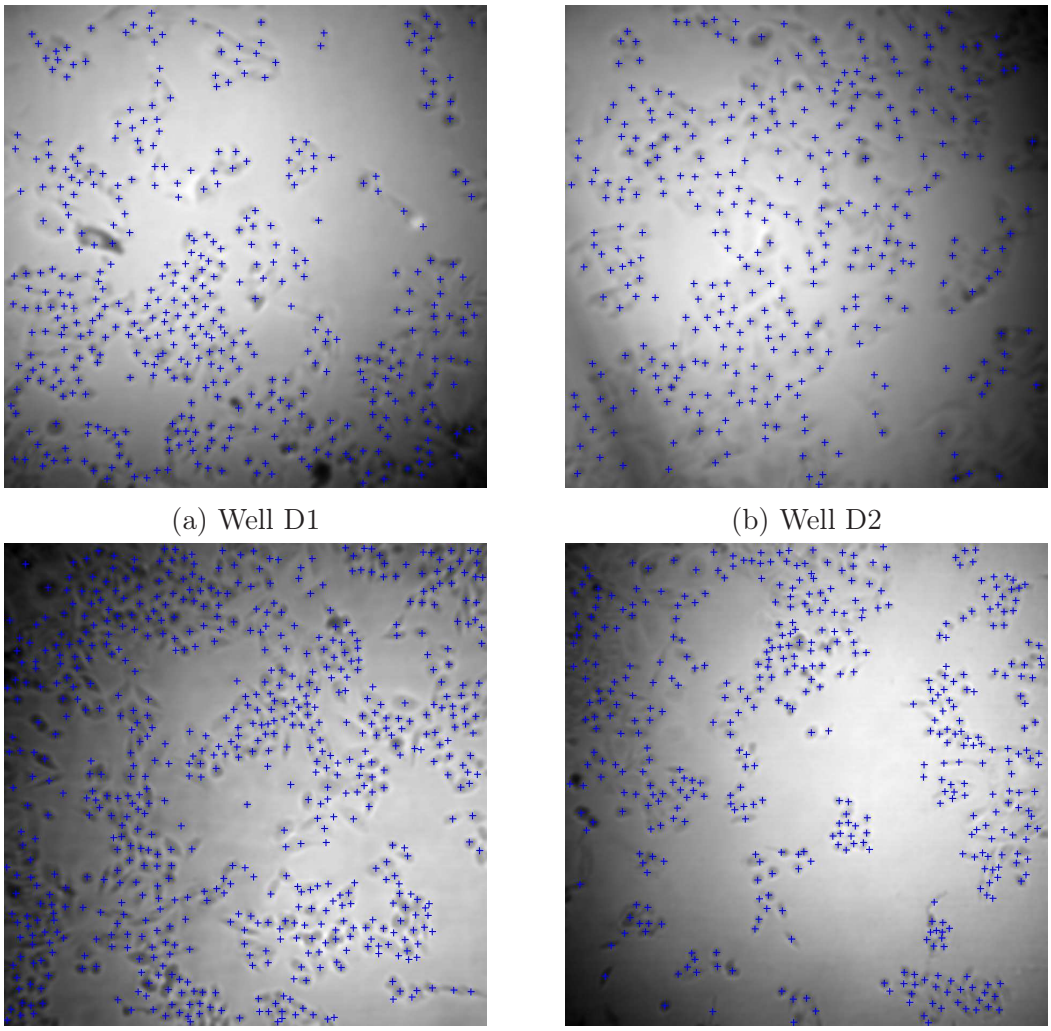

(a) Well D1 (b) Well D2

(c) Well D3 (d) Well D4

Figure 5.5: Results of the cell detection for COSIR-24 images - part 3

The cell image data from Table 5.3 is used for the evaluation. As mentioned earlier, the cell lines CHO and L929 are adherent and the cell line Sf21 is suspended. Detailed evaluations can be found in [Mual 14b]. The best result regarding joint learning is shown in Table 5.7. For the results of joint learning shown in Table 5.7, the TIE image is used for the keypoint feature extraction and the LMLP image for the profile feature extraction.

It was shown that phase retrieval methods such as TIE or LMLP can improve cell detection results especially for joint learning.

### 5.1.3 Cell/Background Classification

The previous sections introduced approaches where the cell detection is done based on extracted keypoints. Most approaches for cell detection do not use keypoints. They classify each pixel into either cell or background using the pixels of a fixed-size patch [Sjos 99, Long 05, Long 06]. In this section, we show that the cell/background

classification results using the pixel intensities of LMLP images as features outperform the results when using the pixel intensities from bright field images.

The roughly presented algorithm and the results in this section were published in [Mual 14a]. More details and evaluations can be found there.

### Evaluation

The same material that was used in the last two sections (see Table 5.3) was also used for this evaluation. The LMLP image (see Section 4.2.3) was calculated using the at-focus and the positively defocused image. The LMLP, the at-focus, and the positively defocused images were used for the comparison.

Machine learning was used to evaluate the discriminative power. Support vector machine (SVM) with the linear kernel, SVM with the radial basis function (RBF) kernel, and random forests were used as classifiers. The pixel values of $5px \times 5px$ sized patches were used as features. To train the classifier, 100 random patches of an image were used. In order to have balanced training data, 50 background and 50 cell patches were used. Mixed patches (containing cell and background pixels) were discarded.

### Results

| Cell line | At-focus [%] | Defocused [%] | LMLP [%] |
|---|---|---|---|
| L929 | 51.2 ± 1.0 | 67.7 ± 0.5 | 82.4 ± 1.1 |
| CHO | 49.8 ± 0.8 | 60.9 ± 1.2 | 68.5 ± 1.7 |
| Sf21 | 59.6 ± 1.2 | 82.5 ± 1.2 | 94.9 ± 0.7 |

Table 5.8: Comparison of the classification rates of cell/background classification for different cell lines using the at-focus, the positively defocused, and the LMLP image

Table 5.8 shows the mean and the standard deviation of the classification rates for the classifier SVM with linear kernel. These results show the following order regarding the discriminative power: LMLP, defocused image, at-focus image. The other results in [Mual 14a] confirm this observation and as a conclusion of all experiments we stated that the computed LMLP image "considerably outperforms the defocused image for the purpose of pixel-patch cell/background classification in bright field microscopy".

## 5.2 Cell Viability Determination

The robust cell detection methods introduced in this chapter enable us to get the total number of cells from bright field microscopy and COSIR images over time. Therefore, growth curves of cell cultures can be generated. However, growth curves normally do not contain the total number of cells over time. They contain the number of living cells. Especially for toxicity tests (where a substance that can damage the cells is added to the cell culture), the growth curves have to show the number of living cells over time instead of the total number of cells. Therefore, we started to investigate the

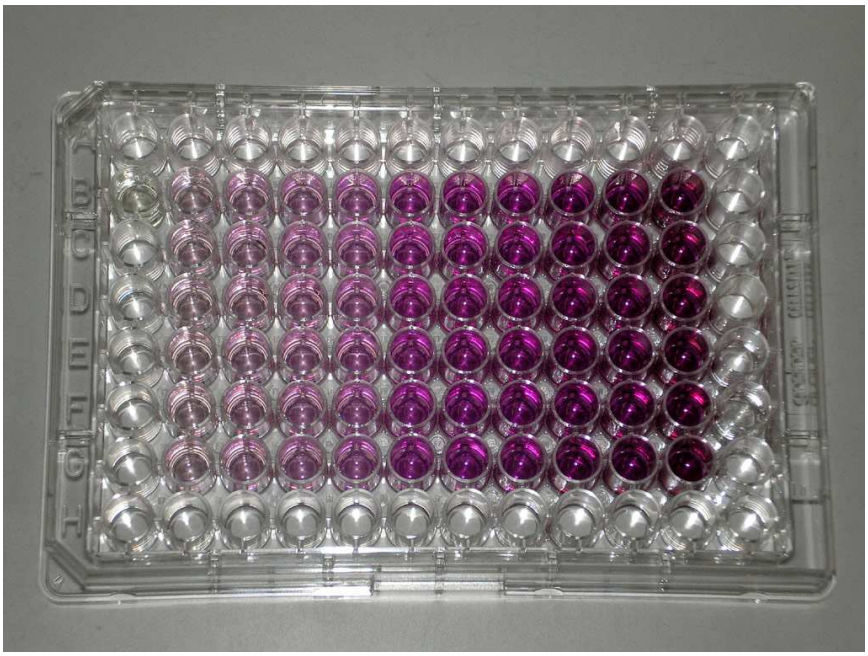

Figure 5.6: MTT assay

differentiation between living (viable) and dead (non-viable) cells. The first results are shown in this section. The section is based on the Master's thesis of E. van Heerden [Heer 13].

### 5.2.1 Material

After multiple discussions with our partners from the Institute of Bioprocess Engineering, it became clear that differentiating between viable and non-viable cells is a complex task. One aspect is that there are many different forms of cell death. Exemplary forms of cell death are apoptosis (the programmed cell death of unneeded cells), oncosis (the accidental cell death), or necrosis (cell are dead for a longer time). Different toxins can cause dying cells. The effect of one toxin can lead to different reactions depending on the cell line. Because of all these different parameters, we reduced the complexity and the side effects of our investigations by using only one cell line (CHO) and only one toxin (sodium azide).

Another special aspect of differentiating viable from non-viable cells is, that even an expert cannot identify dead cells in a standard bright field image of cells. However, we needed to find a way to obtain ground truth data for bright field images as the COSIR system is a bright field microscope.

When we visited laboratories where cells are cultivated, we found out that mainly two ways were used to determine the cell viability: MTT assays and trypan blue staining. These two approaches are completely different. MTT assays are used to measure the metabolic activity of the cells. MTT is a yellow tetrazolium salt that is added to a well. Viable cells are able to reduce the salt to the purple formazan. After a while, the colour of the whole well changes to purple. The exact wavelength of the colour is measured and used to calculate the number of living cells. Figure 5.6

shows a microtiter plate that was used for a toxicity test (different amounts of toxin in different wells) after a MTT test was performed. The results of a MTT test can be used to get the viability of a whole well but they cannot be used to determine if a single cell in an image is dead or not. The method is especially used for toxicity tests.

The other commonly used method to generate cell counts for growth curves is trypan blue method which is described in Section 1.3.2. This method is based on the permeable cell membrane of dead cells. Although the bluish cells can be used to identify dead cells with a bright field microscope, the method cannot be used. Adding trypan blue to a cell culture just works for a while. The actual dead cells become blue. After some time, all cells die because of the stain and also become blue. As ground truth data we need a labelled bright field image. Acquiring a bright field image and adding trypan blue afterwards to generate the labelling failed, because when the stain was added all cells moved away before they became blue.

Dyes that change the visual appearance of the cells cannot be used to generate labelled data. Propidium iodide (PI) is another commonly-used stain which is fluorescent and therefore not visible in the generated bright field image. The dead cells are shown in the red fluorescence channel (see Figure 1.6a).

The CHO cells for the experiments were grown at 37.0 °C in a DMEM/F-12 medium supplemented with 10% fetal calf serum and 2 mmol Glutamine. The toxin sodium azide (0.1 mol) was added to the cell culture. Before the images were acquired, PI was added to the cell culture. Bright field images and fluorescence images were then acquired. Seven image sets were acquired when approximately 25% of the cells were non-viable. An image set consists of three bright field images (at-focus, positively defocused, and negatively defocused) and a fluorescence (PI) image. The defocus distance for the bright field images was 10 µm. In the bright field images, the cells were labelled as three different classes: viable-adherent, viable suspended, and non-viable (using the PI image).

### 5.2.2 Method

In general, a classifier is trained with one image using a specific feature set and evaluated on the other images. In [Heer 13], many variations of this general approach were described and evaluated. The following classifiers were used: SVM with linear kernel, SVM with RBF kernel, and random forests. The investigated features were: the SIFT descriptor, ray features (according to [Mual 13]), the intensity stencil (according to [Mual 13]), the variance map (according to [Mual 13]), Gray and colour Haralick texture features (the extracted patch intensity is quantized to 16, 32, 64, 128, or 256 levels). For the texture features, either fixed-size pixel patches are used (patch's half side length is the average scale of SIFT keypoints) or patches with a dynamic size (patch's half side length is the scale of the corresponding SIFT keypoint).

### 5.2.3 Results

Many combinations of classifiers, feature sets, and patch types were evaluated and detailed results can be found in [Heer 13]. The best results for dynamic patches

| Focus | Classification rate [%] | Feature set | Classifier |
|---|---|---|---|
| At-focus | 88.28 ± 1.34 | Stencil | SVM: RBF |
| Negatively defocused | 88.40 ± 0.65 | Stencil | SVM: RBF |
| Positively defocused | 88.11 ± 0.40 | Stencil | SVM: RBF |

Table 5.9: The feature/classifier combinations that yielded the best classification rates for the differentiation between viable-suspended and non-viable cells ([Heer 13])

| Focus | Classification rate [%] | Feature set | Classifier |
|---|---|---|---|
| At-focus | 67.68 ± 2.37 | CTex128 | SVM: Linear |
| Negatively defocused | 69.90 ± 1.07 | SIFT descriptor | RF |
| Positively defocused | 65.21 ± 2.62 | CTex128 | RF |

Table 5.10: The feature/classifier combinations that yielded the best classification rates for the differentiation between viable-adherent and non-viable cells ([Heer 13]). CTex128 is the abbreviation for the colour Haralick texture features using 128 quantization levels

and for all three focus positions are listed in Table 5.9 and Table 5.10. The best classification rate for the differentiation between viable-suspended and non-viable cells is 88.40%±0.65% (see Table 5.9). The best classification rate for viable-adherent vs. non-viable cells that could be achieved is 69.90% ± 1.07% (see Table 5.10). Both results were achieved for the negatively defocused image.
The main results of the study are:

- The classification rate of non-viable vs. viable-suspended cells outperforms the classification rate of non-viable vs. viable-adherent cells by about 20%.
- The results are almost the same for the at-focus image and the negatively and positively defocused bright field images.
- The results are almost the same for the three classifiers SVM with linear kernel, SVM with RBF kernel and random forests.
- A dynamic patch size outperforms a static patch size (data not shown).
- The most discriminative features for classifying non-viable cells are the intensity stencil, the variance map and the colour texture features quantized with 32 levels (data not shown).

# Chapter 6

# Implementation

During the research project many software applications and tools became necessary and were developed. The basic software architecture for them is described in Section 6.1. As main software part, an image processing library was designed and implemented. This library and its architectural concepts are described in Section 6.2. The most important application that uses this library is the cell monitoring software for the COSIR prototypes. This application is presented in Section 6.3. Besides this application, other image processing tools were developed (see Section 6.4). These tools support, for example, the development and the evaluation of algorithms.

## 6.1 Software Architecture

The main architectural layers for the developed software applications are shown in Figure 6.1. Different programming languages were used for the layers because of their different purposes. For the business logic of all applications C# was used, because it is a simple, modern, general-purpose, object-oriented programming language [ECMA 06] and the author and many other company members of ASTRUM IT are used to it.

For the user interface (presentation layer) the Windows Presentation Foundation (WPF) is used as state-of-the-art technology using the programming language C#. WPF is a graphical framework which is part of the .NET framework that is used as well. For displaying graphs such as focus curves, the WPF library Dynamic Data Display was also included in the user interfaces of the applications.

The other two layers are related to the image processing libraries which is described in more detail in the next section. For performance and memory reasons most common image processing libraries are written in C++. Two of these external libraries are included in our image processing library. There are two common ways to access such C++ libraries from C#:

- direct access from C# using Platform Invocation Services
- a wrapper between native C++ and the managed C# using the programming language C++/CLI [ECMA 05].

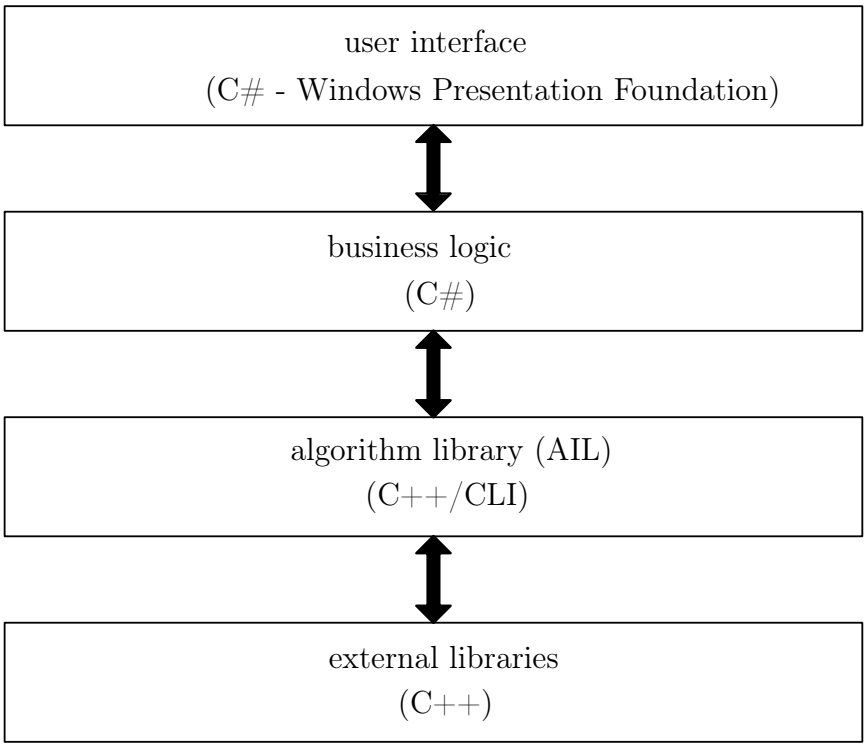


Figure 6.1: Architectural layers used for all software applications

For this thesis the second option was used. This approach supports separating the image processing algorithms from the business logic and it also completely hides the native C++ code for business logic programmers.

## 6.2 C++/CLI Image Processing Library

The C++/CLI image processing library is the software part that contains the implementation of all algorithms described in this thesis. It is also called ASTRUM image library (AIL).

### 6.2.1 Software Architecture

The Common Language Infrastructure (CLI) is an ECMA [ECMA 12] (and also ISO and IEC) standard that specifies a system for application development. The standard itself is independent from platforms and programming languages. The best-known implementation is the .NET framework that was developed by Microsoft for the operating system Microsoft Windows. Different CLI programming languages can be used. All of them are compiled to the Common Intermediate Language (CIL). The CIL code is compiled to native code during the execution of a program by the just-in-time compiler Common Language Runtime (CLR).

The programming languages C# and C++/CLI are both CLI languages. C++/CLI allows to use managed and native (C++) programming in parallel. Classes, for example, can be managed or native. They are differentiated by their syntax:

- A native class is generated if the syntax **class** is used.
- A managed class is generated if the syntax **ref class** is used.

Public methods of managed classes of the AIL can be used in all applications including this library. A main difference between managed and unmanaged objects is that managed objects are affected by the automatic garbage collection. The memory for them is allocated and released automatically. The majority of the library is therefore managed. Nevertheless, huge native objects such as the image itself stay native. They are never converted to managed objects.
Two external C++ (and C) libraries were included:

- Intel Integrated Performance Primitives (Intel IPP) because of the high performance for basic image processing operations.
- OpenCV because it contains diverse computer vision functionalities such as object detection, feature detectors and descriptors.

The AIL can be separated into two main parts:

- images – basic infrastructure for the images.
- modules – mostly static classes for algorithms that analyse or manipulate the images

The main classes for the images are shown in Figure 6.2. The *InternalImage* is the native class that contains the image data itself. The image is stored in the OpenCV format *cv::Mat* and can be used for both libraries (OpenCV and Intel IPP) without copying. The pointer to the pixel data that is necessary for Intel IPP is returned by the method *ImageData* of the *InternalImage*. To hide the native image and its operations, the abstract class *GenericImage* is introduced as base class for all managed images. It contains properties and methods that all derived image classes should implement such as the properties *Width* and *Height*. From the class *GenericImage* image classes are derived for the different types used. One example is *Image8u* (see Figure 6.2), others are *Image8uC3*, *Image16u* or *Image32fc*. They contain type related operations such as *GetAt* or *SetAt*. Concrete type-specific classes were used because the interface to the Intel IPP shows different methods for images with different types.

The main modules of the AIL are shown in Figure 6.3. The classes in the upper part of the diagram (i.e. ArithmeticOperations, ImageStatistics, Filter and, GeometryTransform) contain low level functions with reduced complexity. They were used by the classes in the lower parts that contain algorithms with higher complexity. The class *AlgorithmicOperations* for example contains basic mathematical operations such as adding, subtracting, multiplying or dividing that are performed on two images or on an image and a scalar value. Other functions are for example the calculation of absolute values, square roots or squared values. The class *ImageStatistics* contain methods for calculating values such as minimum, maximum, mean or standard deviation. This class can be also used to compute image histograms. The class *Autofocus* includes all focus measures described in Section 2.4.2.

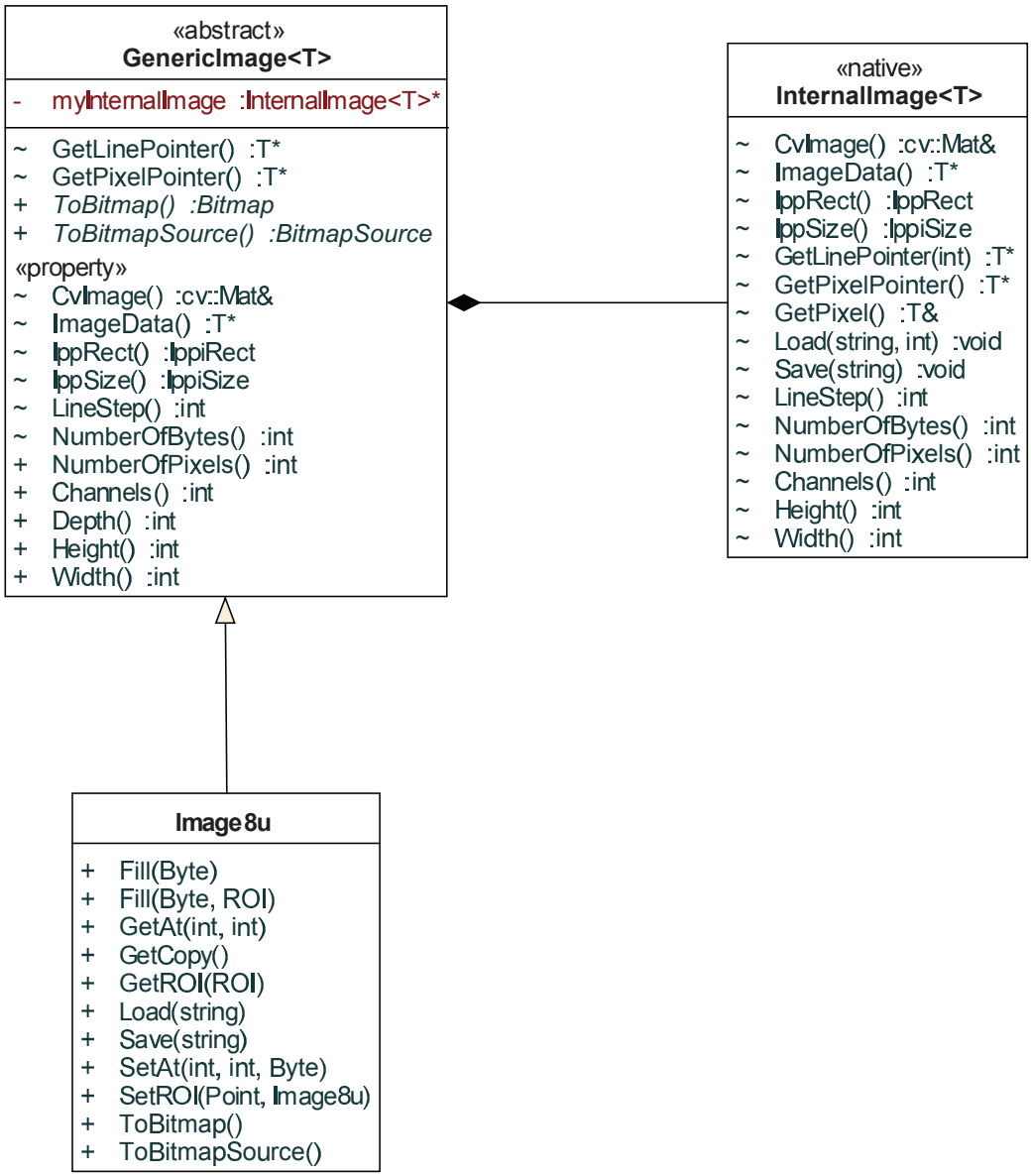


Figure 6.2: AIL basic image classes and their dependencies

### 6.2.2 Continuous Integration

Continuous integration is a good practice in software engineering. The goal is to reach a higher software quality. After submitting software changes to the source control, system building the software and executing related tests is done automatically. Another goal is to keep the changes small and submit them several times per day [Mart 06]. The AIL was developed using these principles and is included in a continuous integration system. As a source control system, Subversion is used and as automated continuous integration server CruiseControl.NET is used. The library is automatically built after each check-in using the Microsoft Build Engine.

While developing the library itself also component tests were developed. These tests helped to validate the algorithms and kept them working correctly even when central parts of the library were refactored. The component tests were developed to

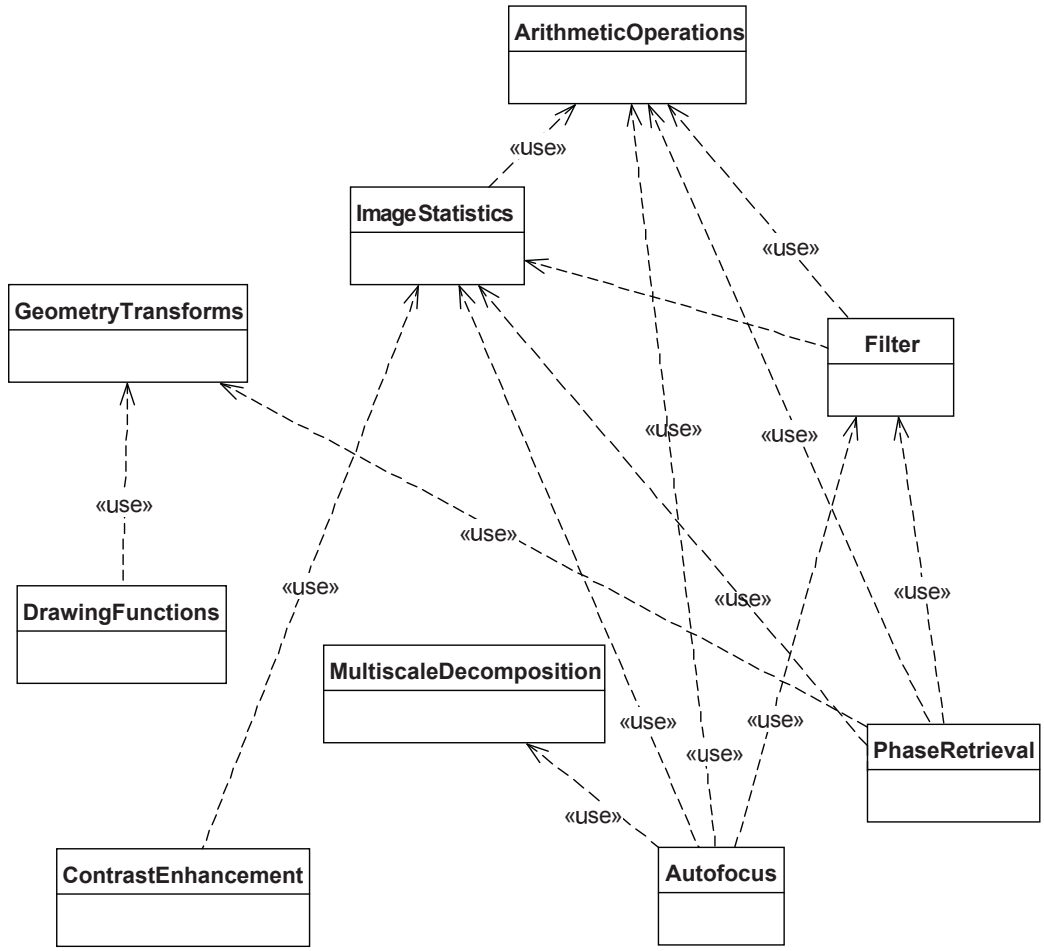


Figure 6.3: AIL basic modules and their dependencies

test the whole library and its usage from other programs. As a consequence C# was used as programming language for the tests. NUnit was used as testing framework. According to Osherove [Oshe 09], a continuous integration build should run all tests in less than 10 minutes. All tests of the AIL are executed in about 40 seconds. The symbol coverage of the AIL is 84.49%, which shows the high level of test coverage.

## 6.3 COSIR Cell Monitoring Software

One central software was developed within the research project COSIR. The first phase in the development of this software was the requirements analysis. Usability engineering methods were used to focus on the users of the software. Users of this software are cultivating cells in an incubator as their daily business and want to observe them from outside. Potential users are working at university institutes with laboratories or at pharmaceutical companies. The project partners of the Institute of Bioprocess Engineering of the Friedrich-Alexander-Universität Erlangen-Nürnberg were the potential users. They were interviewed many times to understand their vocabulary and their needs. They were also observed in their working environment while cultivating cells to get an understanding of their tasks, problems and needs in

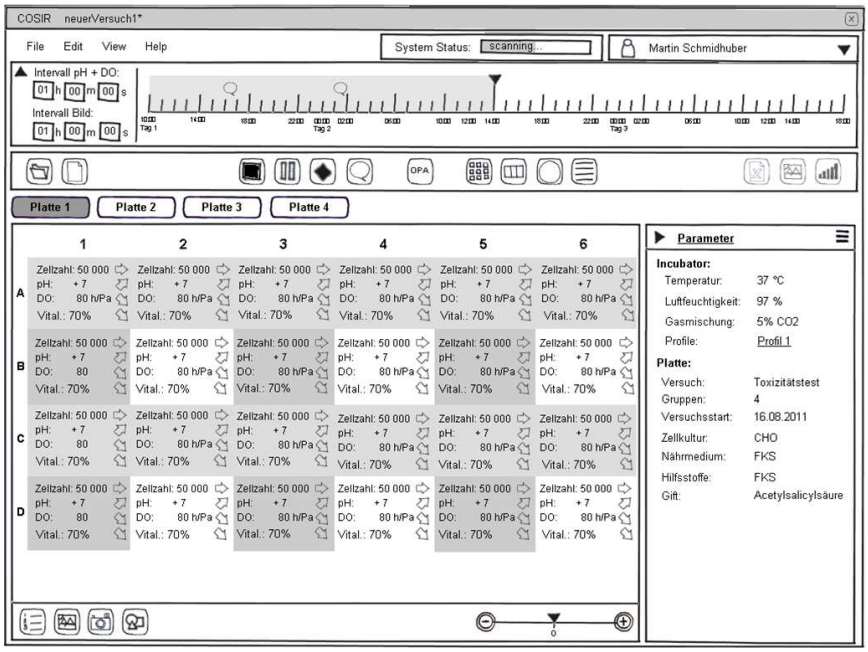


Figure 6.4: Mockup of the graphical user interface

reality. As a result of this phase a requirements specification was written containing the information about the different users, their working environment, their workflows and the user requirements regarding the whole COSIR system.

After knowing the most important user requirements the design phase of the software was started. One task was to derive the concept for the user interface. The first drafts were done on a sketch block and on white boards. As next step mockups of the user interface (see Figure 6.4) were created with the tool Balsamiq Mockups. The different drafts were created by a usability engineer and discussed with the project lead (author of the thesis) and the partners of the Institute of Bioprocess Engineering. The discussion results led to changes in the concepts until the most important remarks were considered.

The interaction is the effect of action on the screens. For example a click on a button causes changes on the screen (or even an exchange of the whole screen). The interaction concept was tested with a usability test with five different users from the Institute of Bioprocess Engineering. They did not see drafts or mockups of the user interface before this test. They had to fulfil some tasks using a clickable PDF file that included the user interface and interaction concept. The comments and reactions of the subjects were recorded and evaluated afterwards to improve the concept of the user interface and the interaction concept. The final concept for the user interface and all system requirements derived from the user requirements were summarized in a functional specification for the COSIR software. A screenshot of the software at the end of the research project COSIR is shown in Figure 6.5.
The software works with the following hardware systems:

- no COSIR system
- one COSIR-1

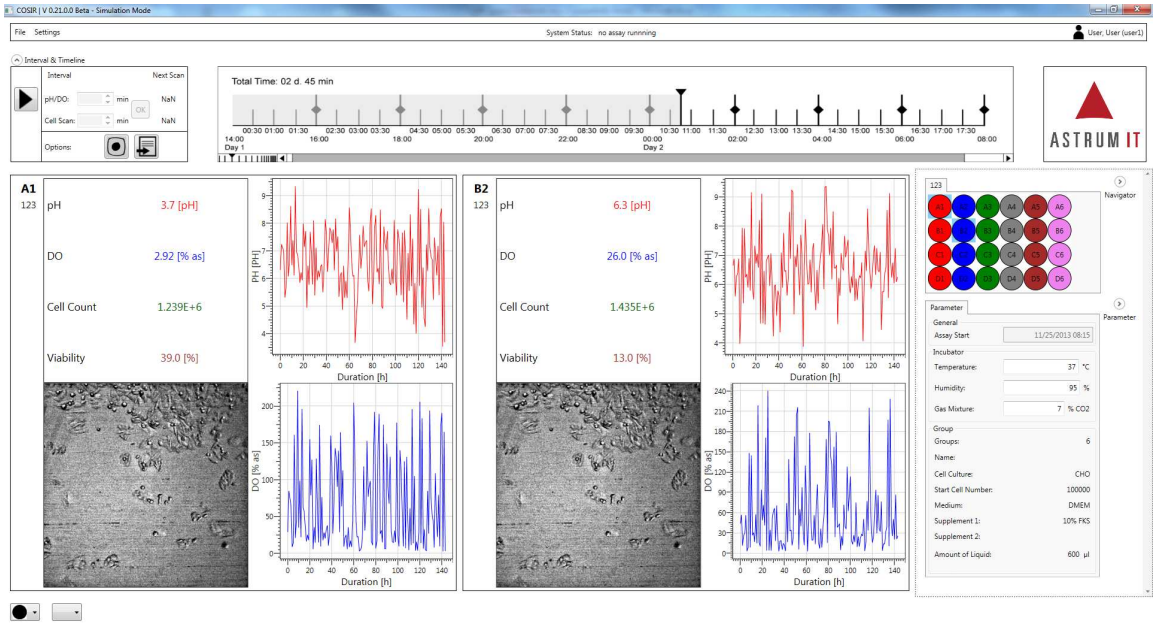


Figure 6.5: User interface of the cell monitoring software at the end of the research project COSIR. An assay with simulated values is loaded and the results of two wells are compared.

- one COSIR-2
- one COSIR-24
- two COSIR-24

That means that the software works with all COSIR setups that were and are available. If a COSIR system with less than 24 microscope units or less than 24 measuring units for pH and DO is connected, the missing measured values and images are simulated.
The usage of the software has three stages:

1. preparation of the assay
2. monitoring of the assay
3. evaluation of the assay

In the preparation phase the user puts a prepared well plate on the COSIR hardware system inside the incubator. Afterwards he can use the software to start the monitoring of the cell cultures from outside. A wizard guides him through this process. He can enter the general parameters of the assay (for example the name of the assay), choose the COSIR devices he wants to use and load calibrations according to Section 2.2. Then he can define the different contents of the single wells to the software and combine wells to groups for evaluation purposes. As last step of the preparation phase the scanning intervals for the pH and DO sensors and for image acquisition can be entered. After finishing the wizard the monitoring phase starts.

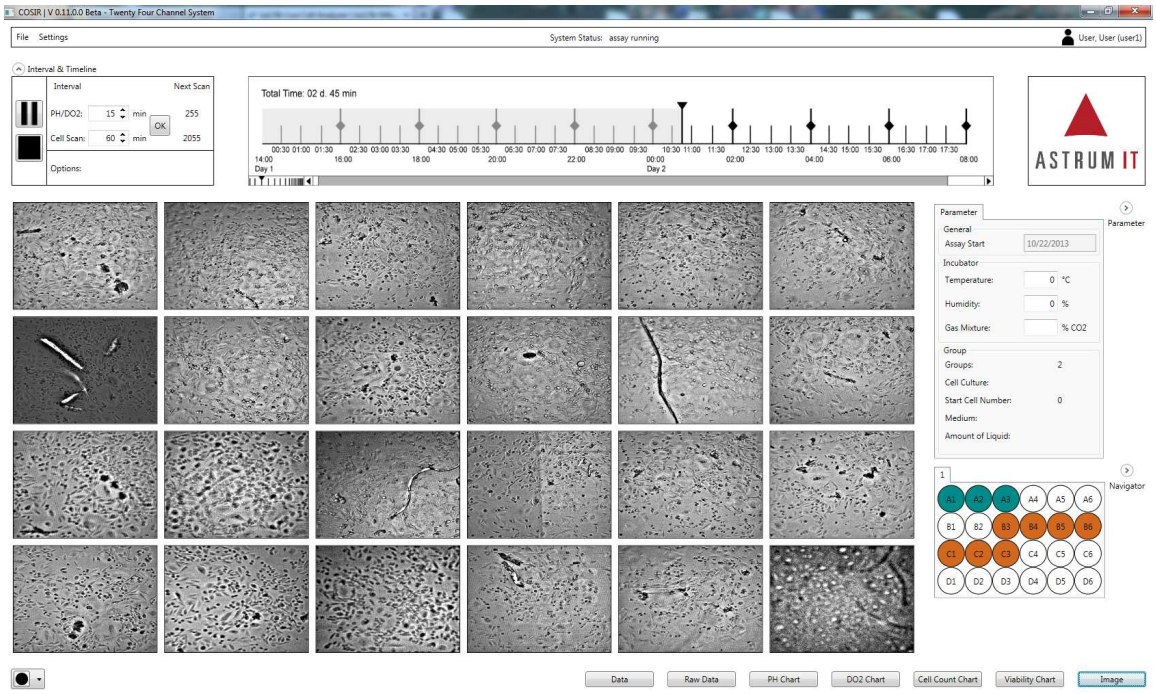


Figure 6.6: Resulting images when the cell monitoring software was used the first time with the COSIR-24 system and CHO cells

The monitoring phase of cell cultures can take days or even weeks. For example toxicity tests commonly take two days before the evaluation is done. In the monitoring phase the software continuously retrieves pH ad DO values and images from the hardware. For the acquisition of the first image the exposure is adapted according to Section 2.3.2. For each image acquisition (also the first one) the algorithms for automatic exposure (Section 2.3.1), automatic focus (Section 2.5), illumination correction (Section 4.1.1) and contrast enhancement (Section 4.1.2) are executed. For the automatic calculation of the cell count, the algorithms are implemented (see Section 5.1 and Section 6.4.2) but not yet included in the monitoring software. Values for the cell count and the viability rate are simulated. For an automatic calculation of the viability first algorithmic steps were done (see Section 5.2) but more work is required. The resulting images acquired with the COSIR software and the COSIR-24 system after it was delivered to the Institute of Bioprocess Engineering and tested the first time with CHO cell cultures are shown in Figure 6.6.

The evaluation phase follows the monitoring phase. Typically the user needs to evaluate all measured values to draw important conclusions for his research. Therefore, the user can use plots in the software to analyse how the measured values developed. He can evaluate a single well, compare two wells, analyse a well group or have a look at the whole plate with 24 wells at one point in time. The measured values over the time can also be exported to the Microsoft Excel file format.

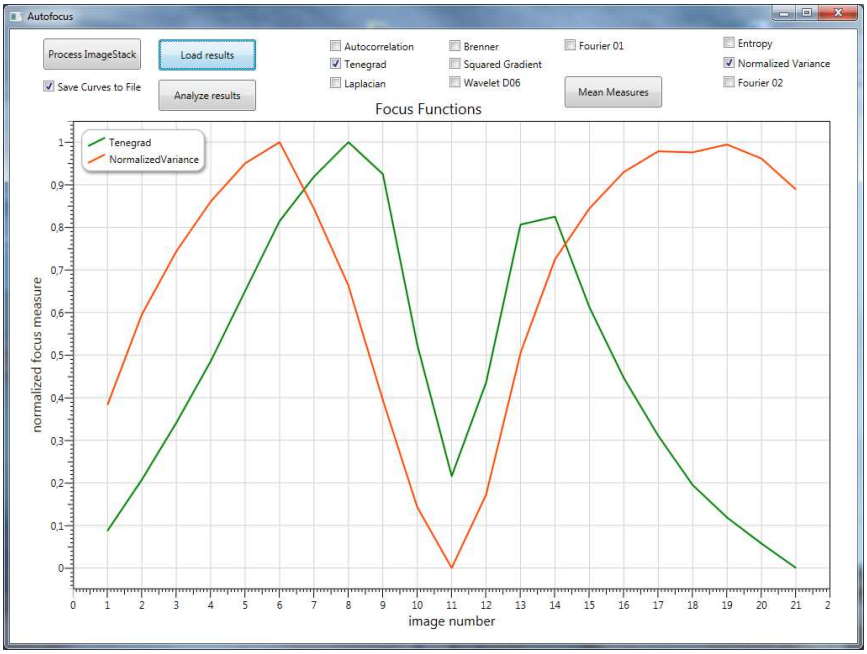


Figure 6.7: Tool to calculate focus measures and analyse focus stacks

## 6.4 Image Processing Tools

Many tools were written based on the AIL to support project partners and algorithm development. The most simple tools, for example, convert colour images to grayscale images, crop image parts or enhance the contrast in the images. To make the calibration procedure easier, a tool was written that automatically determines the parameters of the image region around the illumination centre (see Section 2.2). Another tool was used to automatically remove the horizontal lines that were visible in the images with one hardware version (see Section 3.3). For the phase retrieval experiments a tool was created that can calculate phase retrieval results using the transport of intensity equation, using the monogenic signal or iteratively (see Section 4.2).

Besides all these tools, two more important ones were developed. They are presented in the next two sections.

### 6.4.1 Focus Tool

The library AIL contains all focus measures described in Section 2.4.2. The Focus Tool is the software that enables the user to use them. Image stacks can be selected and all focus measures are calculated for the images and stored in a text file. The format of the text file is compatible with gnuplot. The resulting graphs are displayed in the tool and can be investigated there. The user interface of the tool is shown in Figure 6.7. All the results in the Chapters 2 and 3 that are related to focus measures were generated using this tool. The tool was also distributed to our hardware partners PreSens and the Institute of Bioprocess Engineering. After explaining to them how focus curves should look like, they used the tool to generate the curves and they reported their feedback which helped us to improve the tool.

### 6.4.2 Cell Counting Tool

The fundamental algorithms for acquiring images are already included in the cell monitoring software. All of them were first implemented in the AIL and afterwards tested with component tests and software tools built for one particular purpose.

The number of cells is simulated in the cell monitoring software. The robust cell detection algorithm (see Section 5.1.1) performs well on COSIR images. Therefore, this algorithm is added to the AIL. The implementation was done in an object oriented way and the class diagram is displayed in Figure 6.8.

The main class is the *CellDetector*. The methods *Train* and *Detect* are public. Obviously, *Train* is used to train the algorithm and *Detect* is used to apply the training results to a given image. The class *CellMap* stores the labelled cells (see Figure 5.2b) and provides methods to analyse them. All points belonging to one cell have the same value in the *CellMap*. Points of different cells have different values. The parameters for the training procedure are Images (*Image8U*) and their labels (*CellMap*). The training results are stored in the properties *CellBackgroundClassifier*, *ProfileClassifier*, *BlobTypeDecision*, *DOGThreshold* and *MaximumInnerCellDistance*. The parameter for the detection is an image (*Image8U*). The detected cell centre coordinates are returned in a list of 2D points.

Methods for the extraction of the features used for the cell detection are part of the class *FeatureDetection*. The class contains methods for extracting all features mentioned in Chapter 5. In addition to cell detection features, Haralick texture features used for the viability determination (see Section 5.2) are available. The list of SIFT keypoints extracted from an image are stored in the class *SIFTKeypoints*. This class offers methods for reducing the keypoints according to different criteria and methods for getting statistics such as the average scale of all keypoints.
With component tests the algorithm was applied to the images shown in Table 5.3.

A graphical user interface (GUI) was developed to make the algorithm available to our project partners. The GUI is shown in Figure 6.9. The tool allows to train and detect consecutively or to save the training results. After starting the tool, training results can be loaded and the detection can start directly.

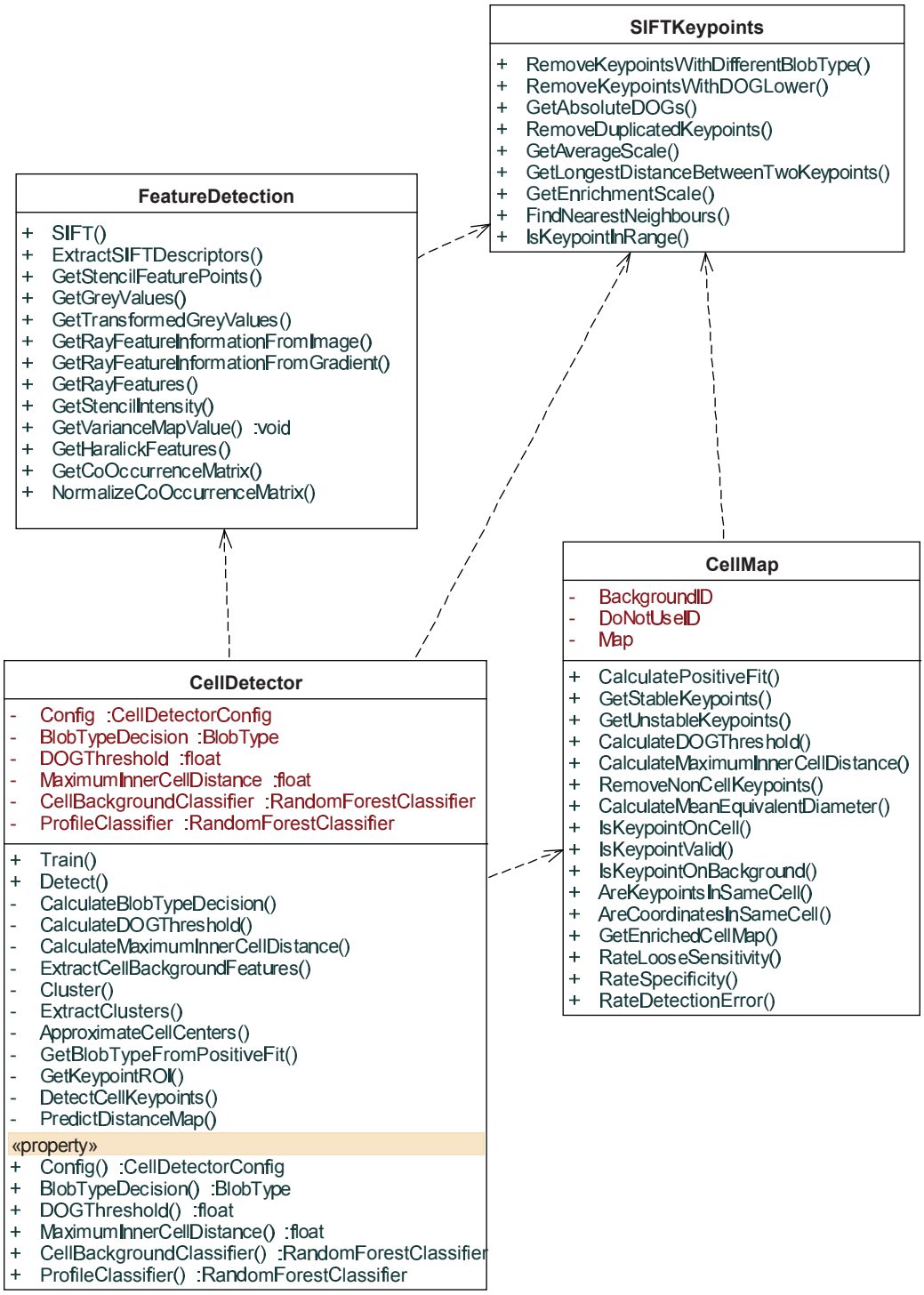


Figure 6.8: Main classes used in the AIL to implement the cell detection algorithm from Mualla et al [Mual13]

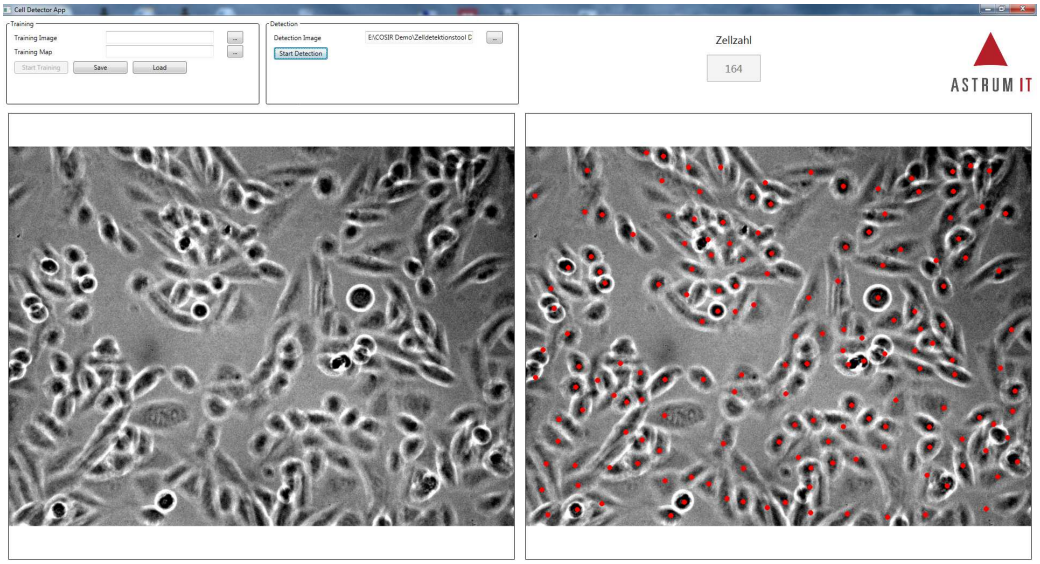


Figure 6.9: Cell Counting Tool using the AIL-based implementation of [Mual 13]. The input image is shown on the left side and the detection results are presented on the right side. Each detected cell is marked by a red point

# Chapter 7

# Summary and Outlook

## 7.1 Summary

Two major contributions were presented in this thesis. First, a pipeline was introduced that made the novel bright field microscope systems usable for cell monitoring in an incubator. Second, the influence of the phase effect on focus curves of bright field microscope images was investigated in detail. Moreover, other contributions to the cell image analysis in COSIR were presented. In the following text, we summarize the final statements of this work.

The whole pipeline for the novel microscope systems was shown in Figure 4.1. A calibration procedure was presented (see Section 2.2) that needs to be done once for each system. The result of the calibration is the relevant image area, initial exposure settings and an initial focus position. At the beginning of each experiment the initial exposure settings are applied and adapted to the actual illumination conditions. Four steps are then automatically done for each image. First, the exposure settings are checked again and adapted if illumination conditions changed. Second, the focus position is adapted. Third, the illumination is corrected and finally the contrast is enhanced. A cell monitoring software (see Section 6.3) was developed containing the whole pipeline. The pipeline enabled the novel microscope systems to be used for cell monitoring in an incubator.

We showed that the typical use of focus measures is likely to fail for bright field microscopes in the presence of the phase effect (see Section 2.4). We made the following important observations for focus curves of phase objects. First, the optical focus is at a local minimum when gradient-based focus measures are used and the images show homogeneous cells (i.e. if most cells tend to lie in the same focal plane). Second, inhomogeneous cells lead to typical focus curves if gradient-based focus measures are used due to the constructive overlapping of differently shaped focus curves from different image regions. Third, for both homogeneous and inhomogeneous cells, statistic-based focus measures tend to have a local minimum instead of a global maximum at the focus position. Fourth, for homogeneous cells, experts prefer focus positions that diverge considerably from the optical focus.

Five different focus positions were identified for phase objects that can be found automatically. These positions seem to be useful for different applications. The optical focus position is at the PEC minimum and the resulting image can be used

for applications such as phase retrieval. Two important focus positions are located at the PEC maxima of gradient-based focus measures. The slightly defocused cell images at the two aforementioned maxima show a high contrast at small details and they can be thus used for applications such as cell segmentation or cell analysis. Other two focus positions are at the PEC maxima of statistic-based focus measures. The strongly defocused cell images at these two maxima show a high contrast at the cell borders and they can be used for applications such as cell detection.

Minor contributions regarding all bright field microscopes are summarized in the next two paragraphs. Three different methods for retrieving the physical phase of light from images of different focus positions were applied to bright field images (see Section 4.2). An iterative solution, the TIE solution and an LMLP image can be calculated from bright field images. Firas Mualla showed that the discriminative power of the intensities in the LMLP image is higher than the discriminative power of the intensities in the original bright field image (see Section 5.1.3). He also used the TIE solution and the LMLP image to improve joint learning for cell detection of adherent and suspended cells in bright field images (see Section 5.1.2).

Moreover, first results were achieved regarding cell viability determination (see Section 5.2). One cell line and one toxin were used for the study. Two classifications were done: Non-viable/viable-adherent cells and non-viable/viable-suspended cells. The classification rate of non-viable vs. viable-suspended cells outperformed the classification rate of non-viable vs. viable-adherent cells by about 20%. The results for the at-focus image and the negatively and positively defocused bright field images were almost the same. The most discriminative features for classifying non-viable cells were the intensity stencil, the variance map and the colour texture features quantized with 32 levels.

Minor contributions regarding especially the novel bright field microscope systems are summarized in the next paragraphs. The development of the hardware system was supported by designing experiments and analysing image processing results such as focus curves (see Chapter 3). The light path in the system was determined using our experiments. A lens that caused a lateral focus irregularity could be identified. Analyses of focus curves revealed that the quantization step size of focus changes needs to be adapted. The analyses also revealed that the waiting time between a focus change and the image acquisition needs to be increased. Furthermore, inappropriate positions of the lens regarding the object could be identified. Horizontal lines originating from a low frequency of the light source pulses could be removed. Finally, unusable microtiter plates could be identified and therefore exchanged.

An image processing library using C++/CLI and a cell monitoring software using this library were developed (see Chapter 6). All steps of the pipeline, a robust algorithm for cell detection and features used for the cell viability determination study were integrated in this library.

## 7.2 Outlook

The research project COSIR was very interesting and the range of research topics was manifold. The outlook therefore covers many different topics.

In this paragraph an outlook for the novel microscope systems is presented. The exact mapping between voltage changes and focus position changes should be derived. The hysteresis effect that appears for the focus changes needs to be investigated in detail and an exact model should be derived. As soon as the focus changes of the system are described exactly, a comparison of different focus measures can be done. Depending on this comparison the best focus measure for the novel systems can be selected. The knowledge about the influence of the phase effect can then be included into the algorithm for finding the focus position automatically. The algorithm can be extended to acquire from one to five images at different focus positions (see above) for phase objects. A quantitative evaluation of the integrated cell detection algorithm can be done on images of the novel system. Physical phase images can be generated for the COSIR system and it can be evaluated, if the joint learning for adherent and suspended cells is improved.

Regarding the influence of the phase effect on focus curves of bright field microscope images, it can be investigated if the proposed five positions are optimal for the proposed applications (see Section 2.4.6). It can also be investigated if a classification of phase and amplitude objects (homogeneous and inhomogeneous cell objects) can be done using patches and focus curves (see Figure 2.15).

Phase retrieval is a huge research area. A quantitative evaluation can be done using the mentioned methods. Research can be done on removing the low frequency noise in TIE results. Suitable methods for COSIR and bright field images can be derived.

Regarding the cell viability determination on unstained bright field images many further steps are necessary. Evaluations can be done on more images, cell lines and toxins to find out if the same features have a high discriminative power for all cases. A combination of the tested features and further features can be evaluated. Including information of cell changes through time seems promising to improve the classification rates.

Further algorithms can be developed that would be helpful for the presented system. Cell tracking can be realized using images from different time stamps and the cell detection results. Motion patterns of the cells can be derived and visualized. Cell segmentation can be done to derive many parameters such as the cell size or the cell diameter. Changes in the cell size over the time can indicate different events such as that the cell starts to die or died some time ago. Cell divisions can be detected in the images over the time. The confluency of the well plate can be extracted. All these parameters would help a user of the system to draw conclusions for his experiments.

# Appendix A

# Acronyms

| | |
|---|---|
| AIL | ASTRUM image library |
| BF | bright field |
| CHO | Chinese hamster ovary |
| CIL | Common Intermediate Language |
| CLI | Common Language Infrastructure |
| CLR | Common Language Runtime |
| COSIR | Combination of Chemical-Optical Sensors and Image Recognition |
| DNA | deoxyribonucleic acid |
| DMEM | Dulbecco's Modified Eagle Medium |
| DO | dissolved oxygen |
| FCS | fetal calf serum |
| FSP | free space propagation |
| GUI | graphical user interface |
| LED | light-emitting diode |
| LMLP | low-pass monogenic local phase |
| MUT | material under test |
| NA | numerical aperture |
| PEC | phase effect characteristic |
| PI | propidium iodide |
| RBF | radial basis function |
| ROI | region of interest |
| SIFT | scale-invariant feature transform |
| SVM | support vector maschine |
| TIE | transport of intensity equation |
| WPF | Windows Presentation Foundation |

# List of Figures

# List of Tables

# Bibliography


[Ager 03] U. Agero, C. Monken, C. Ropert, R. Gazzinelli, and O. Mesquita. "Cell surface fluctuations studied with defocusing microscopy". *Physical Review E*, Vol. 67, No. 5, pp. 051904–1–051904–9, May 2003.

[Albe 05] B. Alberts, D. Bray, K. Hopkin, A. Johnson, J. Lewis, M. Raff, K. Roberts, and P. Walter. *Lehrbuch der Molekularen Zellbiologie*. Wiley, Weinheim, Germany, 2005.

[Ali 11a] R. Ali, M. Gooding, T. Szilágyi, B. Vojnovic, M. Christlieb, and M. Brady. "Automatic segmentation of adherent biological cell boundaries and nuclei from brightfield microscopy images". *Machine Vision and Applications*, Vol. 23, No. 4, pp. 607–621, July 2011.

[Ali 11b] R. Ali, T. n. Szilágyi, M. Gooding, M. Christlieb, and M. Brady. "On the Use of Low-Pass Filters for Image Processing with Inverse Laplacian Models". *Journal of Mathematical Imaging and Vision*, Vol. 43, No. 2, pp. 156–165, June 2011.

[Alle 01] L. J. Allen and M. P. Oxley. "Phase retrieval from series of images obtained by defocus variation". *Optical Communications*, Vol. 199, No. 1-4, pp. 65–75, November 2001.

[Beca 11] G. Becattini, L. S. Mattos, and D. G. Caldwell. "A novel framework for automated targeting of unstained living cells in bright field microscopy". In: *Proceedings of 2011 8th IEEE International Symposium on Biomedical Imaging: From Nano to Macro, Chicago, Illinois, United States, March 30 – April 2*, pp. 195–198, 2011.

[Bren 76] J. F. Brenner, B. S. Dew, J. B. Horton, T. King, P. W. Neurath, and W. D. Selles. "An automated microscope for cytologic research a preliminary evaluation". *Journal of Histochemistry & Cytochemistry*, Vol. 24, No. 1, pp. 100–111, January 1976.

[Daub 92] I. Daubechies. *Ten Lectures on Wavelets*. Society for Industrial and Applied Mathematics, Philadelphia, Pennsylvania, United States, 1992.

[Dulb 59] R. Dulbecco and G. Freeman. "Plaque production by the polyoma virus". *Virology*, Vol. 8, No. 3, pp. 396–397, July 1959.

[ECMA 05] ECMA. *ECMA-372: C++ /CLI Language Specification*. 1st Ed., December 2005.

[ECMA 06] ECMA. *ECMA-334: C# Language Specification*. 4th Ed., June 2006.

[ECMA 12] ECMA. *ECMA-335: Common Language Infrastructure (CLI)*. 6th Ed., June 2012.

[Fels 01] M. Felsberg and G. Sommer. "The monogenic signal". *IEEE Transactions on Signal Processing*, Vol. 49, No. 12, pp. 3136–3144, December 2001.

[Fire 91] L. Firestone, K. Cook, K. Culp, N. Talsania, and K. Preston. "Comparison of autofocus methods for automated microscopy". *Cytometry*, Vol. 12, No. 3, pp. 195–206, 1991.

[Gao 10] D. Gao, D. Padfield, J. Rittscher, and R. McKay. "Automated Training Data Generation for Microscopy Focus Classification". In: T. Jiang, N. Navab, J. P. Pluim, and M. A. Viergever, Eds., *Medical Image Computing and Computer-Assisted Intervention – MICCAI 2010, Beijing, China, September 20 – 24*, pp. 446–453, 2010.

[Gerc 72] R. W. Gerchberg and W. O. Saxton. "A Practical Algorithm for the Determination of Phase from Image and Diffraction Plane Pictures". *Optik*, Vol. 35, No. 2, pp. 237–246, 1972.

[Ghat 10] K. Ghatak. *Techniques and Methods in Biology*. Prentice-Hall of India Pvt. Ltd., New Delhi, Delhi, India, 2010.

[Groe 85] F. C. Groen, I. T. Young, and G. Ligthart. "A comparison of different focus functions for use in autofocus algorithms". *Cytometry*, Vol. 6, No. 2, pp. 81–91, March 1985.

[Gros 10] E. Grossman, R. Tzioni, A. Gur, E. Gur, and Z. Zalevsky. "Optical through-turbulence imaging configuration: experimental validation". *Optics Letters*, Vol. 35, No. 4, pp. 453–455, February 2010.

[Gstr 13] G. Gstraunthaler and T. Lindl. *Zell- und Gewebekultur: Allgemeine Grundlagen und spezielle Anwendungen*. Springer-Verlag, Berlin Heidelberg, Germany, 2013.

[Ham 63] R. Ham. "An improved nutrient solution for diploid Chinese hamster and human cell lines". *Experimental Cell Research*, Vol. 29, No. 3, pp. 515–526, February 1963.

[Ham 65] R. Ham. "Clonal Growth of Mammalian Cells in a Chemically Defined, Synthetic Medium". *Proceedings of the National Academy of Sciences*, Vol. 53, No. 2, pp. 288–293, February 1965.

[Hamm 10] P. Hamm, J. Schulz, and K.-H. Englmeier. "Content-Based Autofocusing in Automated Microscopy". *Image Analysis & Stereology*, Vol. 29, No. 3, pp. 173–180, November 2010.

[Hech 09] E. Hecht. *Optik*. Oldenbourg Verlag, München, Germany, 2009.

[Heer 13] E. van Heerden. *Automatic Cell Viability Determination In Bright-Field Microscope Images*. Master's thesis, Pattern Recognition Lab, Department of Computer Science, Friedrich-Alexander Universität Erlangen Nürnberg, Germany, September 2013.

[Hook 65] R. Hooke. *Micrographia: Or Some Physiological Descriptions of Minute Bodies Made by Magnifying Glasses with Observations and Inquiries Thereupon*. Royal Society, London, England, 1665.

[Kimu 10] A. Kimura Junior, M. G. Costa, C. F. F. Costa Filho, L. B. M. Fujimoto, and J. Salem. "Evaluation of autofocus functions of conventional sputum smear microscopy for tuberculosis". In: *Engineering in Medicine and*

*Biology Society (EMBC), 2010 Annual International Conference of the IEEE, Buenos Aires, Argentina, August 31 – September 04*, pp. 3041–3044, 2010.

[Klin 03] R. Klinke and S. Silbernagl. *Lehrbuch der Physiologie*. Georg Thieme Verlag, Stuttgart, Germany, 2003.

[Lang 13] G. Lang. *Histotechnik: Praxislehrbuch für die Biomedizinische Analytik*. Springer-Verlag, Wien, Austria, 2013.

[Lian 12] Q. Liang and Y. F. Qu. "A texture-analysis-based design method for self-adaptive focus criterion function". *Journal of Microscopy*, Vol. 246, No. 2, pp. 190–201, May 2012.

[Liu 07] X. Y. Liu, W. H. Wang, and Y. Sun. "Dynamic evaluation of autofocusing for automated microscopic analysis of blood smear and pap smear". *Journal of Microscopy*, Vol. 227, No. 1, pp. 15–23, July 2007.

[Long 05] X. Long, W. Cleveland, and Y. Yao. "A new preprocessing approach for cell recognition". *IEEE Transactions on Information Technology in Biomedicine*, Vol. 9, No. 3, pp. 407–412, September 2005.

[Long 06] X. Long, W. L. Cleveland, and Y. L. Yao. "Automatic detection of unstained viable cells in bright field images using a support vector machine with an improved training procedure". *Computers in Biology and Medicine*, Vol. 36, No. 4, pp. 339–362, April 2006.

[Makk 09] V. V. Makkapati. "Segmentation based microscope autofocusing for blood smears". In: N. Karssemeijer and M. L. Giger, Eds., *SPIE Proceedings Vol. 7260: Medical Imaging 2009: Computer-Aided Diagnosis, Lake Buena Vista, Florida, United States, February 7 – 12*, pp. 72603D–1–72603D–8, 2009.

[Mart 06] R. C. Martin and M. Martin. *Agile Principles, Patterns, and Practices in C#*. Prentice Hall PTR, Upper Saddle River, New Jersey, United States, 2006.

[Mise 73] D. L. Misell. "A method for the solution of the phase problem in electron microscopy". *Journal of Physics D: Applied Physics*, Vol. 6, No. 1, p. L6, 1973.

[Mual 13] F. Mualla, S. Schöll, B. Sommerfeldt, A. Maier, and J. Hornegger. "Automatic Cell Detection in Bright-Field Microscope Images Using SIFT, Random Forests, and Hierarchical Clustering". *IEEE Transactions on Medical Imaging*, Vol. 32, No. 12, pp. 2274–2286, December 2013.

[Mual 14a] F. Mualla, S. Schöll, B. Sommerfeldt, A. Maier, S. Steidl, R. Buchholz, and J. Hornegger. "Using the low-pass monogenic signal framework for cell/background classification on multiple cell lines in bright-field microscope images". *International Journal of Computer Assisted Radiology and Surgery*, Vol. 9, No. 3, pp. 379–386, May 2014.

[Mual 14b] F. Mualla, S. Schöll, B. Sommerfeldt, S. Steidl, R. Buchholz, and J. Hornegger. "Improving joint learning of suspended and adherent cell detection using low-pass monogenic phase and transport of intensity equation". In: *2014 IEEE 11th International Symposium on Biomedical Imaging (ISBI), Beijing, China, April 29 – May 2*, pp. 927–930, April 2014.

[Ohno 97] Y. Ohno. "NIST Measurement Services: Photometric Calibration". Tech. Rep. 250-37, National Institute of Standards and Technology (NIST), 1997.

[Oshe 09] R. Osherove. *The Art of Unit Testing: With Examples in .NET*. Manning Publications Co., Greenwich, Connecticut, United States, 1st Ed., 2009.

[Osib 10] O. a. Osibote, R. Dendere, S. Krishnan, and T. S. Douglas. "Automated focusing in bright-field microscopy for tuberculosis detection". *Journal of Microscopy*, Vol. 240, No. 2, pp. 155–163, November 2010.

[Paga 98] D. Paganin and K. Nugent. "Noninterferometric Phase Imaging with Partially Coherent Light". *Physical Review Letters*, Vol. 80, No. 12, pp. 2586–2589, March 1998.

[Pope 11] G. Popescu. *Quantitative Phase Imaging of Cells and Tissues*. McGraw-Hill, New York, United States, 2011.

[Redo 12] R. Redondo, G. Bueno, J. C. Valdiviezo, R. Nava, G. Cristóbal, O. Déniz, M. García-Rojo, J. Salido, M. D. M. Fernández, J. Vidal, and B. Escalante-Ramírez. "Autofocus evaluation for brightfield microscopy pathology". *Journal of Biomedical Optics*, Vol. 17, No. 3, p. 036008, March 2012.

[Sant 97] A. Santos, C. Ortiz de Solórzano, J. J. Vaquero, J. M. Peña, N. Malpica, and F. del Pozo. "Evaluation of autofocus functions in molecular cytogenetic analysis". *Journal of Microscopy*, Vol. 188, No. 3, pp. 264–272, December 1997.

[Schm 11] S. Schmitz. *Der Experimentator: Zellkultur*. Spektrum Akademischer Verlag, Heidelberg, Germany, 2011.

[Scho 14a] S. Schöll, F. Mualla, B. Sommerfeldt, S. Steidl, A. Maier, R. Buchholz, and J. Hornegger. "Influence of the phase effect on gradient-based and statistics-based focus measures in bright field microscopy". *Journal of Microscopy*, Vol. 254, No. 2, pp. 65–74, May 2014.

[Scho 14b] S. Schöll, F. Mualla, B. Sommerfeldt, S. Steidl, and A. Maier. "Image Preprocessing Pipeline for Bright-Field Miniature Live Cell Microscopy Prototypes". In: E. K. Polychroniadis, A. Y. Oral, and M. Ozer, Eds., *International Multidisciplinary Microscopy Congress*, pp. 261–267, Springer International Publishing, 2014.

[Silb 05] S. Silbernagl and F. Lang. *Taschenatlas der Pathophysiologie*. Georg Thieme Verlag, Stuttgart, Germany, 2005.

[Sjos 99] P. J. Sjöström, B. R. Frydel, and L. U. Wahlberg. "Artificial neural network-aided image analysis system for cell counting". *Cytometry*, Vol. 36, No. 1, pp. 18–26, 1999.

[Stru] "Structure of a typical animal cell". `https://commons.wikimedia.org/wiki/File%3AAnimal_cell_structure_en.svg`. Accessed: 2016-03-21.

[Sun 04] Y. Sun, S. Duthaler, and B. J. Nelson. "Autofocusing in computer microscopy: selecting the optimal focus algorithm". *Microscopy Research and Technique*, Vol. 65, No. 3, pp. 139–149, October 2004.

[Teag 83] M. R. Teague. "Deterministic phase retrieval: a Green's function solution". *Journal of the Optical Society of America*, Vol. 73, No. 11, pp. 1434–1441, November 1983.

[Volk 02] V. Volkov, Y. Zhu, and M. De Graef. "A new symmetrized solution for phase retrieval using the transport of intensity equation". *Micron*, Vol. 33, No. 5, pp. 411–6, 2002.

[Voll 88] D. Vollath. "The influence of the scene parameters and of noise on the behaviour of automatic focusing algorithms". *Journal of Microscopy*, Vol. 151, No. 2, pp. 133–146, August 1988.

[Weig 13] M. Weigand. *Phase Retrieval from Bright-Field Microscope Images*. Master's thesis, Pattern Recognition Lab, Department of Computer Science, Friedrich-Alexander Universität Erlangen Nürnberg, Germany, February 2013.

[Yang 03] G. Yang and B. J. Nelson. "Wavelet-based autofocusing and unsupervised segmentation of microscopic images". In: *2003 IEEE/RSJ International Conference on Intelligent Robots and Systems (IROS 2003), Las Vegas, Nevada, United States, October 27 – 31*, pp. 2143–2148, 2003.

[Yazd 08] S. Yazdanfar, K. B. Kenny, K. Tasimi, A. D. Corwin, E. L. Dixon, and R. J. Filkins. "Simple and robust image-based autofocusing for digital microscopy". *Optics Express*, Vol. 16, No. 12, pp. 8670–8677, June 2008.

[Yeo 93] T. Yeo, S. Ong, Jayasooriah, and R. Sinniah. "Autofocusing for tissue microscopy". *Image and Vision Computing*, Vol. 11, No. 10, pp. 629–639, December 1993.

[Yu 10] M. Y. Yu, M. L. Han, C. Y. Shee, and W. T. Ang. "Autofocusing algorithm comparison in bright field microscopy for automatic vision aided cell micromanipulation". In: *2010 IEEE 4th International Conference on Nano/Molecular Medicine and Engineering (NANOMED), Hong Kong, China, December 5 – 9*, pp. 88–92, 2010.